INFORMATION TO USERS

This reproduction was made from a copy of a document sent to us for microfilming. While the most advanced technology has been used to photograph and reproduce this document, the quality of the reproduction is heavily dependent upon the quality of the material submitted.

The following explanation of techniques is provided to help clarify markings or notations which may appear on this reproduction.

1. The sign or "target" for pages apparently lacking from the document photographed is "Missing Page(s)". If it was possible to obtain the missing page(s) or section, they are spliced into the film along with adjacent pages. This may have necessitated cutting through an image and duplicating adjacent pages to assure complete continuity.

2. When an image on the film is obliterated with a round black mark, it is an indication of either blurred copy because of movement during exposure, duplicate copy, or copyrighted materials that should not have been filmed. For blurred pages, a good image of the page can be found in the adjacent frame. If copyrighted materials were deleted, a target note will appear listing the pages in the adjacent frame.

3. When a map, drawing or chart, etc., is part of the material being photographed, a definite method of "sectioning" the material has been followed. It is customary to begin filming at the upper left hand corner of a large sheet and to continue from left to right in equal sections with small overlaps. If necessary, sectioning is continued again—beginning below the first row and continuing on until complete.

4. For illustrations that cannot be satisfactorily reproduced by xerographic means, photographic prints can be purchased at additional cost and inserted into your xerographic copy. These prints are available upon request from the Dissertations Customer Services Department.

5. Some pages in any document may have indistinct print. In all cases the best available copy has been filmed.

University Microfilms International
300 N. Zeeb Road
Ann Arbor, MI 48106

Dulman Fand, Hector Daniel

SILICON LIGHT EMITTING PN DIODES AND OPTICAL INTERCONNECT CONSIDERATIONS

The University of Arizona M.S. 1986

SILICON LIGHT EMITTING PN DIODES AND OPTICAL INTERCONNECT CONSIDERATIONS

by

Hector Daniel Dulman Fand

A Thesis Submitted to the Faculty of the

DEPARTMENT OF ELECTRICAL AND COMPUTER ENGINEERING

In Partial Fulfillment of the Requirements
For the Degree of

MASTER OF SCIENCE
WITH A MAJOR IN ELECTRICAL ENGINEERING

In the Graduate College

THE UNIVERSITY OF ARIZONA

1 9 8 6

STATEMENT BY AUTHOR

This thesis has been submitted in partial fulfillment of requirements for an advanced degree at The University of Arizona and is deposited in the University Library to be made available to borrowers under rules of the Library.

Brief quotations from this thesis are allowable without special permission, provided that accurate acknowledgment of source is made. Requests for permission for extended quotation from or reproduction of this manuscript in whole or in part may be granted by the head of the major department or the Dean of the Graduate College when in his or her judgment the proposed use of the material is in the interests of scholarship. In all other instances, however, permission must be obtained from the author.

SIGNED: 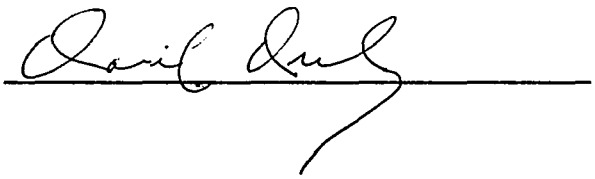

APPROVAL BY THESIS DIRECTOR

This thesis has been approved on the date shown below:

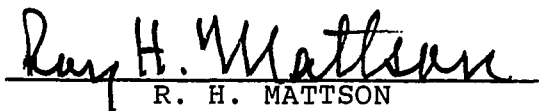

R. H. MATTSON
Professor of Computer and
Electrical Engineering

12-15-86
Date

TABLE OF CONTENTS

TABLE OF CONTENTS--Continued

LIST OF ILLUSTRATIONS

LIST OF ILLUSTRATIONS--Continued

LIST OF ILLUSTRATIONS--Continued

LIST OF ILLUSTRATIONS--Continued

LIST OF TABLES

ABSTRACT

Metal interconnections in silicon IC circuits cause problems and limitations associated with electromigration, pin out counts, frequency response, crosstalk, and reflections. Electro-optical technologies show promise for overcoming many of these problems and limitations, thereby providing optical interconnections. This thesis presents a study of silicon light emitting PN diodes for such interconnects. Obtained data include an efficiency of 6×10^{-7}, a quantum efficiency of about 3×10^{-6}, and a wide band spectrum, which decrease monotonically between 2 eV and 3 eV in the measured photon energy region. These results compare well with published results and provide guidance for future optical interconnection research. In addition, an optical interconnect technology is proposed and a ZnS wet etch procedure is tested.

CHAPTER 1

INTRODUCTION

New technologies are needed for very large scale integrated circuits (VLSI) to transmit information both on-chip and from chip to chip. There are problems with metal interconnections associated with interconnects, crosstalk, electromigration, crossovers, size, and frequency limitations.

For example, the clock distribution metallization system on a VLSI chip has time delays which can cause information to reach different points on the chip at different times. Also, the number of interconnections on the chip and between the chip and the board increases with the complexity of the device; this requires more and more metallization. As the number of pins increases, it becomes a technological problem to connect them to the board. Thus, it is evident that a communication crisis in VLSI circuits exists, and that a solution is necessary.

This thesis investigated the possibility of supplementing metal interconnections with optical ones. Benefits expected include reduced loading effects, the possibility of single-level planar waveguide crosses which do not

significantly interfere, and immunity to mutual interference (Goodman et al., 1984).

Optical interconnects, however, require the coupling of the light from an electronic device to the waveguide and vice versa. This thesis focuses on the on-chip optical interconnections and a light source for these on-chip optical interconnections. A silicon light emitting device has been fabricated in the Microelectronics Laboratory (MEL) at the University of Arizona (UA).

Chapter 2 of this thesis describes the theoretical considerations underlying the light source, detectors, and optical waveguides. Chapter 3 focuses on the fabrication of light sources. The fabrication procedure is given, and data are presented concerning the power output, efficiency, and spectrum. In Chapter 4, an optical interconnect technology is proposed and exploratory experimental results are presented. Chapter 5 summarizes the work and presents guidelines and recommendations for further research.

CHAPTER 2

THEORY

2.1 Introduction

This chapter describes the basic theory of the light sources, detectors and optical waveguides. The section on light emitting devices begins with a review of the underlying solid state physics concepts, followed by p-n junction characteristics. Then the theory of reverse voltage breakdown of a p-n diode and, finally, possible light emission processes are described. Several theories concerning the generation of light by a silicon diode are presented since there is still considerable controversy about the mechanism giving rise to this phenomenon.

The photodetector section introduces relations that predict detection phenomena. Different types of detectors are discussed.

The waveguide section begins with a basic geometric optics analysis of such guides. Some physical optics improvements and coupling problems are discussed. Useful waveguide materials are presented, along with their characteristics.

2.2 Silicon Light Emitting Device

2.2.1 Solid State Physics Concepts

This section reviews some basic concepts of solid state physics, for a better understanding of the different light emission theories. A more in-depth study may be found in the book by Kittel, Introduction to Solid State Physics, Fifth Edition, 1976.

When electrons are in close proximity to one another in a crystalline solid, the presence of nearby atoms affects their behavior and their energies are not uniquely determined. The single energy level of a free electron is spread into a band, or range, of energy levels. According to the band theory of solids, and considering the quantum mechanical wavefunctions and wavevectors associated with the electrons, discontinuities occur in energy levels at certain values of the electronic wavevectors.

The discontinuities are called energy gaps, or band gaps. These gaps represent energy levels which are not allowed for the electrons. Semiconductor materials, e.g., silicon, have at $0^{\circ}K$ a filled "valence" band with a relatively small band gap separating it from an empty "conduction" band. At any finite temperature a small number of electrons is found at the bottom of the conduction band, and a number of unfilled states, or "holes" is found in the

valence band (Fig. 2.1). Electrical conduction is possible by the motion of both, electrons and holes.

Energy band structures are usually plotted as a function of the propagation constant or wavevector $\vec{k}$ associated with the electron. Figure 2.2 shows the energy band structure for silicon, for two directions of $\vec{k}$: [100] and [111]. The "top valence band" consists of two closely spaced bands: "heavy hole valence band" and "light hole valence band." These two bands degenerate at k = 0, as shown in Fig. 2.3. (See also page 226 of Kittel (1976), and page 13 of Sze (1981).) The "split off valence band" is shifted down in energy from the preceding ones in 0.035 eV at k = 0 due to the spin orbit coupling. Because the minimum of the conduction band and the maximum of the valence band occur at different k-values, silicon is called an "indirect" band gap semiconductor.

An electron must make a transition in energy for light to be emitted. When a transition occurs, energy and momentum must be conserved. Direct transitions do not change the k value of the electron. The energy difference is given up as a quantum of electromagnetic energy, i.e., a photon (light), whose component of momentum is negligible. Indirect transitions must be assisted by phonons in order to conserve momentum. A phonon is defined in the next

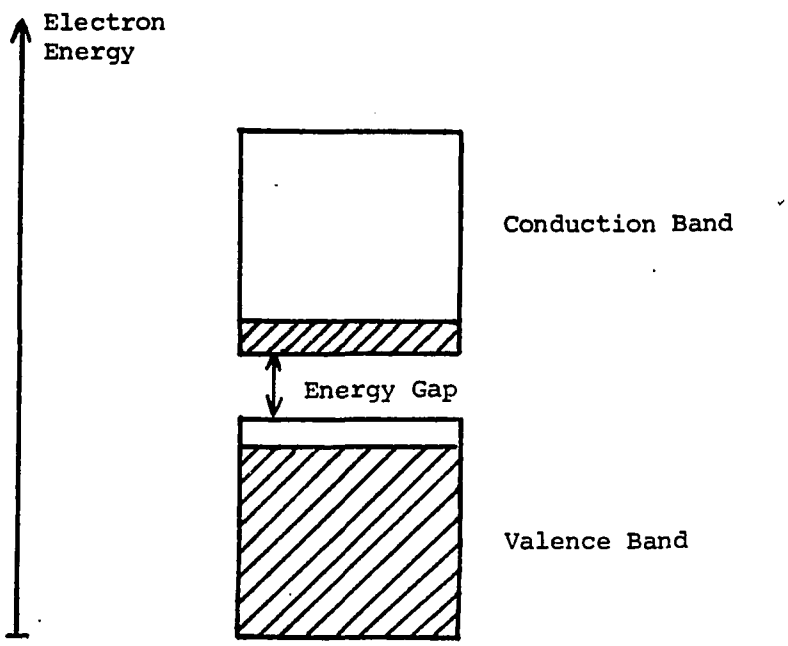

Fig. 2.1. Energy-band diagram for a semiconductor (after Fink and Christiansen, 1982). -- The energy gap is of the order of 1 eV.

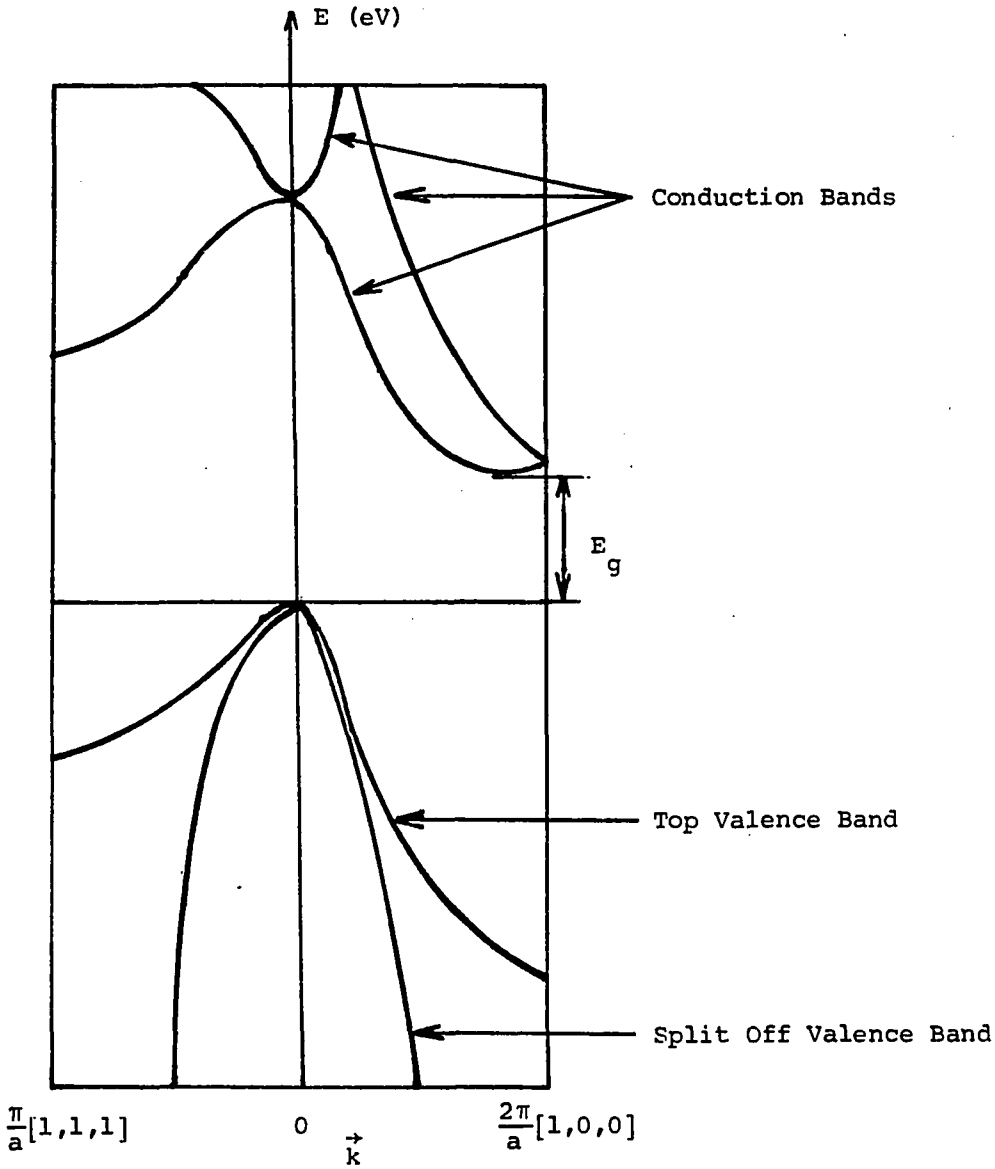

Fig. 2.2. Energy-band structure for silicon in k-space (after Sze, 1981). -- The "top valence band" consists of two bands closely spaced which degenerate at k = 0. See Fig. 2.3.

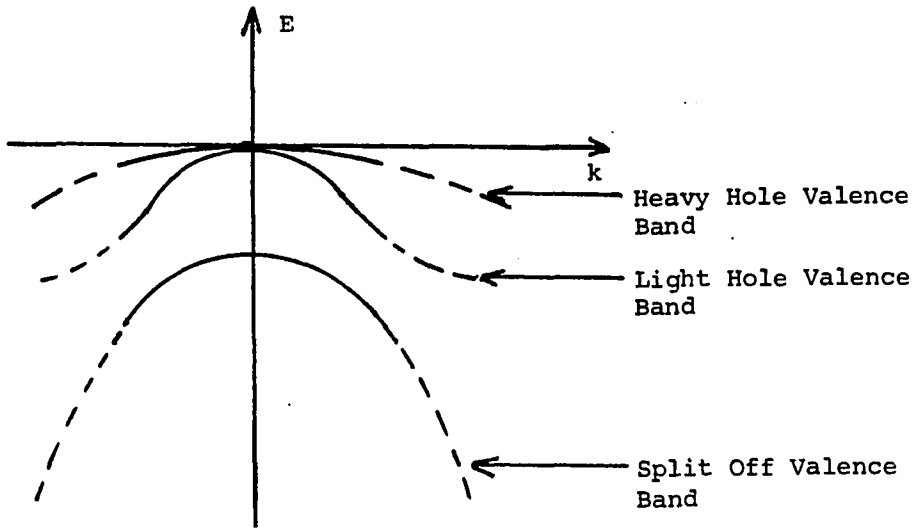

Fig. 2.3. Valence band edge structure, shown in k-space. -- Dashed lines show the valence band structure for larger k-values, based on Kittel (1976), page 226. This plot is for germanium, which has a diamond structure like silicon.

paragraph. The energy is more usually given up as heat to the lattice rather than as an emitted photon.

The energy of a lattice vibration is quantized. The quantum of vibrational energy is called a "phonon" or, more accurately, an "acoustic phonon." Vibrations between the atoms associated with each lattice point, i.e., within the primitive cell, are also quantized, and their quantum of energy is called an "optical phonon."

Electrons in a crystal lattice behave as if their masses were different from the mass m_o of a free electron. Thus, in order to satisfy Newton's second law, it is necessary to define an "effective" mass, m*, of an electron in the crystal lattice. This value is related to the curvature of the energy bands, i.e., with the second derivative of the electron energy E with respect to k in the band under consideration. Usual values range from 0.1 m_o to m_o.

2.2.2 The P-N Junction

Planar step junctions are considered in this section; also, remarks on deviations from the theory are presented.

In p-n junction semiconductor devices a depleted space charge region exists in the immediate vicinity of the junction. Electrons migrate from the n-region to the p-region, leaving behind positively charged ionized donor atoms. Some of these electrons are trapped by the acceptor

atoms and ionize them negatively. These processes form the "space charge region," also called the "depletion" or "transition" regions. The resulting electric field from those uncompensated impurities creates a potential barrier for the mobile majority carriers. In equilibrium a drift component of current opposes the diffusion component, and the total current is zero. Thus, for example, for the hole current $J_p(x)$,

$$J_p(x) = q.[\mu_p.p(x).\varepsilon(x) - D_p \cdot \frac{dp(x)}{dx}] = 0 \qquad (2.1)$$

Drift Diffusion

where

μ_p = mobility of holes

$p(x)$ = hole concentration

$\varepsilon(x)$ = intensity of the electric field

D_p = diffusion coefficient of holes

x = measured normal distance to the junction

This is shown in Fig. 2.4. Solving the electrostatic problem presented in Fig. 2.4 leads to the contact potential V_o as:

$$V_o = \frac{kT}{q} \cdot \ln \frac{N_a.N_d}{n_i^2} \qquad (2.2a)$$

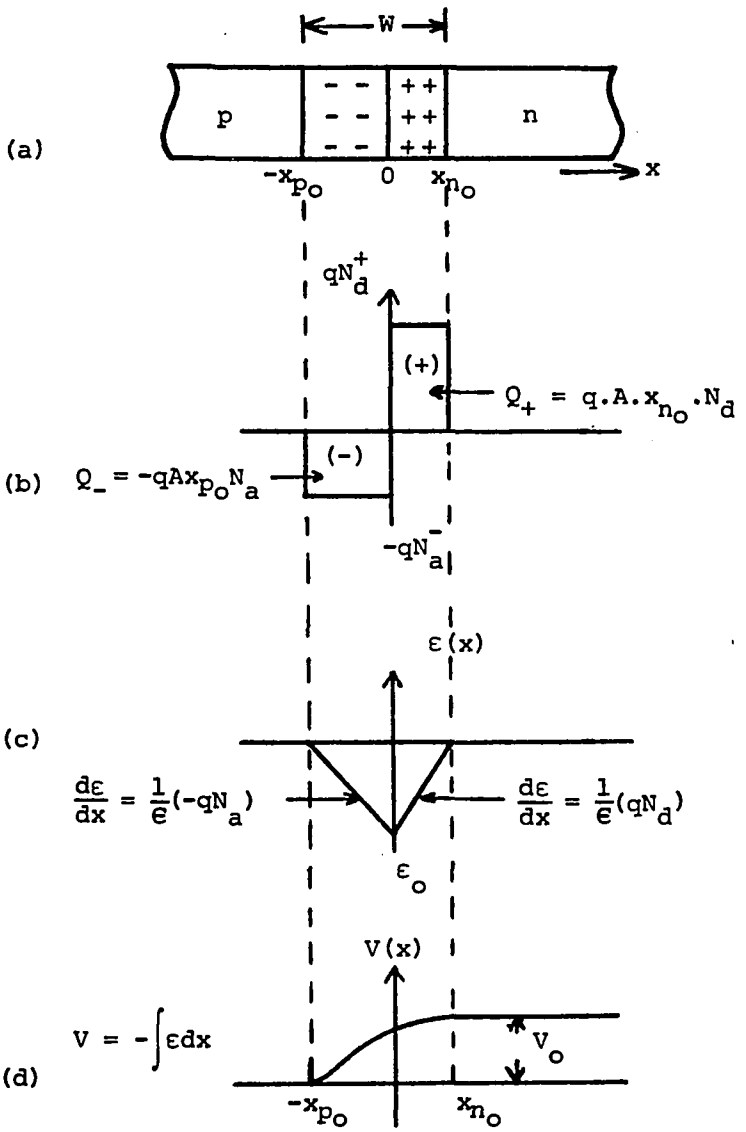

Fig. 2.4. Properties of the step junction transition region (after Streetman, 1980). -- (a) Transition region; (b) Charge density; (c) Electric field; and (d) Electrostatic potential.

where

N_a and N_d = ionized impurity concentrations in the p and n regions, respectively

n_i = intrinsic carrier concentration, 1.5×10^{10} cm^{-3} for silicon at 300^oK

For example, for $N_a = 10^{15}$ cm^{-3} and $N_d = 10^{19}$ cm^{-3}, $V_o = 0.8$ V. The width of the depletion region, W_o, can also be determined. Using Gauss' law and integrating twice in the depletion region (Fig. 2.4), the result is:

$$W_o = \left[\frac{2\epsilon V_o}{q}\left(\frac{1}{N_a} + \frac{1}{N_d}\right)\right]^{1/2} \qquad (2.2b)$$

$$x_{p_o} = \frac{W_o \cdot N_d}{N_a + N_d}$$

$$x_{n_o} = \frac{W_o \cdot N_a}{N_a + N_d}$$

where ϵ is the dielectric permittivity of silicon ($11.8\ \epsilon_o$). An important result is the maximum electric field at the junction $\varepsilon_{o_{max}}$

$$\varepsilon_{o_{max}} = -\frac{2V_o}{W_o} \qquad (2.2c)$$

The abrupt junction approximation is not always adequate for analyzing diffused junction devices, and it is necessary to apply the linearly graded junction approximation. Figure 2.5 shows the space charge, electric field,

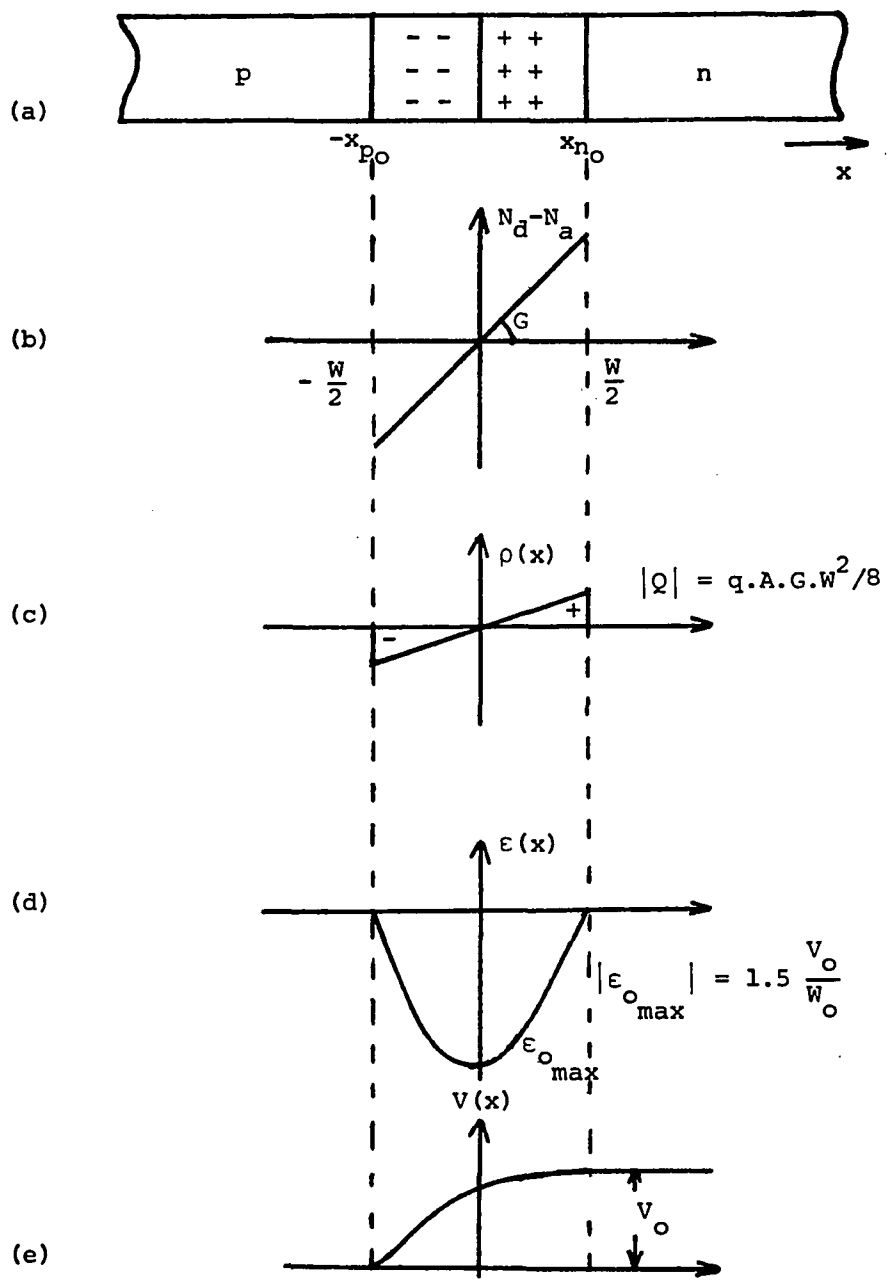

Fig. 2.5. Properties of the graded junction transition region (after Streetman, 1980). -- (a) Transition region; (b) Net impurity profile; (c) Net charge distribution; (d) Electric field; and (e) Electrostatic potential.

and electrostatic potential within the depletion region, assuming a linearly graded junction. Applying a similar mathematical treatment, the following relations result (Grove, 1967):

$$V_o = \frac{2kT}{q} \cdot \ln \frac{G.W_o}{2n_i} \tag{2.3a}$$

$$W_o = \left[\frac{12\epsilon V_o}{qG}\right]^{1/3} \tag{2.3b}$$

$$\varepsilon_{o_{max}} = -1.5 \frac{V_o}{W_o} \tag{2.3c}$$

where W_o is the width of the zero-bias (equilibrium) depletion region, and G is the impurity concentration gradient at the junction:

$$G \equiv \left.\frac{d(N_d - N_a)}{dx}\right|_{x=x_j} \tag{2.4}$$

2.2.2.1 Forward Bias. Forward biasing the junction causes the p side to be positive with respect to the n side, which reduces the energy barrier. Under the presence of a bias voltage V, the excess (injected) minority carrier concentration is:

$$\Delta P_n = P(x_{n_o}) - P_n = P_n(e^{qV/kT} - 1) \tag{2.5}$$

Therefore under forward bias the injection of minority carriers across the junction increases exponentially with

the applied voltage. On the other hand, once across the junction, those carriers will recombine with the majority carriers, giving an excess minority carrier concentration that decreases with x (see Fig. 2.6a):

$$\delta p(x) = \Delta p.e^{-x_n/L_p} \tag{2.6}$$

where δp is the excess concentration, and L_p is the diffusion length of holes. x_n is measured from x_{n_o}, as shown in Fig. 2.6. The injected current in the n material due to holes is calculated at x_{n_o}:

$$I_p(0) = -q.A.D_p \cdot \left.\frac{d\delta p(x_n)}{dx_n}\right|_{x_n=0} = \frac{q.A.D_p}{L_p} \cdot p_n.(e^{qV/kT} - 1) \tag{2.7}$$

Similar reasoning may be applied for excess electrons injected in the p region. Assuming there is no recombination in the depletion region, the total current I is obtained by adding both $I_p(0)$ and $I_n(0)$, and the result is:

$$I = q.A.\left(\frac{D_p}{L_p} \cdot p_n + \frac{D_n}{L_n} \cdot n_p\right) \cdot (e^{qV/kT} - 1)$$

$$\equiv I_o \cdot (e^{qV/kT} - 1) \tag{2.8}$$

Hence, the current increases exponentially under forward bias.

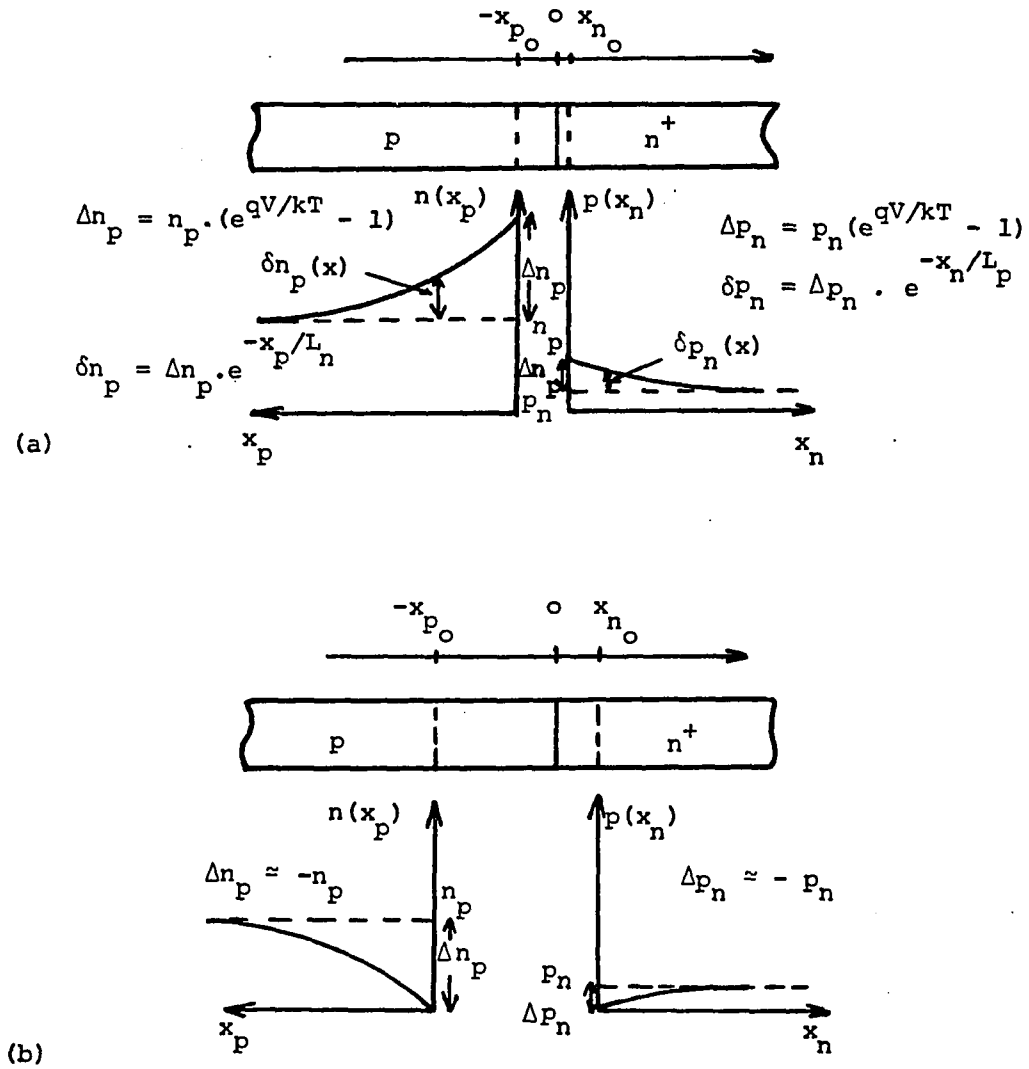

Fig. 2.6. Injection characteristics of a p-n^+ junction (after Streetman, 1980). -- (a) Forward bias; and (b) Reverse bias.

The width of the depletion region and maximum electric field under forward bias are obtained by replacing V_o by $V_o - V$ in Eqs. 2.2b and 2.2c for the step junction, and in Eqs. 2.3b and 2.3c for the linearly graded approximation.

2.2.2.2 Reverse Bias. Under reverse bias these equations are equally valid considering V negative, but different aspects become important. As shown in Fig. 2.6b, there is a reduction of minority carriers close to the depletion region. Physically, all the minority carriers at the edges of the depletion region are swept to the other side through the depletion region of the junction. The minority concentrations at the edges of the depletion region are therefore zero, and a gradient of their concentration toward the depletion region exists. For V negative larger than a few times kT/q (0.026 V), the current through the device is simply $-I_o$, constant. The width of the depletion region increases with V, extending mostly into the low doping concentration side of the junction. Additionally, $|\varepsilon_{max}|$ is proportional to $(V_o - V)/W$, but W is proportional to $(V_o - V)^{1/2}$. Thus, $|\varepsilon_{max}|$ is proportional to $(V_o - V)^{1/2}$; that is, the peak electric field increases with the reverse bias. A similar conclusion is obtained using the linearly graded approximation.

Figure 2.7 shows the I-V characteristics of a p-n junction and related energy band diagrams under forward and reverse bias.

2.2.2.3 Reverse Bias Breakdown. When a p-n junction is reverse biased, the current through it is normally very small and voltage independent. For large reverse bias, a critical or breakdown voltage is reached after which the current increases sharply (see Fig. 2.7). Small further increases in the voltage cause large currents to flow. This breakdown voltage (BV) is caused by either one of two mechanisms: Zener effect or avalanche breakdown (Streetman, 1980; Grove, 1967).

An abrupt junction with both sides heavily doped has a very narrow depletion region. When reverse biased, the energy bands bend in such a way at relatively low voltages that Zener breakdown occurs. Carriers are separated from empty states by the narrow barrier. Under these conditions, tunneling of carriers can happen. This leads to large currents due to the Zener effect. Experimentally, it is found that Zener breakdown begins at fields of the order of 10^6 V/cm.

For graded or lightly doped junctions, electron tunneling is negligible; breakdown takes place as a result of impact ionization between host atoms and energetic carriers. When the internal electric field becomes large

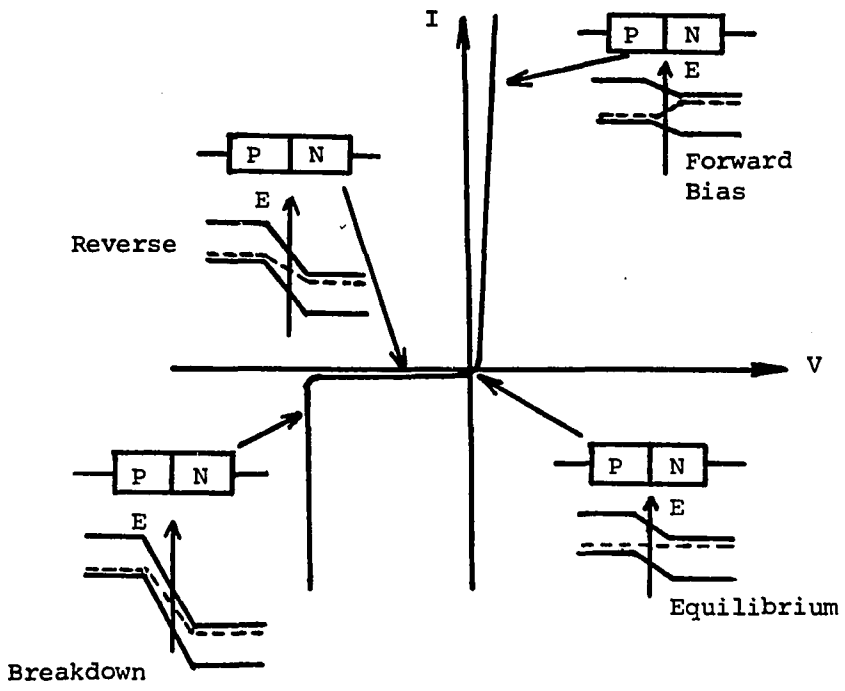

Fig. 2.7. p-n junction I-V characteristics and related energy band diagrams (after Fink and Christiansen, 1982).

enough (2×10^5 V/cm), a carrier entering the depletion region may gain enough kinetic energy to cause an ionizing collision with the lattice. Figure 2.8 shows the energy band diagram for a p-n diode under reverse bias, and the different steps that lead to carrier multiplication. In Step 1 an electron-hole pair (EHP) is generated thermally in the depletion region. If the electric field is high enough, the electron, and similarly the hole, will gain sufficient kinetic energy (Steps 2 and 2') that when it collides with the lattice it will break a silicon bond in the collision, generating a new EHP and giving up kinetic energy (Steps 3 and 3'). The original carrier and the new ones are now accelerated; each one will produce additional EHPs until they reach the edge of the depletion region.

If the electric field is not sufficiently high, the multiplication of carriers is smaller than at breakdown. If I_o is the reverse saturation current through a reverse biased junction and I_R is the reverse current when multiplication occurs, it has been found empirically that:

$$M = \frac{I_R}{I_o} = \frac{1}{1 - (\frac{V}{BV})^n} \qquad (2.9)$$

where

M = multiplication factor

n = an empirical number between 3 and 6

V = reverse voltage

BV = the "breakdown voltage"

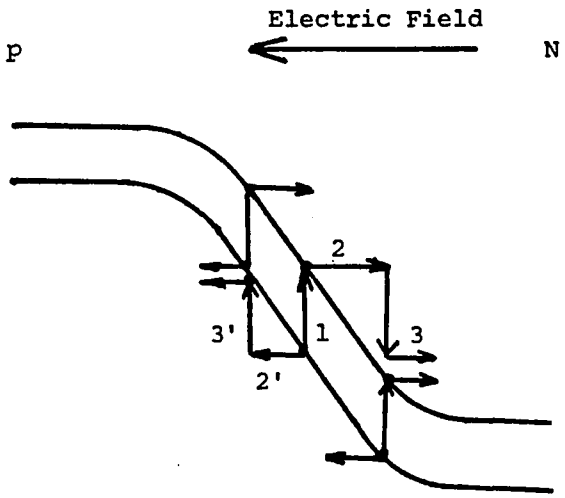

Fig. 2.8. Scheme of the avalanche breakdown process (after Grove, 1967).

Note that for V approaching the BV value, multiplication tends to increase indefinitely although the external resistance in the circuit limit the current. This situation is called "avalanche breakdown." Assuming a step junction, the BV is found making the maximum field in the junction, ε_{max} equal to the critical field for the avalanche process, ε_c. For the case of a p-n^+ junction the following result is obtained:

$$BV = \frac{\epsilon}{2qN_a} \cdot \varepsilon_c \qquad \text{for step junctions} \qquad (2.10)$$

$$BV = \left(\frac{32\epsilon\varepsilon_c^2}{9qG}\right)^{1/2} \qquad \text{for linearly graded junctions} \qquad (2.11)$$

In order to avoid undesirable series resistance in the p side of a p-n^+ junction, the usual structure is p^+-p-n^+. For very low p concentrations, where the p region may approach intrinsic doping levels, this structure is also referred to as the PIN diode. In this case the depletion region extends over most of the lightly doped p region. If the p region is not large enough, it may become fully depleted; then the depletion region width increases very slowly in the p^+ and n^+ regions; thus, the electric field reaches the critical value for lower V, causing a BV much lower than expected. This situation is called punch-through.

2.2.3 Light Emission Process in Silicon

Visible light emitted by reverse biased p-n junctions in the breakdown region has been attracting the attention of scientists since 1955, following its discovery by Newman (1955). The emission came from the regions where avalanche breakdown was taking place (Chynoweth and McKay, 1956). The spectrum was measured and theories were developed to fit the spectrum and explain the phenomenon. Most publications agree as to the emission spectrum for silicon. The spectrum is wideband with no definite structure, extends from less than 1 eV to more than 3 eV, and falls monotonically more than four orders of magnitude with increasing emitted photon energy (Fig. 2.9). Unless otherwise stated, all the spectra described in this section represent the number of emitted photons per unit photon energy interval per unit time; that is, $J_{out}(\hbar\omega)/\hbar\omega$, where J_{out} is the power emitted per photon energy interval, and $\hbar\omega$ is the photon energy. The spectral dependence of the light emitting device in terms of the quantum efficiency represents the number of photons emitted per unit energy interval per unit time and per electron. Thus, for constant current input, the quantum efficiency is proportional to $J_{out}/\hbar\omega$.

Different types of transitions between energy bands may give up a photon. Figure 2.10 shows a simplified energy band structure for an indirect band gap semiconductor. Only

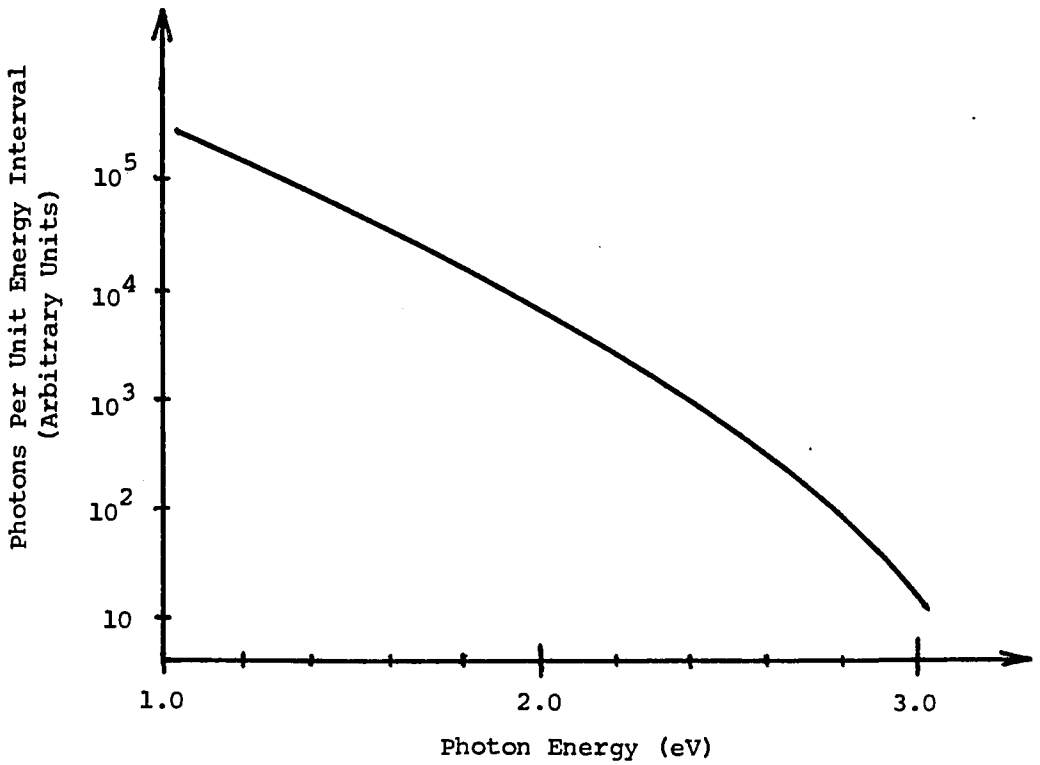

Fig. 2.9. Emission spectrum for silicon (after Chynoweth and McKay, 1956).

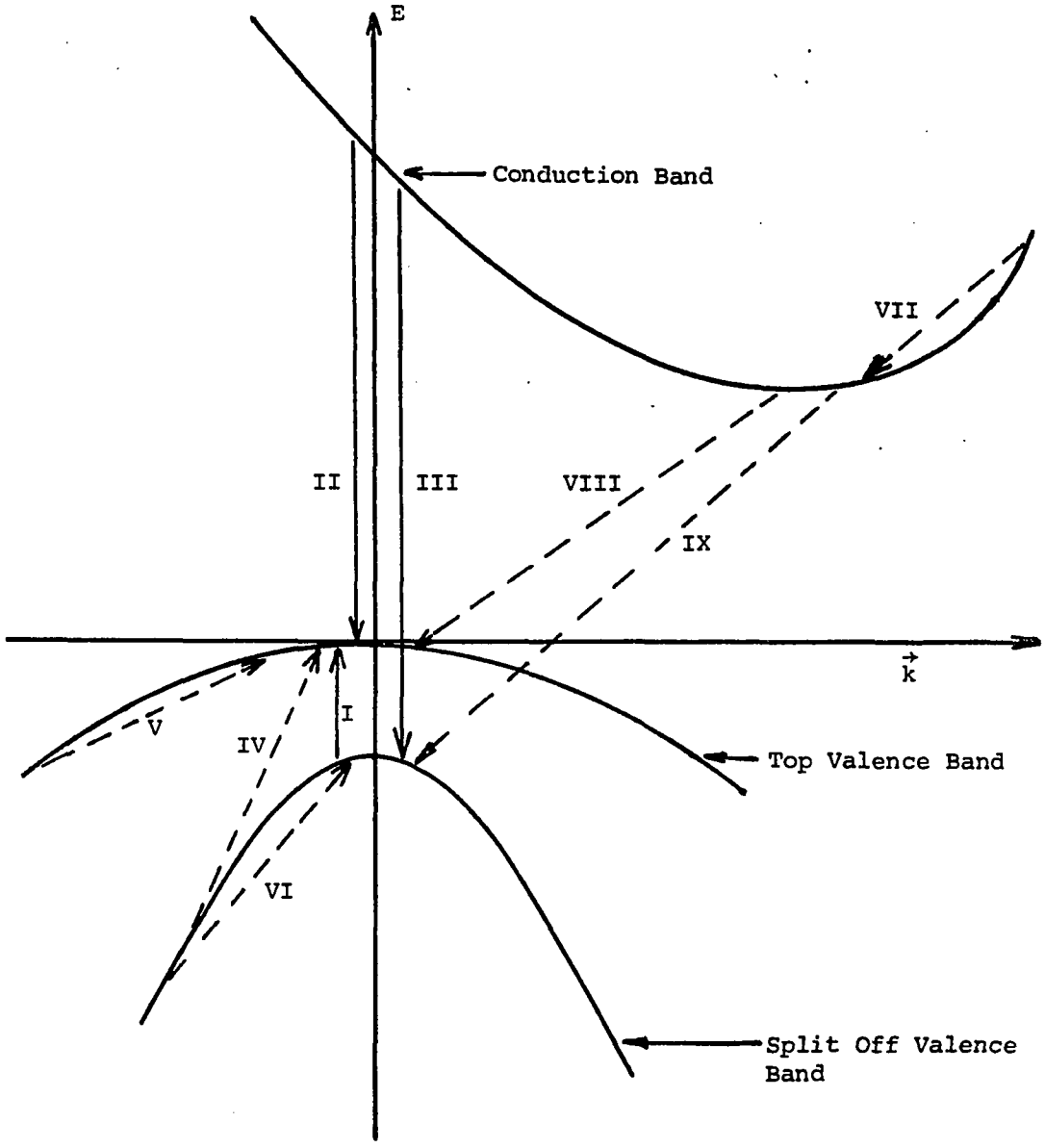

Fig. 2.10. Simplified energy band structure for silicon, and different types of transitions. -- Solid lines represent direct transitions. Dashed lines represent indirect transitions.

the least energetic conduction band, the top valence band and the split-off valence band are considered (Fig. 2.2). Figure 2.10 also shows different types of transitions between energy bands. The following is a description of each type of transition:

I. Direct intraband transition between valence bands.

II. Direct interband transition between conduction and top valence bands.

III. Direct interband transition between conduction and split-off valence bands.

IV. Indirect intraband transition between valence bands.

V. Indirect intraband transition within the top valence band.

VI. Indirect intraband transition within the split-off valence band.

VII. Indirect intraband transition within the conduction band.

VIII. Indirect interband transition between conduction and top valence bands.

IX. Indirect interband transition between conduction and split-off valence bands.

In principle, transitions do not necessarily take place at $k = 0$ or at the minimum of the conduction band. The schematic characteristics are seen in Fig. 2.10. Considering the full energy band structure for silicon shown in

Fig. 2.2, it is clear that Transitions I, IV, V, VI and VII may also give up photons with energies much larger than the energy band gap, particularly in the visible region of the spectrum.

As said before, transitions must conserve momentum, and direct transitions respect this rule. For indirect transitions, two possible processes are considered for momentum conservation: scattering by acoustic or optical phonons, and scattering by charged impurity centers. The latter is based on an old model, proposed by Figielski and Torun in 1962, which states that emission takes place when hot carriers are decelerated in the coulombic field of charged impurity centers (Haecker, 1974).

Three theories are considered in the following paragraphs. Haecker (1974) finds that the dominant process is direct intraband transitions of free holes (Transition I, Fig. 2.10); he cannot fit his spectrum assuming indirect transitions of any type (IV to IX). Kosyachenko, Kukhto, and Sklyarchuk (1984) conclude that the dominant process is indirect intraband transitions of high energy carriers accompanied by the transfer of momentum to acoustic phonons (IV to VII). Additionally, indirect interband transitions (VIII and IX) may be present. These Russian authors cannot fit their spectrum assuming scattering with impurity centers. Tam and Hu (1984) conclude that the dominant

process is intraband transitions of hot electrons (VII), accompanied by the transfer of momentum to impurity centers. These authors demonstrate that intraband transitions of holes (I, IV, V, and VI) are not the dominant processes and suggest that interband transitions (II, III, VIII, and IX) are also not the dominant processes.

Haecker studied the light emission phenomenon in 1974 using a 0.25 m Jarrell-Ash monochromator with two gratings blazed at 2.1 and 1.2 microns, and a Santa Barbara Research Center PbS detector. Haecker measured the power spectrum J_{out} in the photon energy range $0.5\ E_g \leq \hbar\omega \leq E_g$ where no self-absorption takes place. This spectrum appears in Fig. 2.11. Haecker could explain his observed spectrum by considering direct intraband transitions of holes between different valence bands, type I as described in Fig. 2.10. The emitted power per unit energy interval must be proportional to the probability $f(E_1)$ (defined in Eq. 2.16) of having a hole with energy E_1 in the split-off valence band, to the probability $1-f(E_2)$ of having an electron with energy E_2 in the top valence band, times the density D_k of available states in each band, multiplied by the rate A of spontaneous emission:

$$J_{out}(\hbar\omega) \alpha f(E_1).[1 - f(E_2)].D_k.A \qquad (2.12)$$

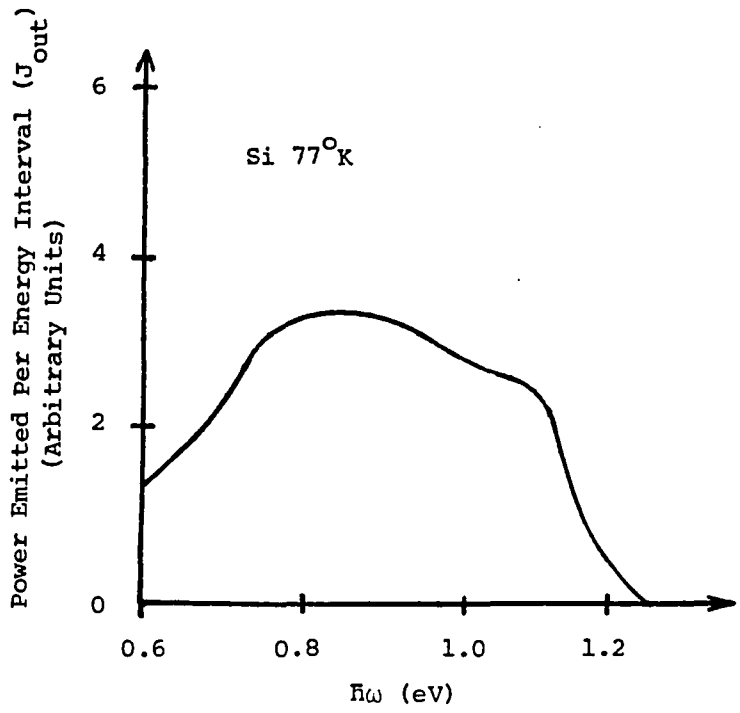

Fig. 2.11. Spectrum measured by Haecker (1974). -- It is noted that this spectrum corresponds to power and not number of photons emitted per unit energy interval.

According to Haecker, the density of states D_k is proportional to $(\hbar\omega - \Delta E)^{1/2}$, where $\hbar\omega$ is the photon energy, and ΔE is the spin orbit splitting. The rate A of spontaneous emission is calculated from the coefficient B of the stimulated emission, and gives a result proportional to $(\hbar\omega)^2 k^2$. Assuming parabolic bands, the photon energy is:

$$\hbar\omega = E_1 - E_2 = \frac{\hbar^2}{2m_1^*} \cdot k^2 + \Delta E - \frac{\hbar^2}{2m_2^*} \cdot k^2 \qquad (2.13)$$

where m_1^* and m_2^* are the effective hole masses in the split-off and top valence bands, respectively. Thus, k^2 is proportional to $\hbar\omega - \Delta E$. In addition, the probability $1 - f(E_2)$ of having an electron in a valence band is close to unity. By substitution, the power output per unit energy interval turns out to be proportional to a power function in $\hbar\omega$ times the distribution of holes in the split-off valence band for an energy E_1, also a function of $\hbar\omega$:

$$J_{out}(\hbar\omega) \alpha (\hbar\omega)^2 . (\hbar\omega - \Delta E)^{3/2} . f(E_1) \qquad (2.14)$$

with:

$$E_1 = \frac{\hbar\omega - \Delta E}{1 - \frac{m_1^*}{m_2^*}} + \Delta E \qquad (2.15)$$

Haecker assumes that the probability f(E) of having a hole with energy E is given by the distribution function found by Baraff in 1964. Here only the result is presented:

$$f(E) = c_1 . \left(\frac{E}{E_i}\right)^{-a} . \exp[-b(E - E_i)] \qquad (2.16)$$

where E_i is the ionization energy, and c_1, a, and b are parameters that depend on E_i, the maximum electric field in the junction, the optical phonon energy, and the mean free path between energy losing collisions. Figure 2.12 shows the spectrum, J_{out}, comparing the measurements of Haecker and Chynoweth-McKay, with the theoretical spectra based on Haecker's approach.

Haecker also calculated the theoretical spectrum assuming indirect transitions as the dominant process. Using an equation of the stimulated emission rate times the density of states developed by Fan et al. (1956) and doing a similar reasoning as for direct transitions, the following result was obtained:

$$J_{out}(\hbar\omega) \alpha (\hbar\omega)^{3-r} \int_{\hbar\omega}^{+\infty} f(E) . \left(1 + \frac{2E}{\hbar\omega}\right) . \left(1 + \frac{E}{\hbar\omega}\right)^{1/2} dE \qquad (2.17)$$

where

r = 1.5 for acoustical phonon scattering

r = 2.5 for optical phonon scattering

r = 3.5 for scattering with impurity centers

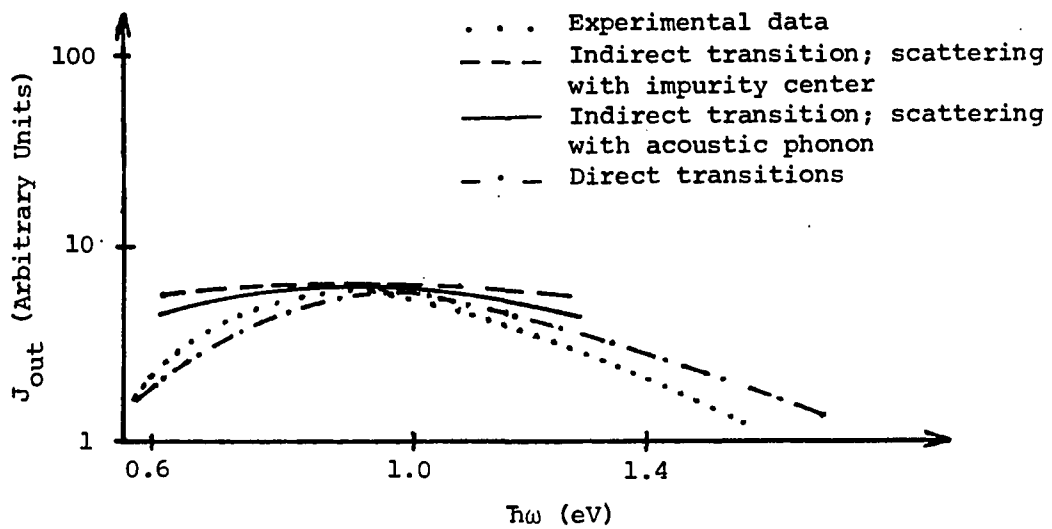

Fig. 2.12. Comparison of experimental data by Haecker and Chynoweth-McKay with different theoretical spectra (after Haecker, 1974).

This integral was calculated numerically. As Fig. 2.12 shows, no fit was possible. Thus a full explanation that satisfies the experiment is not available.

Kosyachenko et al. (1984) used a DMR-4 monochromator and a PbS photodetector or an FEU-38 photomultiplier and found the two emission spectra which are shown in Fig. 2.13. These Russian scientists did not give any fabrication or structural differences between the silicon diodes that gave rise to these two types of spectra. The basic difference between the quantum efficiencies of the two spectra is the presence of a peak at a photon energy close to the energy band gap, E_g, in Fig. 2.13b. This peak was attributed to indirect interband radiative transitions of thermalized carriers, i.e., Transitions VIII and IX in Fig. 2.10. The authors developed a model to explain the wideband nature of both spectra, but especially the one shown in Fig. 2.13a which is of the same shape as the one found by Chynoweth and McKay (1956) (Fig. 2.9), based on indirect intraband transitions of high energy carriers.

Four transitions may be present: IV, V, VI, and VII (Fig. 2.10). In order to conserve momentum, two processes are considered: scattering by acoustic phonons and scattering by impurity centers. Based on other Russian studies (Kosyachenko, Kukhto and Sklyarchuk, 1982; Guts, Kosyachenko and Solonchuk, 1983), Kosyachenko et al. (1984)

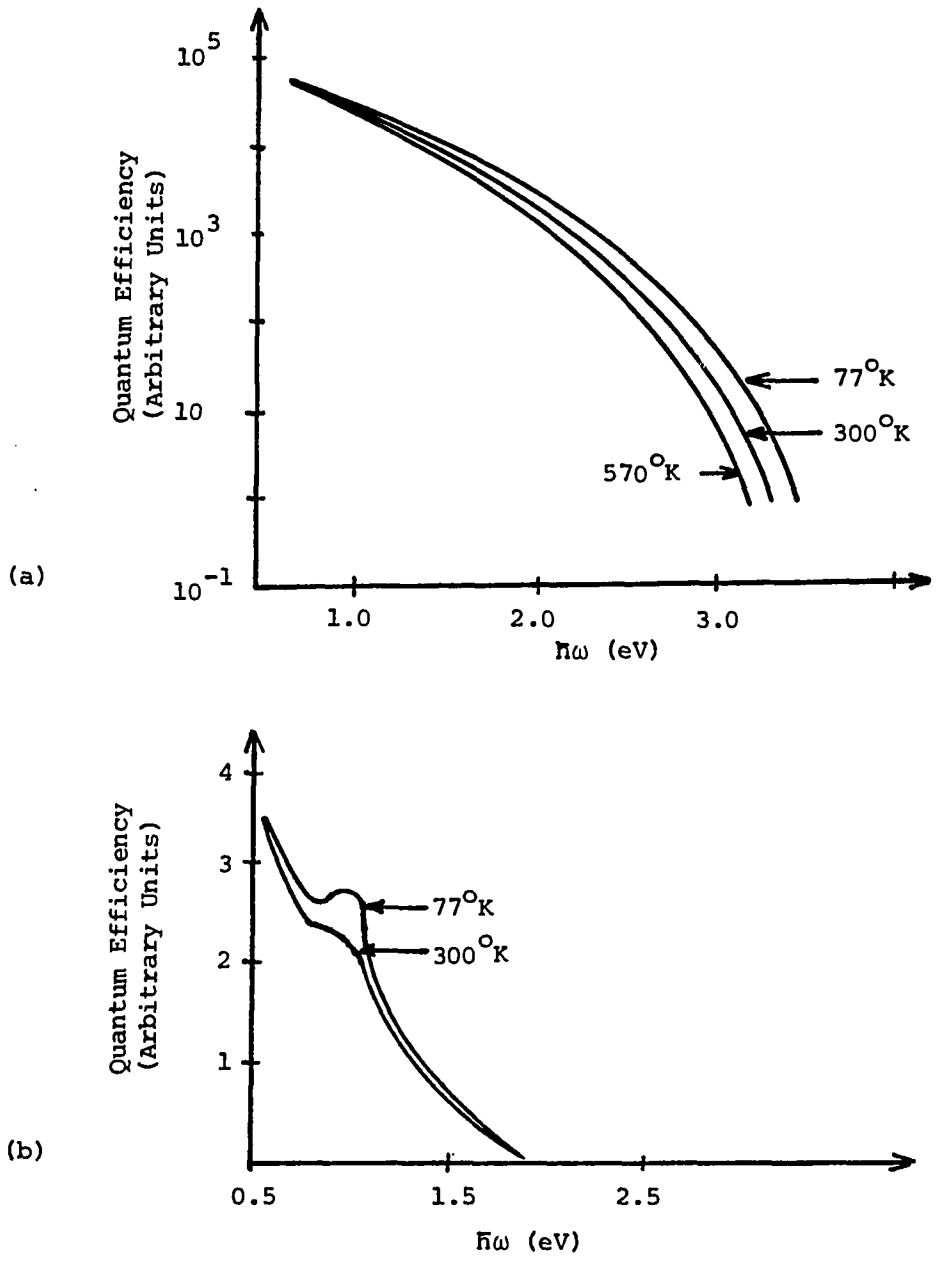

Fig. 2.13. Measured spectra by Kosyachenko, Kukhto and Skylarchuk (1984). -- (a) Wide band type; and (b) Peak type. The peak in (b) is at 1.1 eV, that is, E_g. No characteristics are given about the diodes that produced each spectra.

express the spectral dependence of the quantum efficiency $\eta(\hbar\omega)$ for the intraband luminescence as follows:

$$\frac{J_{out}}{\hbar\omega} \alpha \eta(\hbar\omega) = \eta_o^1 . \sigma . (\hbar\omega)^{1/2} . (E_{max}^2 - \hbar\omega . E_{max})^{3/2} \tag{2.18}$$

where η_o^1 depends on the refraction index, effective masses, and energy losses due to the interaction with phonons. E_{max} is the maximum energy of a carrier in a band. σ is the cross-section for the absorption of a photon by a free carrier, and has the form $\sigma_o/(\hbar\omega)^r$, where r is taken as 1.5 for scattering by acoustic phonons and 3.5 for scattering by charged impurities; σ_o is a constant independent of $\hbar\omega$. Substituting in Eq. 2.18, the following equation is obtained:

$$\frac{J_{out}}{\hbar\omega} \alpha \eta(\hbar\omega) = \eta_o \frac{(E_{max}^2 - \hbar\omega . E_{max})^{3/2}}{(\hbar\omega)^{r-1/2}} \tag{2.19}$$

where η_o is the proportionality constant. From this result, it can be proven that scattering takes place with acoustic phonons and not with impurity centers. Equation 2.19 can be rewritten in a more convenient form:

$$[\eta(\hbar\omega) . (\hbar\omega)^{r - 1/2}]^{2/3} = \eta_o^{2/3} . (E_{max}^2 - \hbar\omega . E_{max}) \tag{2.20}$$

The second member of Eq. 2.20 represents a straight line in $\hbar\omega$ with negative slope. The quantum efficiency per unit energy interval $\eta(\hbar\omega)$ is given in Fig. 2.13a. If these values of $\eta(\hbar\omega)$ are substituted in the first member of Eq. 2.20, using r = 1.5 and adequate constants, a negative slope can be obtained and the straight line can be fitted (see Fig. 2.14). The decrease for $\hbar\omega > E_g$ is attributed to self-absorption. For r = 3.5, a positive slope is obtained and no fit is possible.

An additional justification was given: if scattering with impurity centers were the dominant mechanism, it would be reasonable to expect an increase in luminescence and quantum efficiency with higher doping. However, this was not observed by Kosyachenko et al. (1984).

In summary, then, according to Kosyachenko et al. (1984), the electroluminescence is explained by indirect intraband transitions of high-energy carriers accompanied by the transfer of momentum to acoustic phonons. They demonstrated that scattering with impurity centers does not explain the phenomenon.

In recent years the presence of minority carriers has been observed in the substrate of MOSFET devices biased deep into saturation (Fig. 2.15). Many authors (Tam et al., 1983; Tam and Hu, 1984) proposed a photo-induced generation

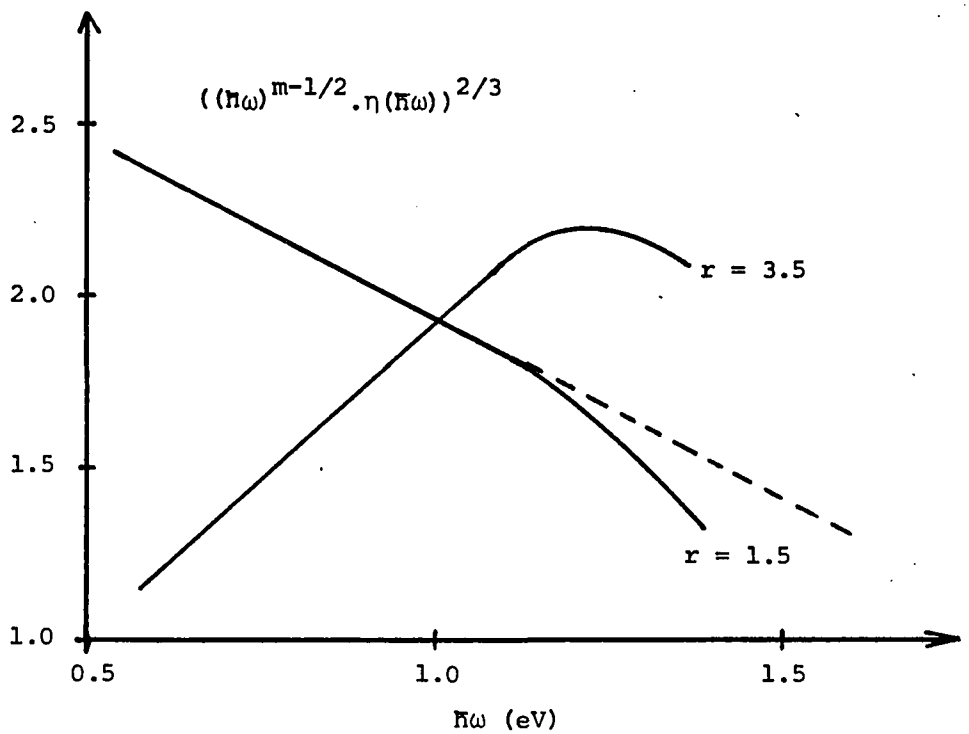

Fig. 2.14. Comparison of the experimental spectral distribution of the quantum efficiency with the theory, for r = 1.5 and r = 3.5 (after Kosyachenko et al., 1984).

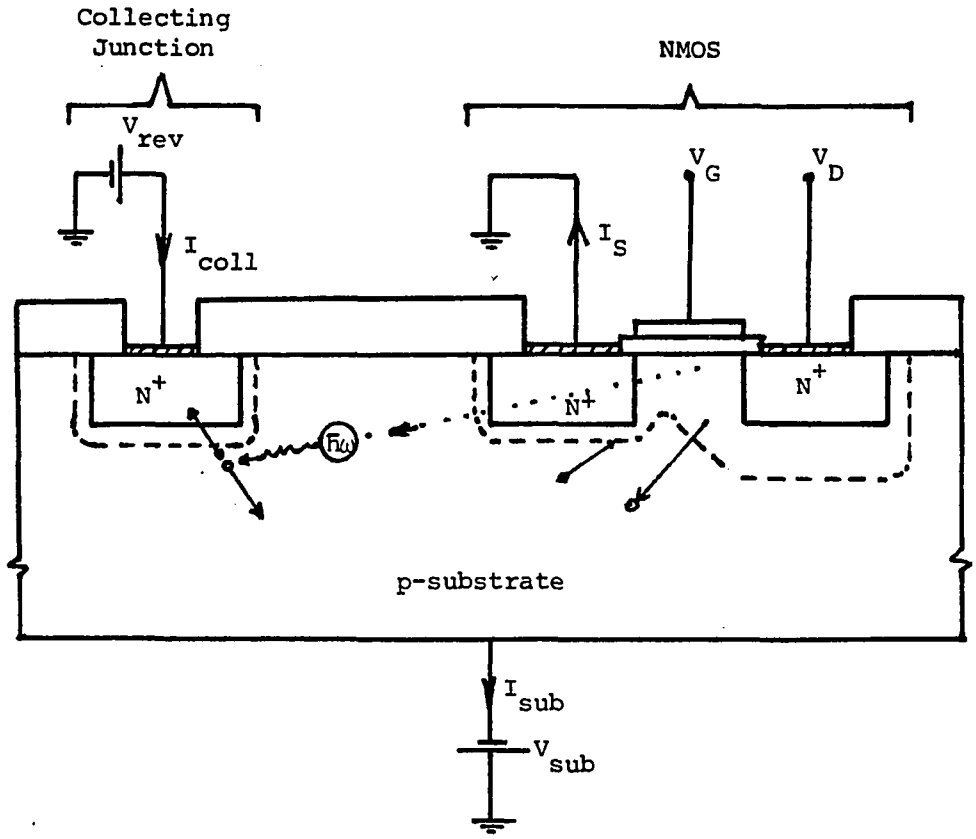

Fig. 2.15. Experimental configuration used in the NMOS wafer (after Tam and Hu, 1984).

process to explain the existence of these carriers. According to their theory, photons are generated in the high channel-field region near the drain of the MOSFET. Some of these photons, which have energies higher than the band gap of silicon can subsequently generate electron-hole pairs in the substrate. Some of the minority carriers may diffuse to the reverse biased "collecting" junction (Fig. 2.15) contributing to the current I_{coll}. Those authors agree that the mechanism and the emission spectrum of the generated light must be the same as the light emission from p-n junctions under avalanche breakdown, although no specific reason is given for this assumption. Based on this assumption, Tam and Hu (1984) studied different mechanisms to determine which one was responsible for light emission. These include: radiative transition of holes between valence bands (Transitions I, IV, V, VI), radiative recombination between a hot electron and a free hole (Transitions II, III, VIII, IX), and scattering of hot electrons by charged coulombic centers (Transition VII). These are all shown in Fig. 2.10. Currents I_{coll}, I_{sub}, and I_{DS} (Fig. 2.15) were measured for different values of V_{GS}, with V_{DS} fixed at 7 V and V_{sub} at zero; also, measurements were taken maintaining V_{GS} fixed and changing V_{DS}. The conclusions of Tam and Hu (1984) are summarized in the following paragraphs.

PMOS devices have a much larger hot-hole population and much higher hole temperature than NMOS; thus, if intraband transitions of holes were the dominant mechanism, the number of photons and so the number of photogenerated minority carriers as well as the collected current I_{coll} would be larger in PMOS than in NMOS. However, since the difference found was less than an order of magnitude, intraband transitions of holes cannot be the cause.

According to the collected data, I_{coll} and hence the photon generation rate are proportional to $(I_{sub})^a$, where a is between 0.7 and 0.9 and independent of I_{DS}. Tam and Hu (1984) consider that the electron density at the drain junction is proportional to I_{DS}, the hole density is proportional to I_{sub}, and the hot electron density is proportional to I_{sub}. If light emission were due to electron-hole recombination, the photon generation rate and the collected current I_{coll} would be proportional to the product of the electron density and hole density, I_{DS} x I_{sub}, or to the product of the hot electron density and hole density $(I_{sub})^2$, and both are in disagreement with data. Thus, radiative electron-hole recombination is not the dominant process.

Tam and Hu (1984) developed a theoretical formulation based on the scattering of hot electrons with impurity centers. Based on a model by Shockley (1961) that gives the

probability P(U) for the channel hot-electrons to attain kinetic energy in excess of U, these authors calculate the number of hot electrons R(U)dUdx passing through the channel with kinetic energy from U to U + dU. Based on a study about X-ray absorption by Kramers (1923), Tam and Hu calculate the probability $Q_\omega d\omega$ of the emission of a photon with energy in the interval $\hbar\omega$ to $\hbar(\omega + d\omega)$ due to one electron passing through a thickness dx containing N_C charged impurity centers per unit volume. Then integrating $Q_\omega d\omega \cdot R(U)dUdx$ along the length of the channel and for initial kinetic energies higher than $\hbar\omega$, Tam and Hu obtain the total energy radiated in the frequency range ω to $\omega + d\omega$, per unit time. The result is written in a simplified form:

$$J_{out}(\hbar\omega) \alpha \frac{N_c}{(\hbar\omega)^2} \cdot e^{-\hbar\omega/q\varepsilon_m\lambda} \qquad (2.21)$$

where ε_m is the maximum channel electric field, i.e., the value at the drain end, and λ is the mean free path of the channel hot electrons due to optical phonon scattering. In addition, Tam and Hu take N_C as the impurity concentration in the drain region. Figure 2.16 shows the spectrum of silicon, by Chynoweth and McKay (1956), similar to Fig. 2.9, which they managed to fit.

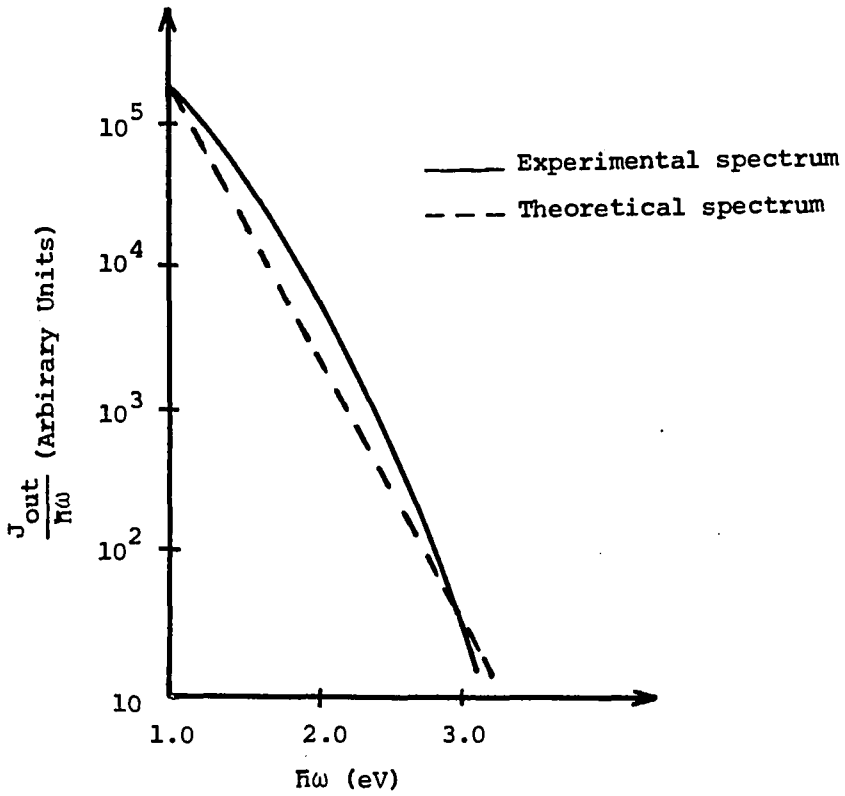

Fig. 2.16. Comparison between the measured photon spectrum (Chynoweth-McKay) and the calculated photon spectrum (after Tam and Hu, 1984).

Tam and Hu also suggested that reducing the drain impurity concentration would probably reduce the photogeneration rate. Ogura et al. (1980) observed a decrease in the substrate current for lightly doped drain-source MOSFETs. That conclusion disagrees with Kosyachenko et al. (1984) study. Also, Tam and Hu did not consider the possibility of scattering with acoustic phonons.

From this information given above, one can see that no agreement exists at present to explain the mechanism responsible for light emission from silicon p-n junctions biased into avalanche breakdown. Several observations about this light emission may be made, however. Under avalanche breakdown, a large generation of electron hole pairs with high kinetic energy occurs, as shown in Section 2.2.2.3 and Fig. 2.8. By spontaneous emission or by interaction with lattice points or impurity centers, those high energy particles, also called hot carriers, may give up part of their energy in the form of a photon. The typical photon spectrum is wideband in nature, extending from less than 1 eV to more than 3 eV in photon energy, and decreasing monotonically more than four orders of magnitude in that interval (Chynoweth and McKay, 1956; Kosyachenko et al., 1984). Also, some diodes of unknown characteristics produce a spectrum with a peak around E_g.

With respect to the absolute values of efficiency and power output, Kosyachenko et al. (1984) claim a quantum efficiency of 10^{-5} photons/electron, and a power output of 10^{-8} watts, without giving data on the power input.

Other qualitative results are given by Das, Khokle, and Mohanty (1985), in working with MOSFET devices. The electric field intensity is a maximum at the most sharply curved place in the junction, so light was first seen at the four corners of the drain region when the voltage was increased and avalanche breakdown was reached. Also, the intensity of the light emission changes with drain and gate bias. In particular, for the simple p-n junction beyond breakdown, light emission intensity is proportional to junction current. This last result was also found by Kosyachenko et al. (1984), who claimed the light output was linear over four orders of magnitude of current input.

2.3 Semiconductor Photodetectors

2.3.1 Optical Absorption

When electromagnetic radiation, e.g., light, is incident on an intrinsic semiconductor, it will be absorbed, or it will pass unattenuated through the material, depending on the wavelength. The optical absorption is very small for photon energies less than E_g, the energy band gap, and large for photon energies larger than E_g. The absorption also depends on the thickness of the sample. Figure 2.17 shows

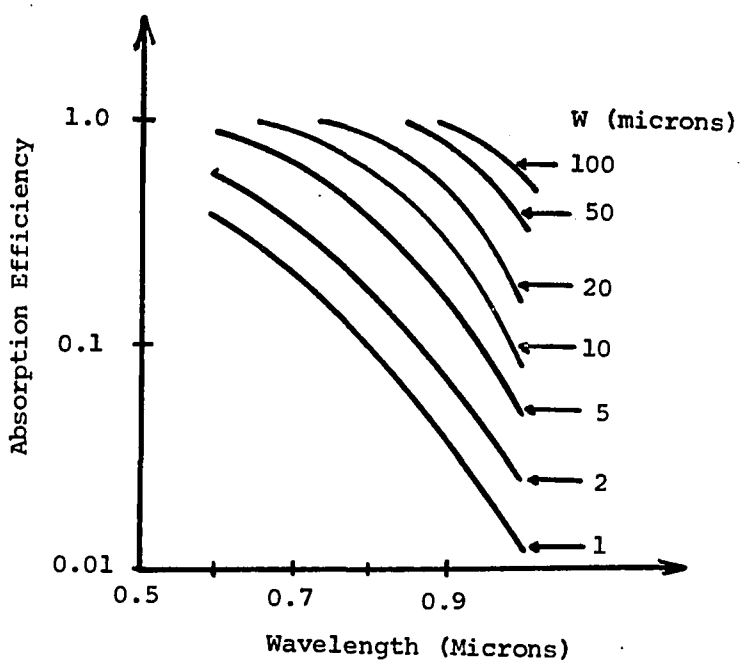

Fig. 2.17. Absorption efficiency as a function of wavelength and thickness (after Kressel, 1980).

the absorption efficiency as a function of wavelength and thickness. An absorption efficiency of 1.0 corresponds to 100% absorption.

2.3.2 Detectors

A photoconductor consists basically of a bulk semiconductor sample with ohmic contacts at both ends. When illuminated with light of the appropriate wavelength, i.e., with photon energy, $\hbar\omega$, larger than the energy band gap E_g, light is absorbed; thus, electron hole pairs are generated, thereby increasing the bulk conductivity. The optical generation rate, g_{op}, is the number of electron hole pairs/cm^3sec. In steady state the following equation gives the conductivity change:

$$\Delta\sigma = q.g_{op}.(\tau_n\mu_n + \tau_p\mu_p) \qquad (2.22)$$

where μ_p and μ_n are the carrier mobilities, and τ_p and τ_n the lifetimes. High mobilities and long lifetimes are preferred in order to have maximum photoconductive response. However, long lifetimes limit the operating frequency of the device.

Junction devices can be used to improve the speed of response and sensitivity of detectors, mainly for optical and high-energy radiation. Specifically, single-junction detectors are called photodiodes. If the photodiode is illuminated laterally, as shown in Fig. 2.18, a new

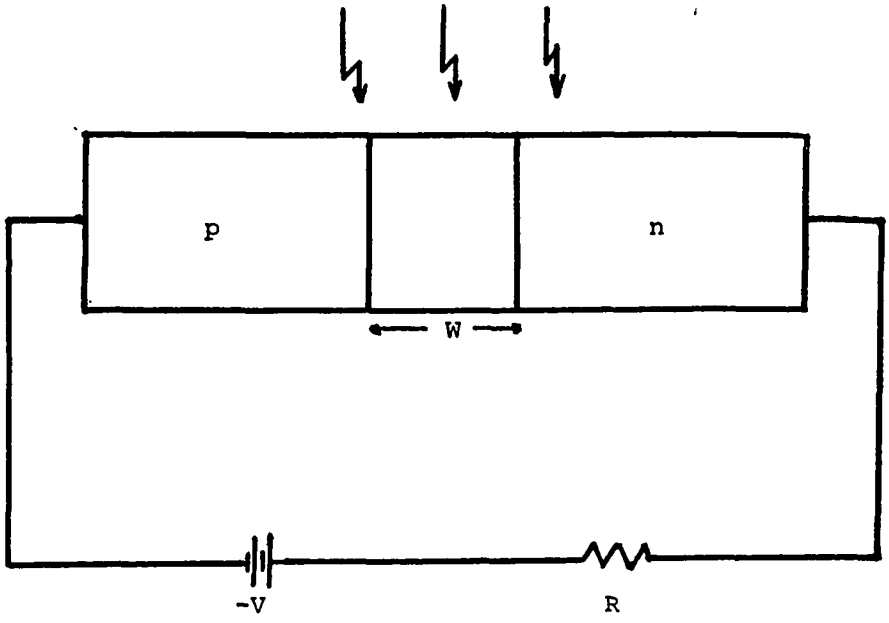

Fig. 2.18. p-n junction laterally illuminated. -- The diode is shown reverse biased.

component of current must be considered, proportional to the optical generation rate, g_{op}, and to the volume in which a generated minority carrier may diffuse to the junction and contribute to the drift current. Thus, for a photodiode under illumination, the current through the diode resulting from the photogenerated carriers, I_{illum}, is given by:

$$I_{illum} = q.A.g_{op}.(L_p + L_n + W) \qquad (2.23)$$

and the total current, I_{Total}, is then:

$$I_{Total} = I_o(e^{qV/kT} - 1) - q.A.g_{op}.(L_p + L_n + W) \qquad (2.24)$$

Working in the third quadrant of the I-V characteristic, under reverse bias, the current is independent of voltage, but proportional to the optical generation rate.

When a fast response is necessary, the generation of minority carriers outside the depletion region is undesireable because of the time it takes them to diffuse to the junction. Thus, it is better to have a wider depletion region to absorb most of the light. This can be accomplished using a PIN diode.

If very small signal levels must be detected, the sensitivity can be increased by reverse biasing the diode just below the point of avalanche breakdown. Then a large carrier multiplication occurs under illumination.

2.4 Optical Waveguides

The optical waveguide (Hunsperger, 1984) is the basic element that allows an interconnection between optical devices, as a metallic strip does between electronic devices in an integrated circuit. Optical waveguides are difficult to design because of the existence of different transmission modes. These modes have different spatial distributions of the electromagnetic energy through the waveguide, with unfavorable effects. For simplicity, consider a three-layer planar waveguide, shown in Fig. 2.19, with indices of refraction for the three layers:

$$n_2(\text{center}) > n_3(\text{bottom}) \geq n_1(\text{top}) \qquad (2.25)$$

and transmission in the z direction.

2.4.1 Ray-optic Approach

This approximation considers the light propagating in the z direction that is composed of plane waves moving in zig-zag paths in the x-z plane undergoing total internal reflections at the interfaces bounding the waveguide as shown in Fig. 2.19. The plane waves are usually represented by rays drawn perpendicularly to the planes of constant phase. All the plane waves travel with the same phase velocity, but are reflected at different angles, each one defining a mode of transmission and its associated z-component of phase velocity. Thus, each mode advances at

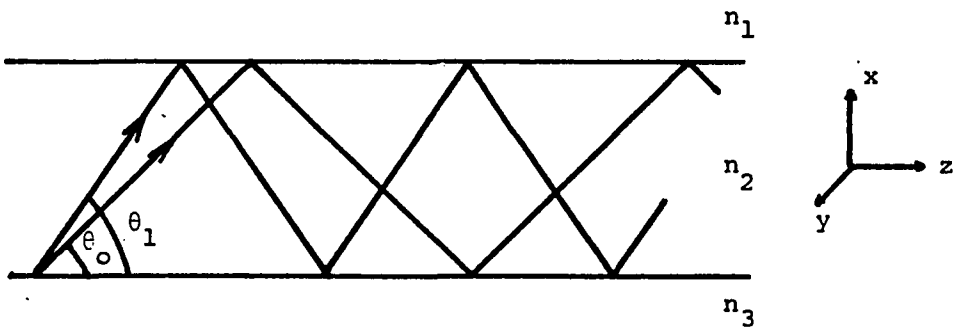

Fig. 2.19. Optical ray pattern within a multi-mode planar waveguide (after Hunsperger, 1984).

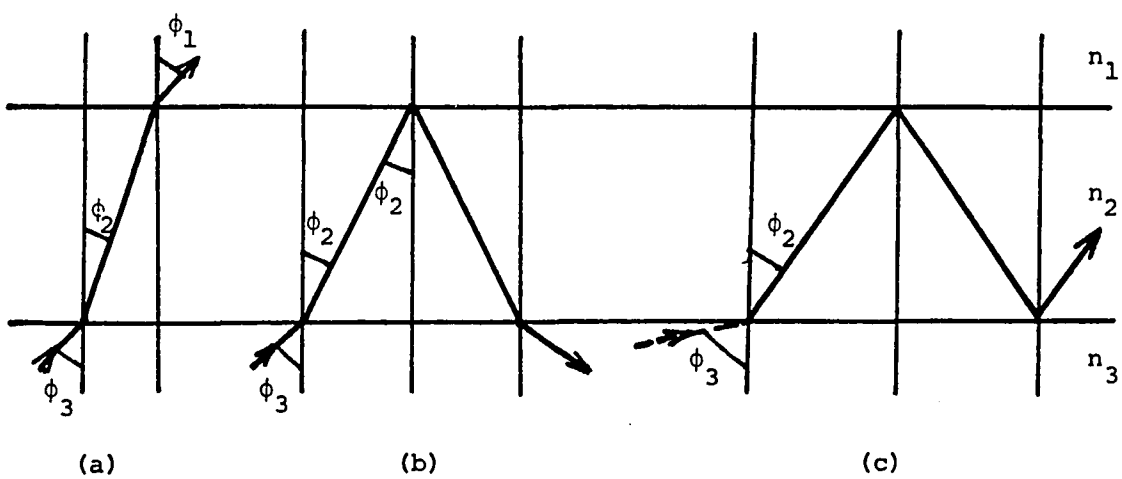

Fig. 2.20. Ray patterns according to incidence angle (after Hunsperger, 1984). -- (a) Radiation mode; (b) Substrate mode; and (c) Guided mode. Situation (c) is physically impossible (see text).

a different velocity; hence, different modes of light coupled in phase at one end of the waveguide reach the other end at different times. This phenomenon, known as dispersion, limits the operating frequency of the system.

A simple, although incomplete, understanding of the transmission of light in the three-layer guide is obtained with the help of the classical Snell's laws of optics. The light rays of Fig. 2.20a through c correspond to three basic situations: radiation mode, substrate mode, and guided mode. According to Snell's laws:

$$\frac{\sin\phi_1}{\sin\phi_2} = \frac{n_2}{n_1} \tag{2.26a}$$

and

$$\frac{\sin\phi_2}{\sin\phi_3} = \frac{n_3}{n_2} \tag{2.26b}$$

Beginning with small angles of incidence ϕ_3, the light ray that comes from the bottom medium is refracted at both boundaries. This situation is called a radiation mode (Fig. 2.20a); light is radiated to the top medium.

When ϕ_3 is increased, total internal reflection occurs at the boundary between the center and the top media. This situation is called a substrate mode (Fig. 2.20b); light is directed back to the bottom medium. The condition for this to happen is:

$$\phi_2 = \sin^{-1}\left(\frac{n_1}{n_2}\right) \tag{2.27a}$$

or, using Eq. 2.26b

$$\phi_3 = \sin^{-1}(\frac{n_1}{n_3}) \qquad (2.27b)$$

In principle, increasing ϕ_3 still more, total internal reflection takes place at the boundary between the center and bottom media and the light becomes totally confined. This case is called a guided mode (Fig. 2.20c). The condition for this to happen would be:

$$\phi_2 = \sin^{-1}(\frac{n_3}{n_2}) \qquad (2.28a)$$

or, using Eq. 2.26b,

$$\phi_3 = \sin^{-1}(1) = 90^{o} \qquad (2.28b)$$

This condition is physically unrealizable and shows the need for coupler devices in order to have a guided mode, which will be considered below.

2.4.2 Improvements to the Ray-optic Model

In the preceding treatment, it was assumed that light rays corresponding to each mode were distributed continuously in every direction. Because of the destructive interference of plane waves with their reflected counterparts, only a discrete set of modes can travel through the waveguide without an energy decay (Hunsperger, 1984).

Until now, when waveguiding occurs, the energy has been considered confined entirely to the middle dielectric. This is not true. From an electromagnetic point of view, or physical optics approach, in order to satisfy boundary conditions, it is shown that the "confined" or "guided wave" fields have "tails" which extend into the other two media. The tails decrease exponentially with distance to negligible values within a wavelength from the boundary with the center region. In addition, in the confined region the field varies sinusoidally, having different distributions according to the mode, as shown in Fig. 2.21.

2.4.3 Coupling

Many systems exist for coupling the optical energy into or out of a waveguide, such as transverse couplers, prism couplers, grating couplers, and tapered couplers, each one with advantages and disadvantages according to the situation. For the purpose of this thesis, the tapered coupler is considered.

The tapered coupler (Hunsperger, 1984; Tien and Martin, 1971) is made by progressively reducing the thickness of the waveguide to zero as shown in Fig. 2.22. When a guided ray enters the tapered region, it undergoes successive reductions in the incident angle until it is too small to produce a total internal reflection, thereby transferring its energy to the substrate. It takes about

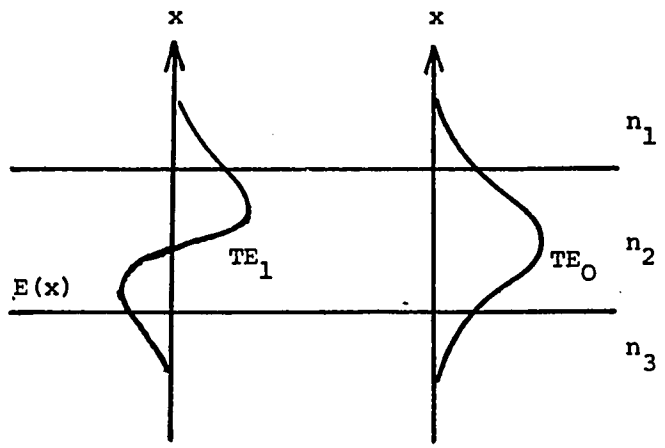

Fig. 2.21 Two electromagnetic modes in a planar waveguide (after Hunsperger, 1984).

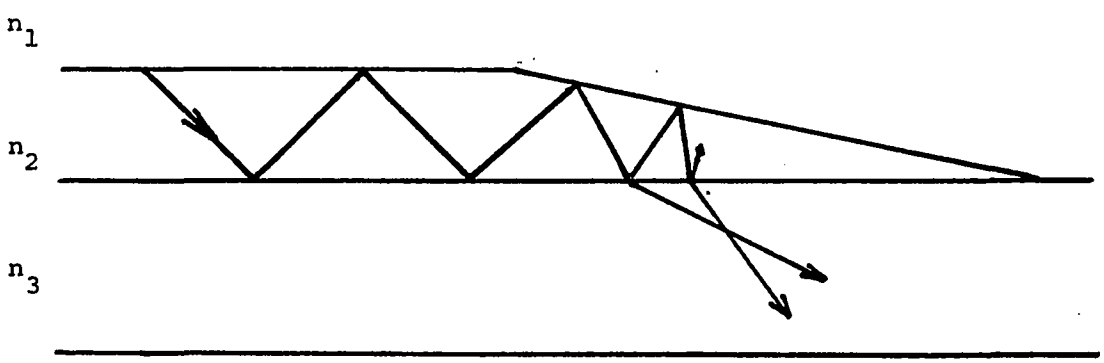

Fig. 2.22. Diagram of a tapered coupler (after Hunsperger, 1984).

eight vacuum wavelengths after refraction to the substrate begins to have a coupling efficiency of 70%. The tapered coupler is easy to fabricate and works well as an output coupler, but forms a divergent beam with a spread up to 20^{o} (Fig. 2.22). The reverse situation is theoretically possible. Light rays with the same direction as in Fig. 2.22 generated in the substrate will be refracted to the center medium and form guided modes. However, since we had a divergent beam before, in order to reconstruct the guided modes, a convergent beam must be generated in the substrate. This needs a converging lens in the integrated circuit. As this solution is practically impossible, only very low efficiencies can be obtained at the input coupler end.

2.4.4 Materials for Optical Waveguides

These materials must have low attenuation at operating frequencies and higher index of refraction than the surrounding media. One of the most important is zinc sulfide (ZnS), a direct band gap semiconductor with E_g = 3.6 eV, an index of refraction 2.3, and a resistivity 10^{10} ohm-cm at 300^{o}K. Chemically, ZnS is a salt and passes into solution when it comes into contact with acids, especially strong acids (HCl, HNO_3, H_2SO_4). For example, with hydrochloric acid it gives zinc chloride and hydrogen sulfide (Ehret, 1947).

Another important material is silicon nitride (Si_3N_4) with a band gap of 4.5 eV and an index of refraction of 2.03. No further details are given because it is not used in this thesis.

CHAPTER 3

STUDIES ON SILICON LIGHT EMITTING DEVICES

3.1 Introduction

This chapter covers the design and fabrication of light emitting diodes used as light sources, followed by the presentation and discussion of the experimental results. The first section reviews briefly previous work performed within the Microelectronics Laboratory (MEL) of the University of Arizona.

The design and layout of the diodes to be used in this study are given in the next two sections. In order to learn as much as possible about the effect of device structure, including the interconnect layout on the performance of the device, and to confirm or reject previous conclusions, a number of layout patterns were developed which were incorporated into the final mask set.

The section on experimental results presents the measured results obtained on these devices. Device parameters such as breakdown voltages and series resistance values, spectra, power output, and efficiency are given.

In the last section, quantitative and qualitative results are summarized and compared with the expected ones.

3.2 Previous Research at the MEL

As a consequence of some exploratory work done in the last years at MEL of the UA, different opinions developed concerning the patterns and concentrations necessary for light emission to occur. It was considered that patterns diffused over previous diffusions, like common bipolar transistors in which impurity compensation takes place, would not emit light. Although the problem was not studied theoretically, no record existed of light emitted in such common situations. Light emission would take place with abrupt junctions, without significant impurity compensation. Also, it was believed that contact distances to the junction influenced the light emission. Theoretically, no major influence over the electric field would occur for contacts laid out of the depletion region.

Furthermore, one spectral measurement made using a grating and a photographic system disagreed with the spectra found in the literature, as reviewed in Section 2.2.3. This measurement showed a peak in the visible part, around green, with a decrease for larger wavelengths. Hence, those exploratory results introduced doubts about their reliability , and further work and study were considered necessary.

3.3 Pattern Design-Layout

Since it was not known which structures would emit light, nor what might be the most effective structure for

the light emitting diodes, a number of possible structures was investigated. Three basic types were considered to determine differences in efficiencies, power outputs, and in the physical location of light emission. The three structures are called overlap type, gap type, and abutting type, and are described below. Within each basic structure, variations exist in geometries, dimensions, and contact to contact distances, and are also described below. A general layout is shown in Fig. 3.1. The devices in a row are numbered from right to left, and the rows are numbered from top to bottom.

In the overlap structure (Fig. 3.2), p^+ and n^+ regions are laid out with a common region 0.2 mils wide at the mask level (the "overlap" region) between them, and in this situation, impurity compensation occurs. No theoretical consideration, as reviewed in Section 2.2.3, contradicts the emission of light from the junction.

In the gap structure, p^+ and n^+ regions are laid out separated by a gap of p^-, the substrate, 0.2 mils wide at the mask level, like a p-i-n structure (Fig. 3.3). The depletion region is located between the p^- and n^+ regions, and extends mainly into the p^- region. According to Figielski-Torun's model (Section 2.2.3), the intensity of the light emission is larger for higher impurity concentrations. If this is right, most of the light must come from

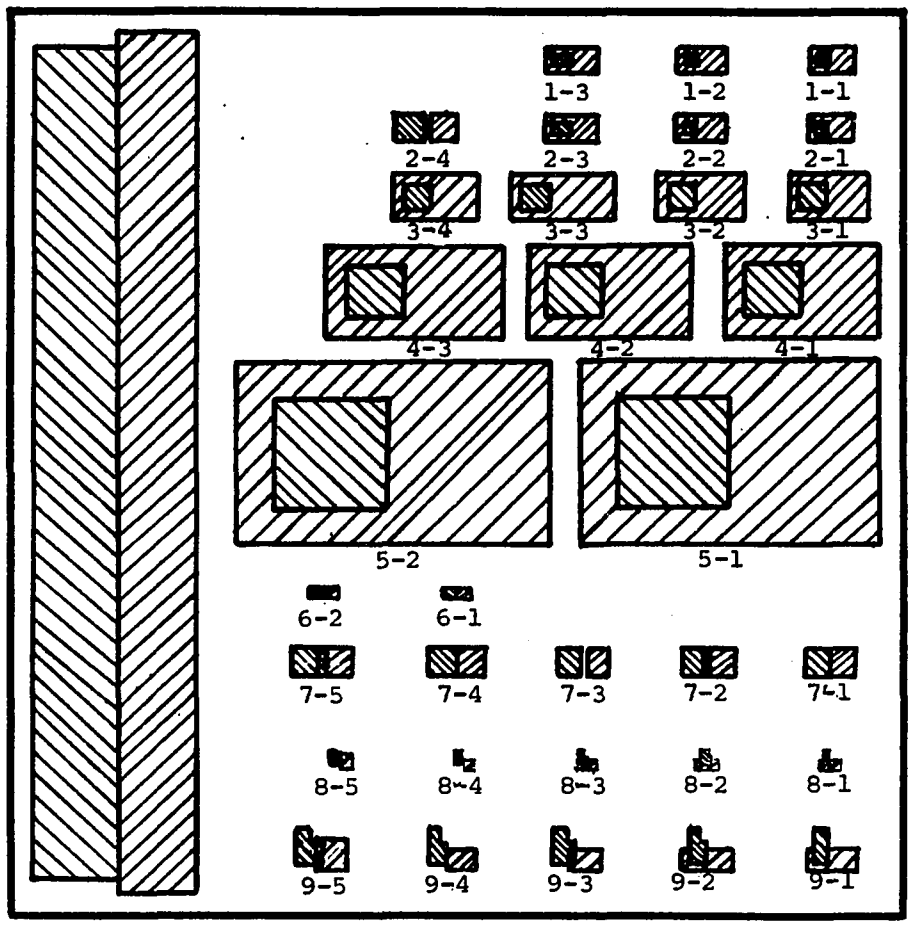

Fig. 3.1. General layout. -- Only p^+ and n^+ regions are drawn.

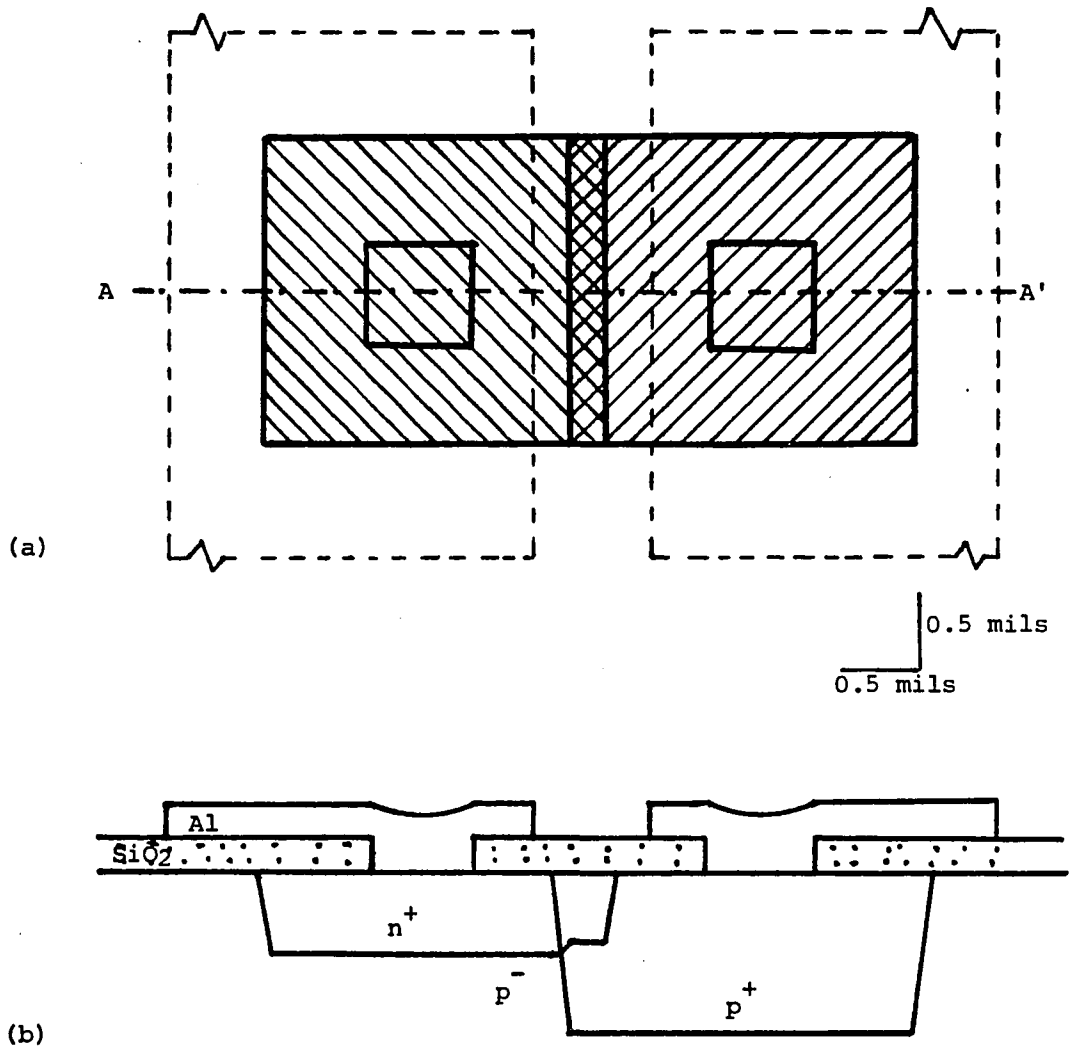

Fig. 3.2. Overlap structure, device 7-5. -- (a) Layout; and (b) Cross-section A-A'. The change in junction depth of the n^+ diffusion is due to the different concentrations of the p^+ and p^- regions.

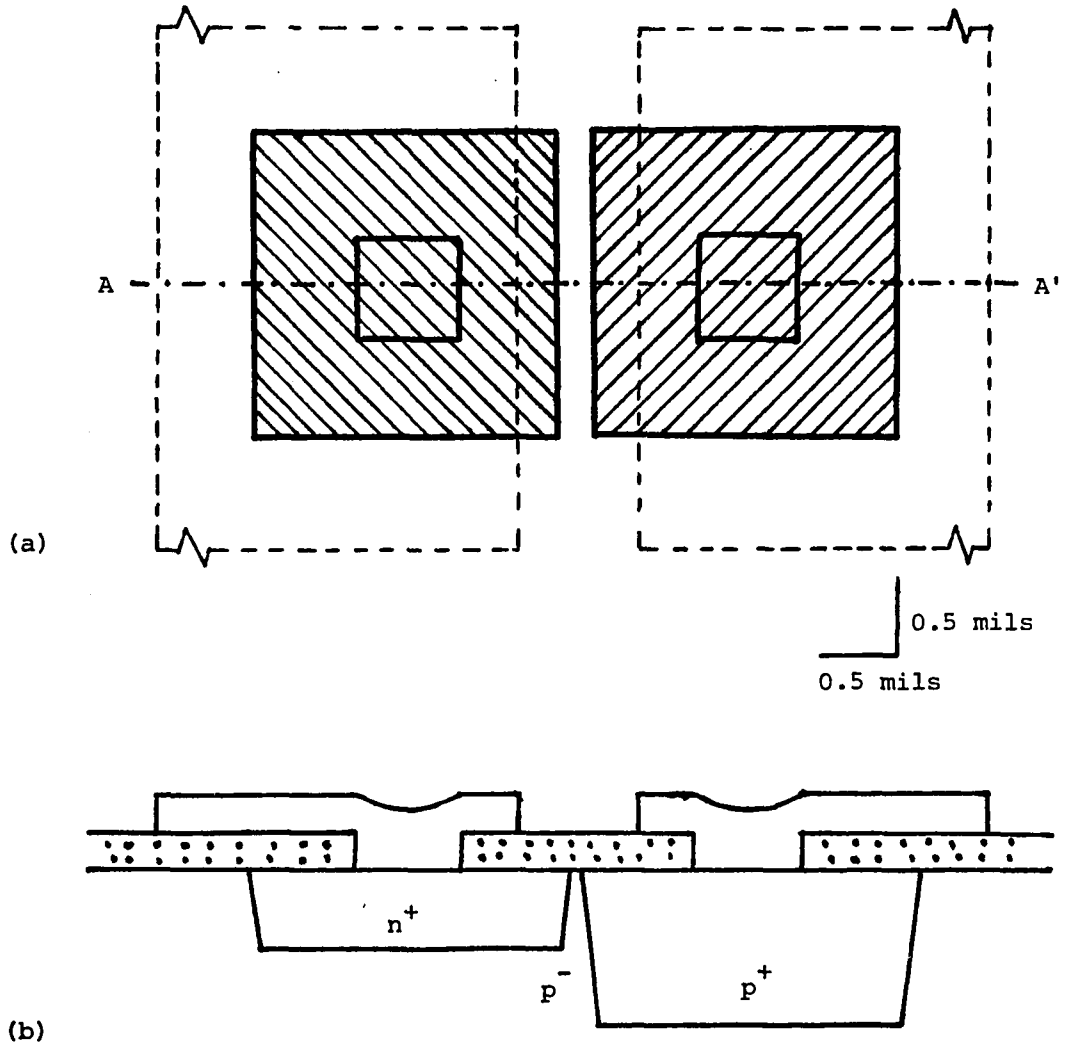

Fig. 3.3. Gap structure, Device 2-4. -- (a) Layouts; and (b) Cross-section A-A'.

the n^+ region and not from the p^- region. If it is wrong, a broader line of light than in the overlap structure will probably be seen because of the light generated in the p^- and p^+ depletion regions.

In the abutting structure (Fig. 3.4), the p^+ and n^+ regions are laid out such that they touch at the mask level. Due to process and equipment limitations, an overlap or gap between the two regions was the result, which makes this structure similar to the preceding ones.

Two other structures which may be derived from the preceding ones were considered. Figure 3.5 shows a pattern in which the n^+ region is completely diffused into the p^+ region. This structure is considered a special situation of the overlap structure, and corresponds to the typical emitter-base layout of a bipolar transistor.

Figure 3.6 shows a pattern in which p^+ circumscribes n^+, the structure being a variation of the abutting type. Basically, this pattern was the one previously tested at MEL, and it was found to emit light.

The patterns designed for optical interconnection purposes deserve special consideration, and their design was based on the following principles. The light is expected to come from a straight line above the junction. The waveguide has to be positioned above it, in order to couple the light adequately using a 45° tapered end, as shown in Fig. 3.7.

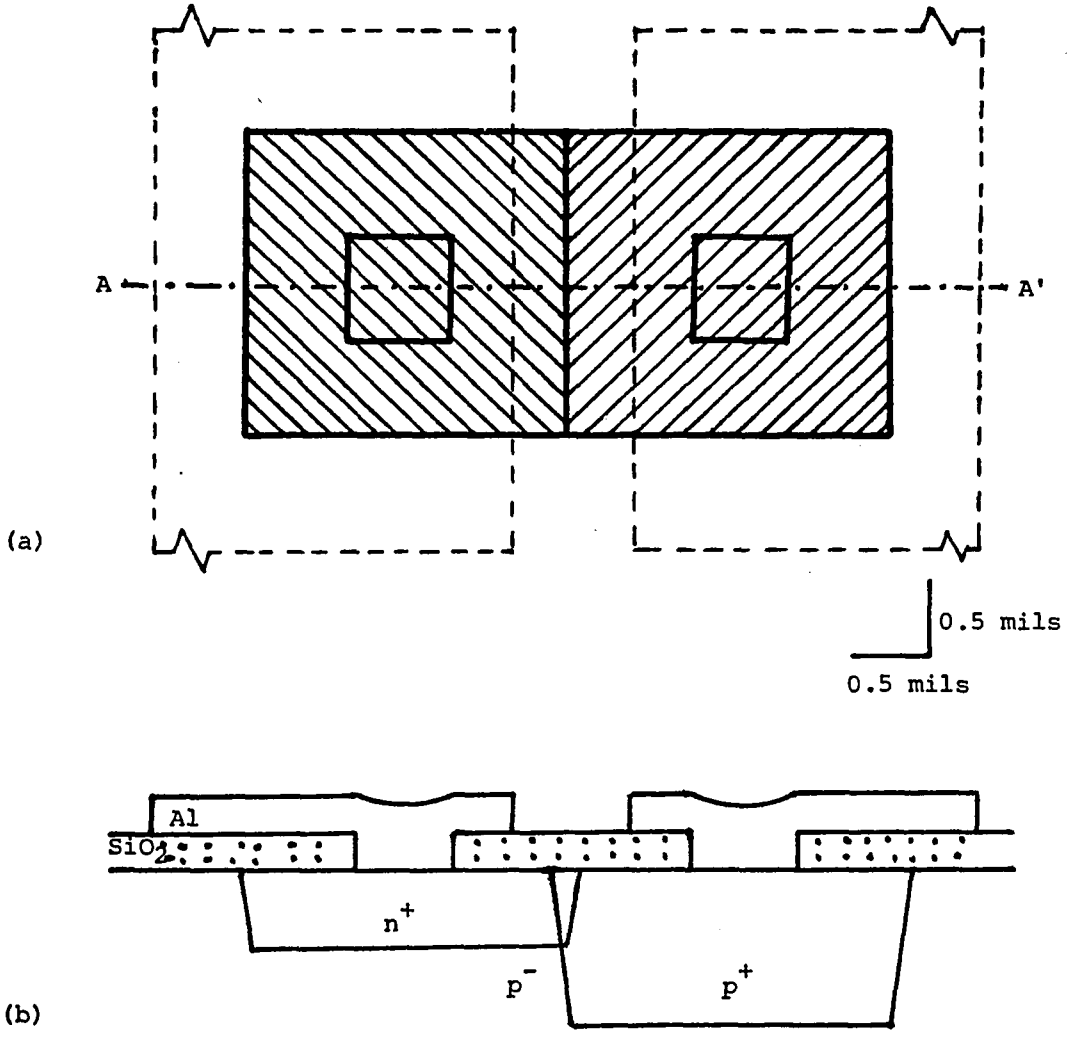

Fig. 3.4. Abutting structure, Device 7-4. -- (a) Layout; and (b) Cross-section A-A'. p and n regions are laid out such that they touch at the mask level.

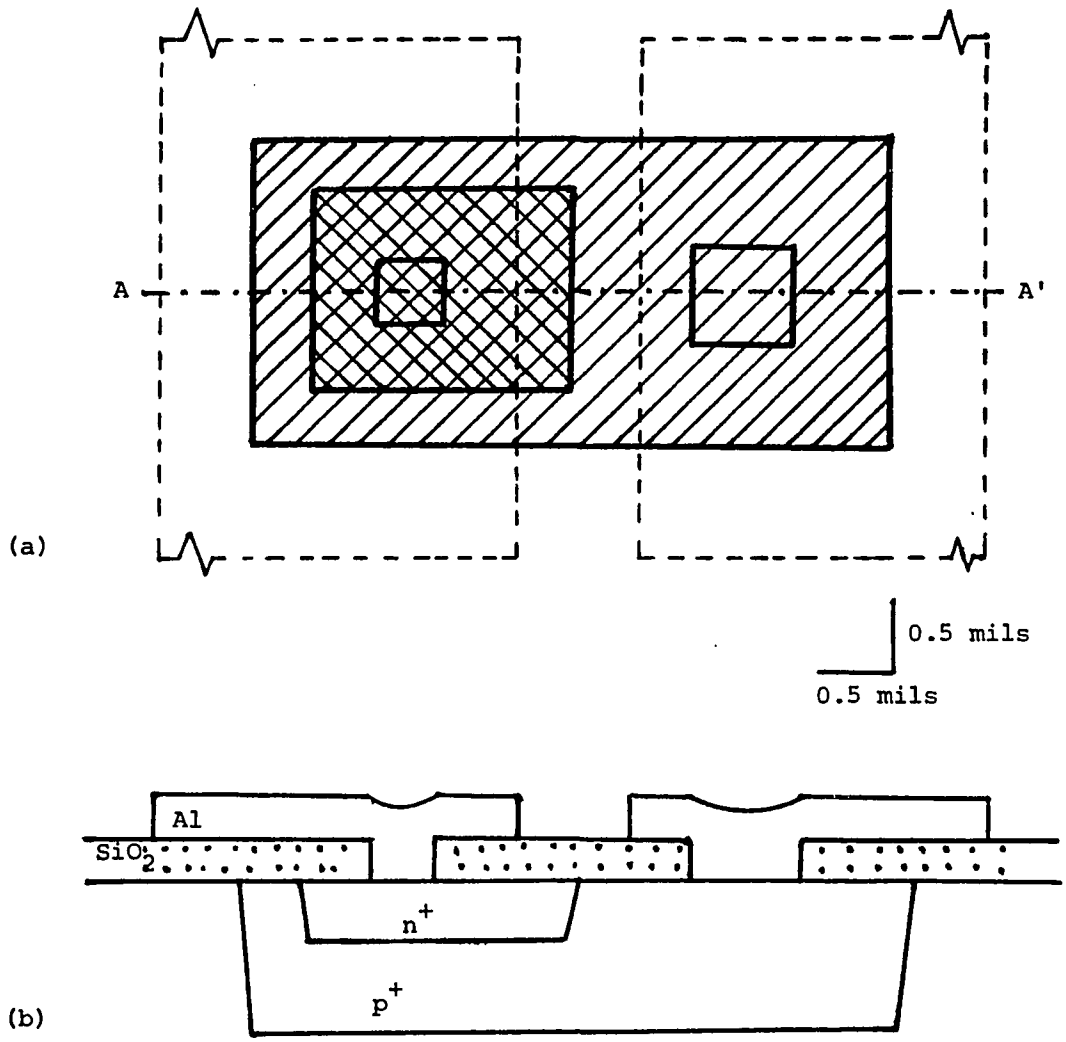

Fig. 3.5. Diffusion over diffusion structure, Device 1-3. -- (a) Layout; and (b) Cross-section A-A'.

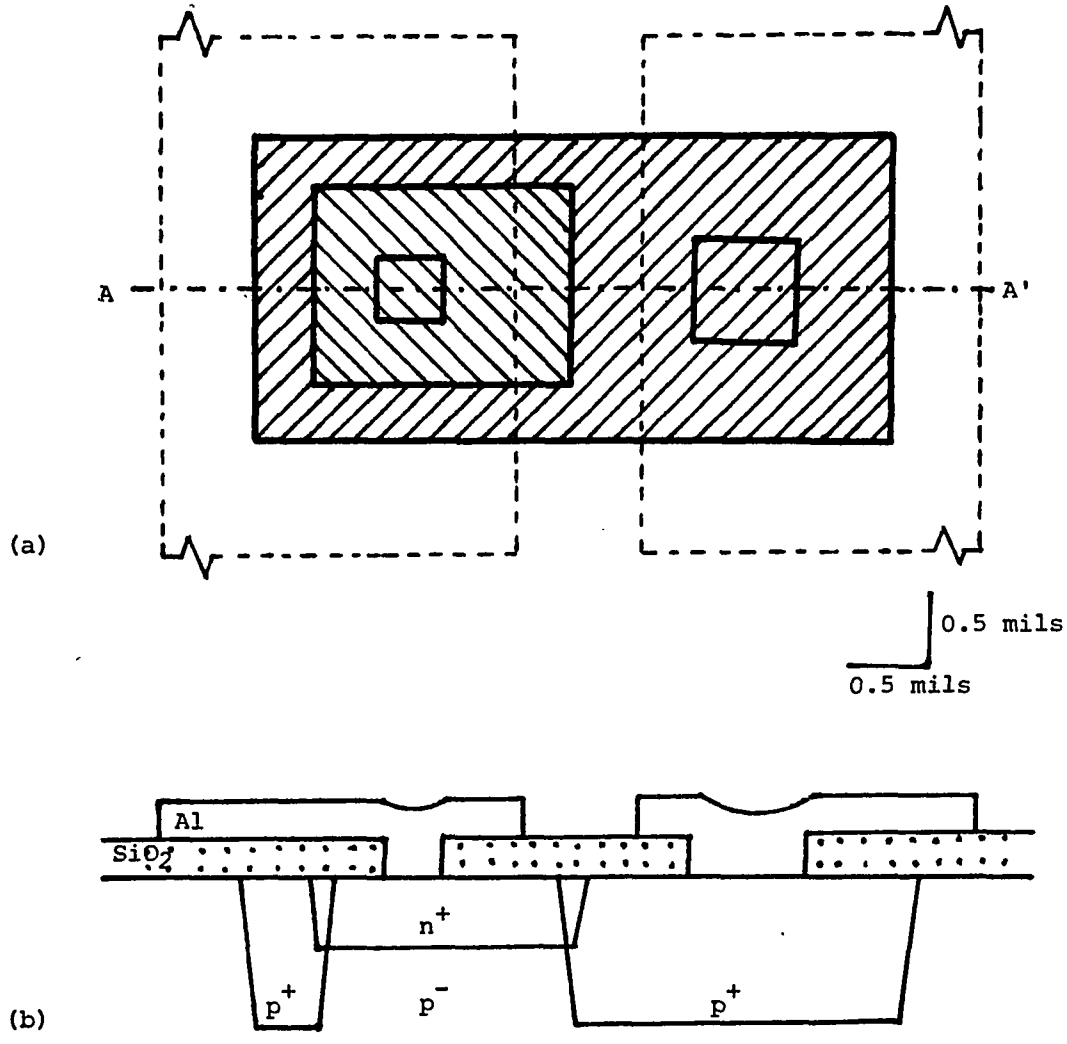

Fig. 3.6. Circumscribed structure, Device 2-3. -- (a) Layout; and (b) Cross-section A-A'. The n^+ region is diffused in a window of p^-.

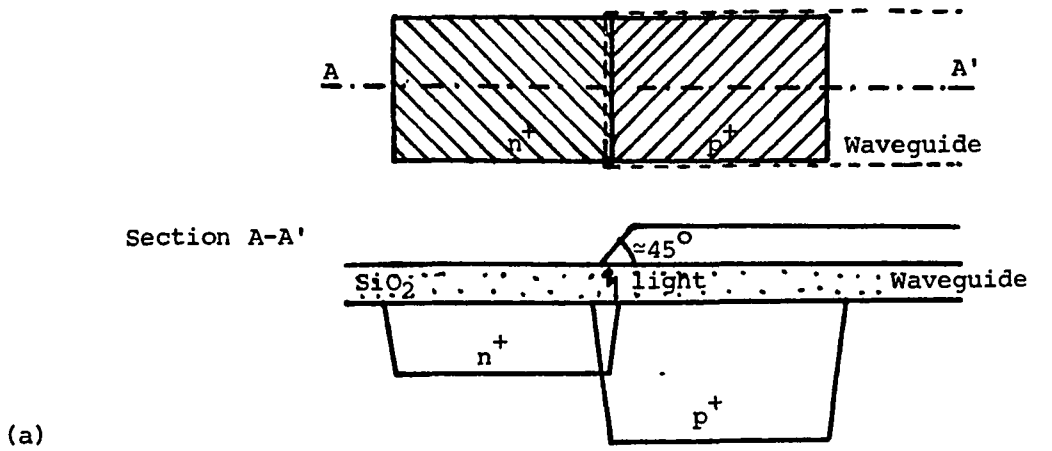

(a)

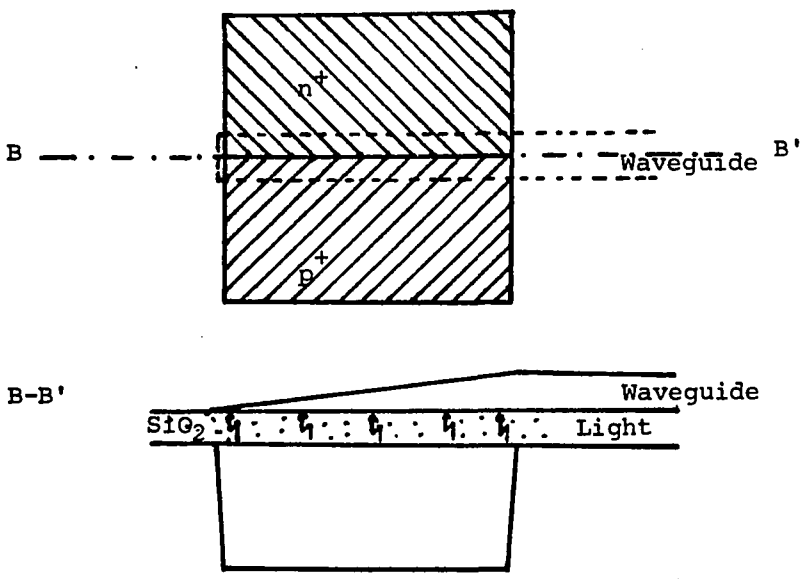

(b)

Fig. 3.7. Necessary location of waveguide, for LED design. -- (a) Waveguide and LED crossed; and (b) Waveguide along the LED. For the waveguide located along the line of light emission (b), the tapered angle must be very small, giving low coupling efficiency. On the other hand, layout (a) gives high coupling efficiency.

(See also the process design in Section 3.4.) Two coupling techniques are shown. In order to collect most of the light the taper should have a very small angle at the base which, as seen in Section 2.4.3, is known to give very low coupling efficiency, at the light source end of a waveguide. Based on that principle, many conditions must be satisfied.

If the aluminum contact were laid out over the waveguide, the contact window would be an obstacle for the light to be transmitted. If the waveguide were over the aluminum, the steps up and down at the edges of the aluminum pads, would decouple most of the light. If the aluminum and waveguide were deposited one over the other, the energy tails contained in the aluminum (discussed in Section 2.4.4 and shown in Fig. 2.21) would be absorbed; thus, an electromagnetic energy transfer to that medium would be present, and would reduce the amount of light reaching the detector. The design of these waveguide structures was basically the same for the overlap, gap, and abutting device configurations; but it was considered convenient to investigate their operation, taking into account the large amount of space available over the die. These waveguide structures were laid out in Rows 8 and 9, Fig. 3.1. Device 9-5 is shown in detail in Fig. 3.8.

Since the literature gave very little information about absolute values of light output (a very small value

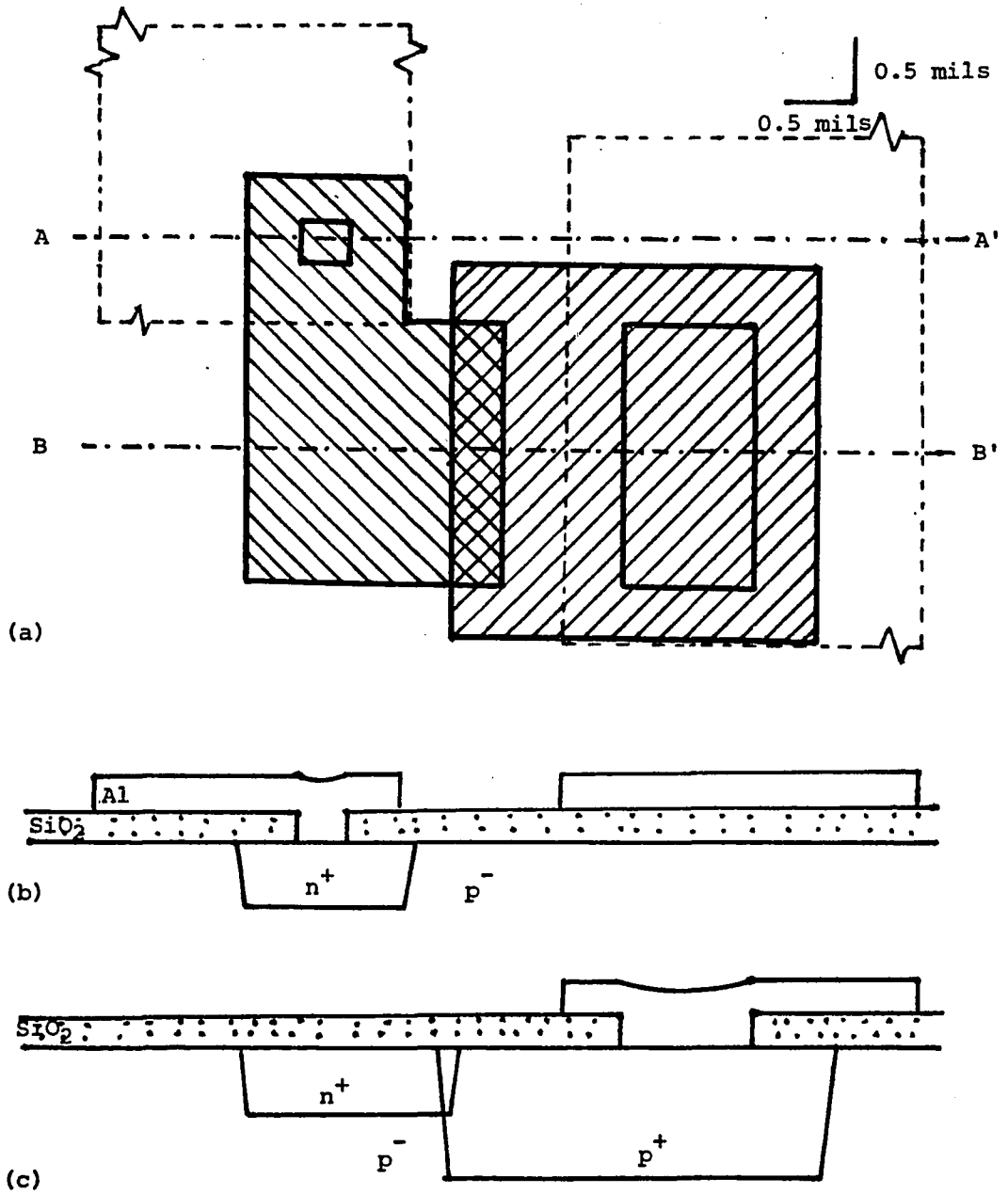

Fig. 3.8. Diode for optical interconnections, Device 9-5. -- (a) Layout; (b) Cross section A-A'; and (c) Cross section B-B'.

10^{-8} W was given), a large light emitting device was laid out in case it was impossible to make measurements in the other diodes. For this reason, the device numbered 0 (Figs. 3.1 and 3.9) was laid out with the other patterns. It consisted of a diode with the abutting structure with a junction length, i.e., the abutting length at the mask level, of 70 mils.

Within each type of basic structure, patterns of different sizes were laid out in rows. Each row had different dimensions in order to find the changes in light emission efficiencies. This is shown in Fig. 3.1.

Devices in Row 1 have a diffusion over diffusion structure (Fig. 3.5). Devices 1-1 and 1-2 have a junction length at the mask level of 4.8 mils, and Device 1-3 a junction length of 5.6 mils.

Devices in Row 2 have a circumscribed structure (Fig. 3.6). Devices 2-1 and 2-2 have a junction length of 4.8 mils and Device 2-3 a junction length of 5.6 mils.

Devices in Row 3 have a circumscribed structure (Fig. 3.6) and a junction length of 9.6 mils.

Devices in Row 4 have a circumscribed structure (Fig. 3.6) and a junction length of 19.2 mils.

Devices in Row 5 have a circumscribed structure (Fig. 3.6) and a junction length of 38.4 mils.

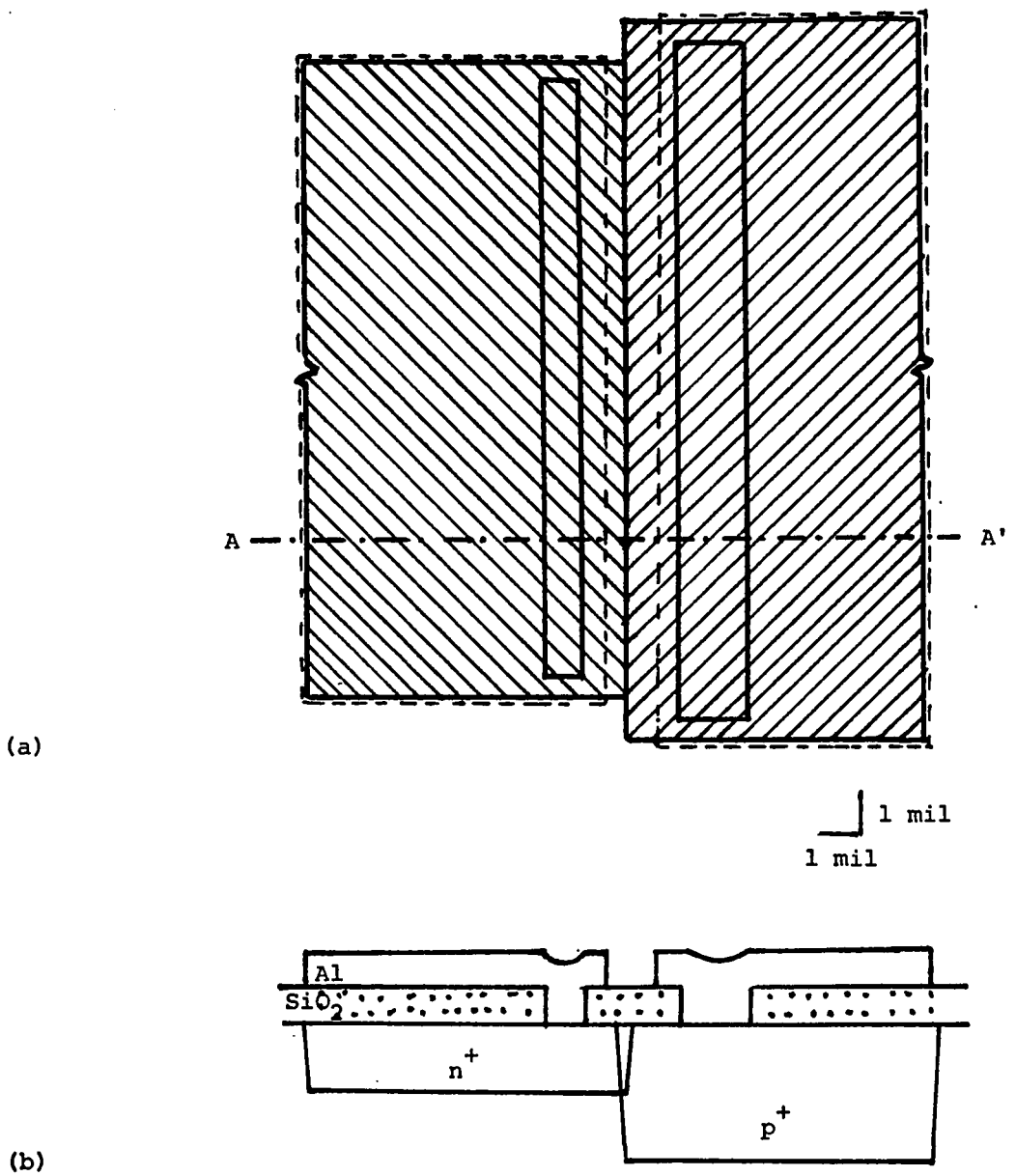

(a)

(b)

Fig. 3.9. Type O device. -- (a) Layout; and (b) Cross section A-A'. This device has the abutting structure. The drawing has been shortened. Total junction length 70 mils.

Device 6-1 has an abutting structure (Fig. 3.4), and Device 6-2 has an overlap structure (Fig. 3.2), both with a junction length of 0.8 mils.

Devices 7-1 and 7-4 have an abutting structure (Fig. 3.4), Devices 7-2 and 7-5 have an overlap structure (Fig. 3.2), and Devices 7-3 and 2-4 have a gap structure (Fig. 3.3). All these six devices have a junction length of 2.4 mils.

Devices in Rows 8 and 9 are for optical interconnection purposes (Figs. 3.8 and 3.1). The p^+-n^+ junction region has an abutting-type structure in Devices 8-1 (1.4), 8-2 (1.6), 8-4 (0.4), 9-1 (4.4), 9-2 (4.8), and 9-4 (1.6), and an overlap-type structure in Devices 8-3 (0.6), 8-5 (1.0), 9-3 (2.0), and 9-5 (2.8). The junction length of each device has been specified in mils in parentheses.

The type 0 device has an abutting structure and a junction length of 70 mils.

In addition, for each basic structure and each size, different distances between aluminum contacts were considered within each row of devices. As these variations did not show any influence in the results, neither in electrical nor optical qualitative, they are not described.

3.4 Selected Process

As was discussed in Section 2.2.3, light emission occurs under avalanche breakdown. Also, light emission

close to the surface of the wafer is desirable in order to avoid absorption by the silicon. Furthermore, light generated from a single "line" instead of a whole region is adequate for coupling techniques when using a tapered coupler at 45° to the base. The basic structures already described (overlap, gap, and abutting types, Figs. 3.2 through 3.4) fulfill those requirements. The diffusion process is characterized by the presence of higher impurity concentrations at the surface level and by lateral diffusions of curved shape. These characteristics give higher electric fields at the surface and the lateral junctions. Thus, avalanche breakdown occurs at those areas first (see Section 2.2.2).

Doping levels define the breakdown voltage (BV) and series resistance. A relatively low BV is preferable which allows compatibility with other electronic circuits. Hence, a BV in the range of 5 to 10 V was selected.

There is a standard, well-known process in MEL which gives devices with good characteristics and a BV of the order of 7 V in the emitter junction. This process is described in the Laboratory Manual for the course ECE 457 (Fordemwalt et al., 1985) under "Experiment 7: ECL gate." Figure 3.10 shows the impurity profiles and junction cross sections. The emitter sheet resistance is about 5 Ω/□ and the base sheet resistance is about 180 Ω/□.

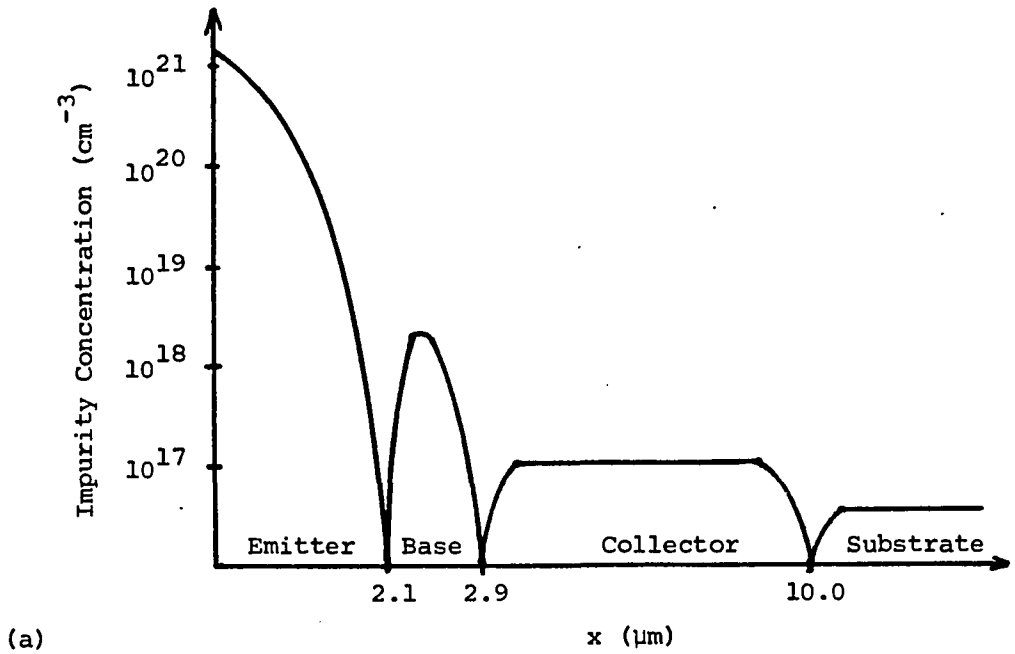

(a)

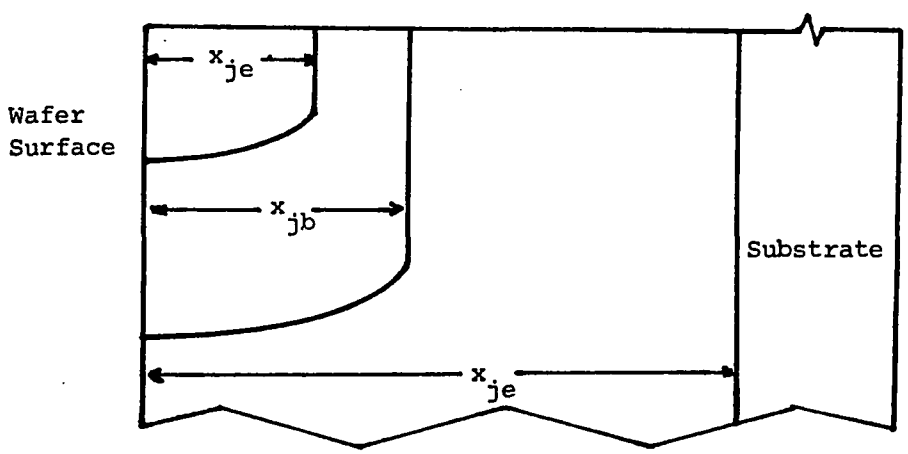

(b)

Fig. 3.10. ECl-Gate profile and cross section (after Fordemwalt et al., 1985). -- (a) Impurity profile; and (b) Junction cross section.

For the light emitting device, our interest is centered in the depletion region and the efficiency of the light emission process. Therefore, we want to have low voltage drops and power dissipation in the p^+ and n^+ regions. Thus, the sheet resistances in both regions must be low. By doing a dry oxidation before the steam one in the p^+ diffusion process, the p^+ sheet resistance is reduced to less than 1 Ω/□. This method is described later. Two pre-drive temperatures were tested, 950°C and 1000°C. During pre-drive the surface concentration remains constant, and the concentration follows a complementary error function curve. Hence, higher pre-drive temperatures give higher concentrations at a certain depth; thus, for example, for the overlap structure a slightly higher concentration will be present at the junction. So, a slightly lower BV and series resistance is expected with the higher pre-drive temperature (see Section 2.2.2.3). However, the already discussed dry oxidation determines the main characteristics of the devices because of its still higher temperature, and makes that distinction in pre-drive temperatures of little influence in the results.

A substrate with fairly high resistivity was preferred for giving an intrinsic-like region in the gap structure devices. The wafers used were p-type, ‹111› orientation, with a resistivity of 5 Ω-cm.

Figures 3.11 and 3.12 show the approximate concentrations and junction depths expected from the chosen process for the gap and overlap structures, calculated by using the diffusion theory. Figure 3.13 shows the process schedule based on the preceding considerations, and Table 3.1 shows the measured process parameters.

3.5 Experimental Results

The experiments may be subdivided into three main groups: electrical, optical qualitative and optical quantitative. The electrical measurements were made to determine BV and series resistance values. The optical qualitative consisted mainly in determining the physical location of light emission, i.e., to check if light was emitted from the depletion regions under avalanche breakdown. The optical quantitative consisted of measurements of power output as a function of current input and spectra. These last measurements allowed a comparison of values and data with those already reported in the literature, to obtain absolute values of light power output, and to look for the most efficient structure. Two types of results are discussed in a fourth section: those concerning the influence of the SiO_2 on light emission, and the results concerning the photodetection properties.

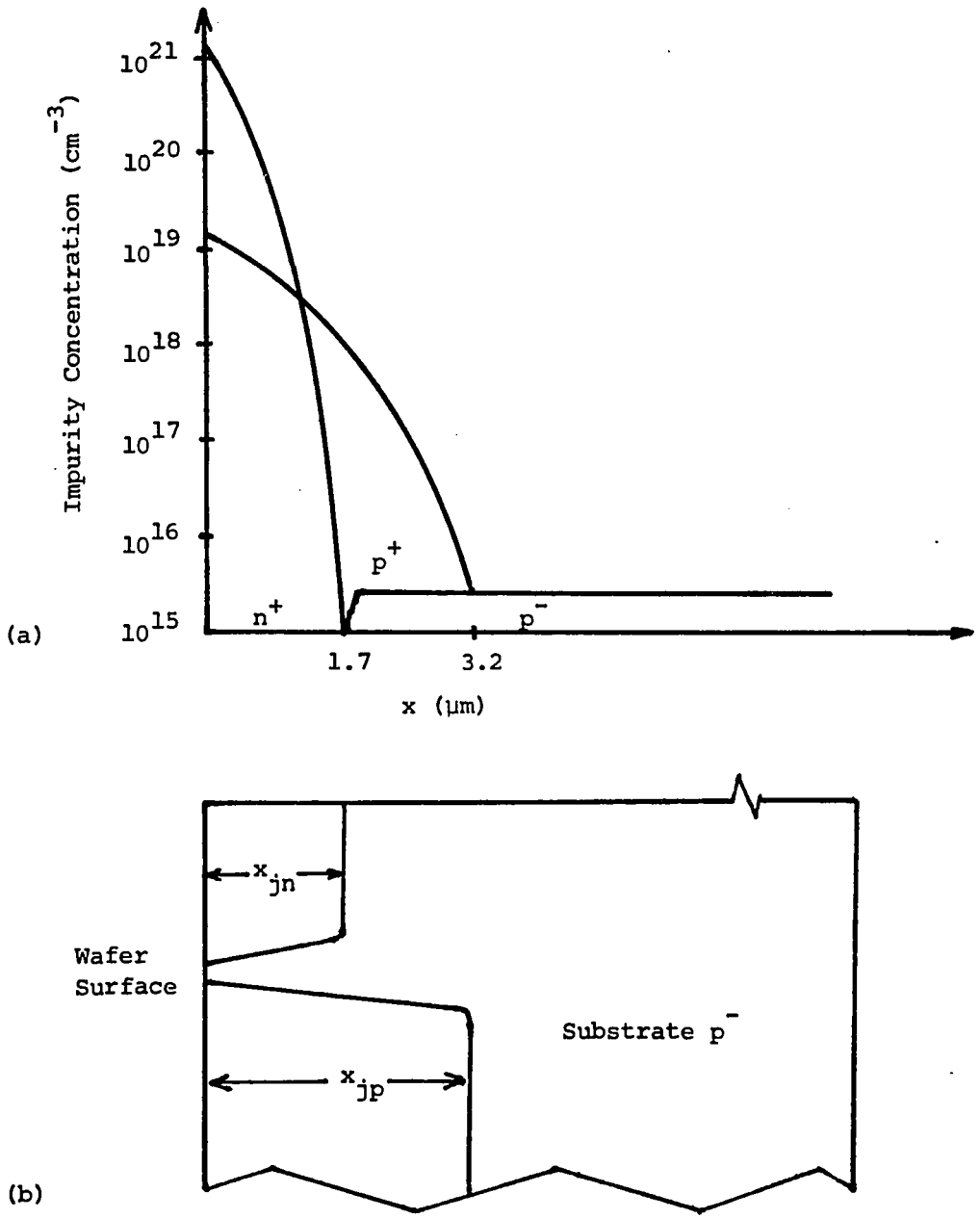

Fig. 3.11 Gap structure profile and cross section. -- (a) Impurity profile; and (b) Junction cross section.

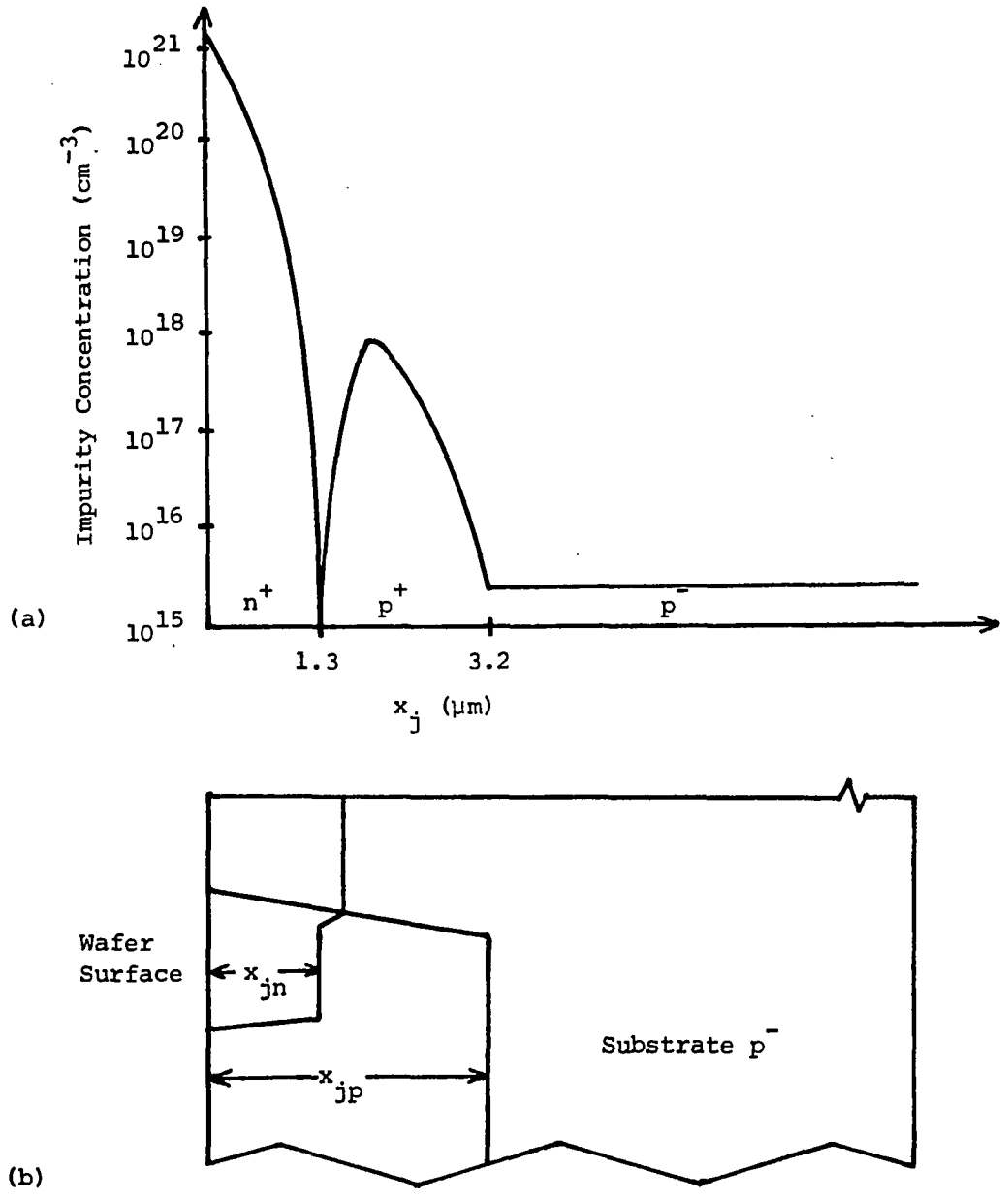

Fig. 3.12. Overlap structure profile and cross section. -- (a) Impurity profile; and (b) Junction cross section. Note that n^+ diffused over p^- gives a larger x_{jn}.

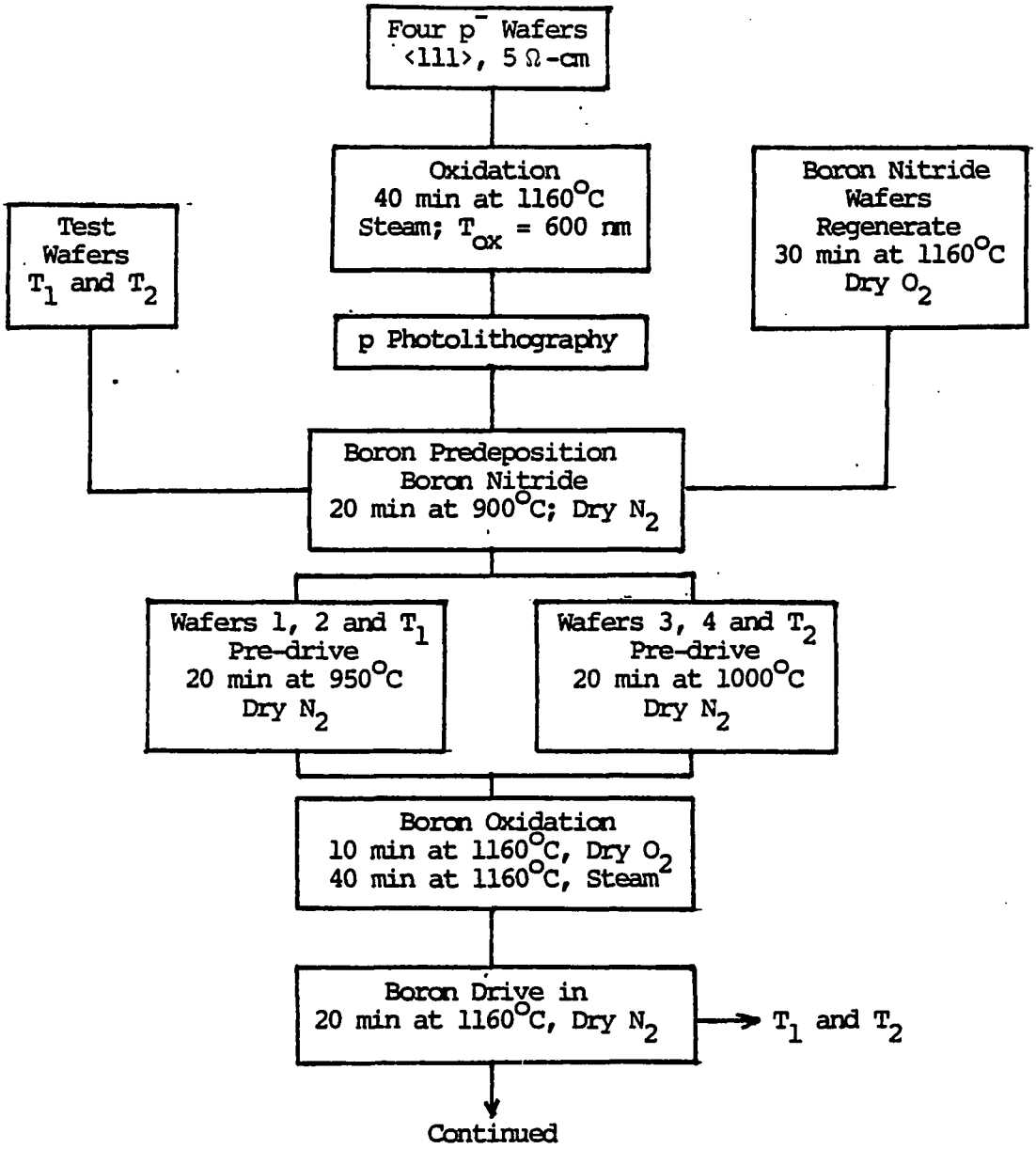

Fig. 3.13. Process flowchart--LED.

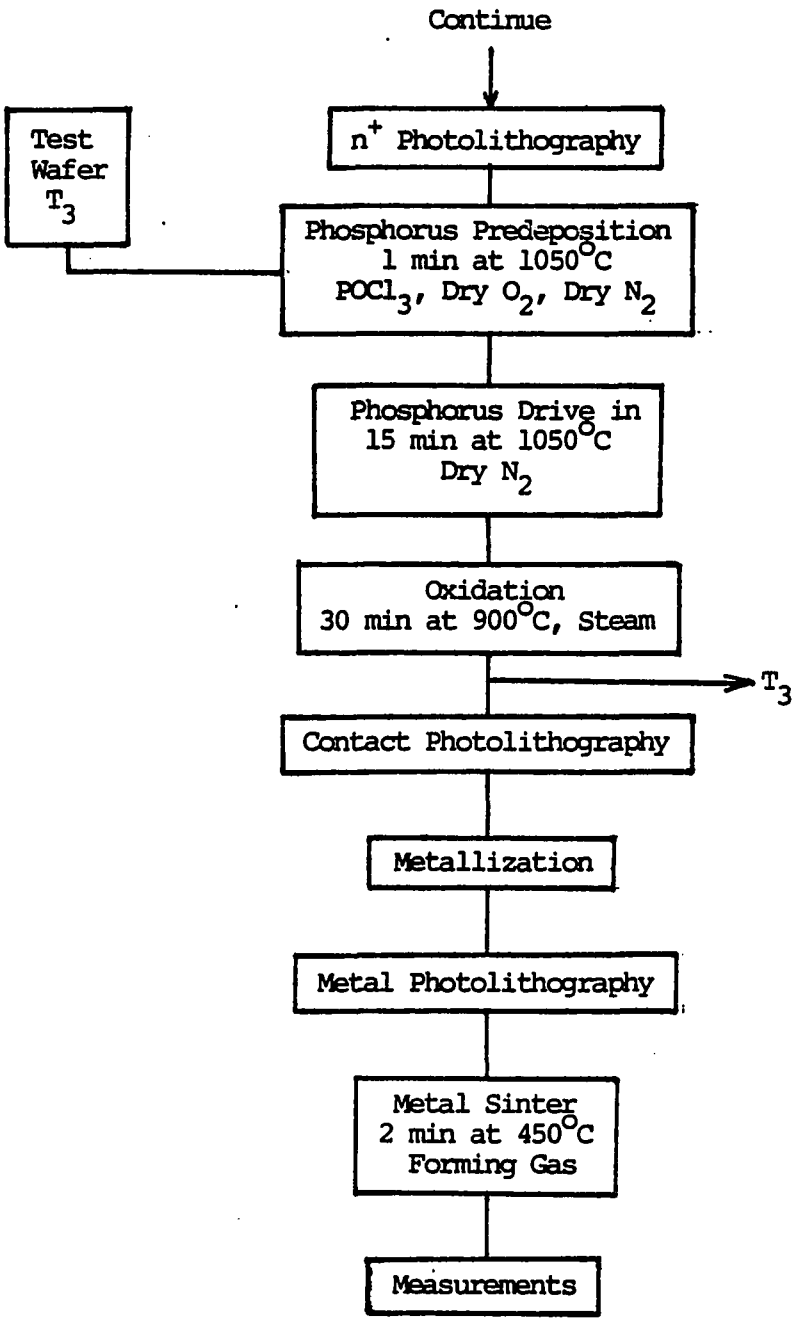

Figure 3.13--Continued

Table 3.1 Process parameters.

Starting material-p type, <111>	
Resistivity	5 Ω cm
Boron diffusion	
Sheet resistance (both pre-drives)	0.6 Ω/□
Calculated virtual junction depth	3.2 μm
Phosphorus diffusion	
Sheet resistance	4.6 Ω/□
Junction depth (over p^-)	1.5 μm

3.5.1 Electrical Results

Electrical measurements were made on all the devices of many dice, and on all the wafers. The BV is 5.9 $\pm$ 0.1 V for Wafers 1 and 2 (pre-drive at 950^{o}C) and 5.6 $\pm$ 0.1 V for Wafer 3 (pre-drive at 1000^{o}C) for the overlap structure, and 6.5 $\pm$ 0.1 V for the gap structure in all the wafers. The abutting structures gave one or another value depending on misalignments. The series resistances are of the order of 6 ohms in type O devices, to 25 ohms in devices in Row 9.

3.5.2 Optical Qualitative Results

The physical location of light emission was established, and in all the devices, light is generated at the border of the n^{+} region where avalanche breakdown is taking place. In devices in which the corners of the n^{+} pattern are clearly visible, e.g., 1-3, 2-3, 7-3, and 2-4, light emission occurs at the corners first, when avalanche breakdown is reached.

3.5.3 Optical Quantitative Results

Because of the lack of sensitivity in the instruments used, light emission data could only be taken in type O devices and from four dice in different wafers. Due to misalignments, type O devices with gap and overlap structures were available. Those dice were packaged by Mr. James A. Homoki, Lab Engineer at MEL. Some of these were

covered with a thin glass to protect the bonds. The following four type O devices, identified by the letters A, B, C, and D, were investigated:

A. Gap structure, from Wafer 1, with coverglass;

B. Overlap structure, from Wafer 3, no coverglass;

C. Gap structure, from Wafer 2, with coverglass;

D. Gap structure, from Wafer 3, no coverglass.

All four devices were used for power output measurements, and Device A was used for spectral measurements. Both types of measurements were made at the University of Arizona Quantum Electronics Laboratory under the supervision of Dr. Roger C. Jones, Director.

3.5.3.1 Power Output-efficiency. The power output as a function of input current was determined using an NRC Newport Research, Model 815 Power meter, Serial No. 624, set to the most sensitive scale, 2 μW full scale. The detector model is VPH-4, and was used without filter. This power meter works linearly between 4000 and 11000 Å. The basic set-up appears on Fig. 3.14. The light emitting device is connected to a power supply and ampere meter; a resistor of 50 ohms nominal value is used to limit the current. The LED is attached to a holder and positioned facing the sensitive surface of the detector. This surface is large enough to

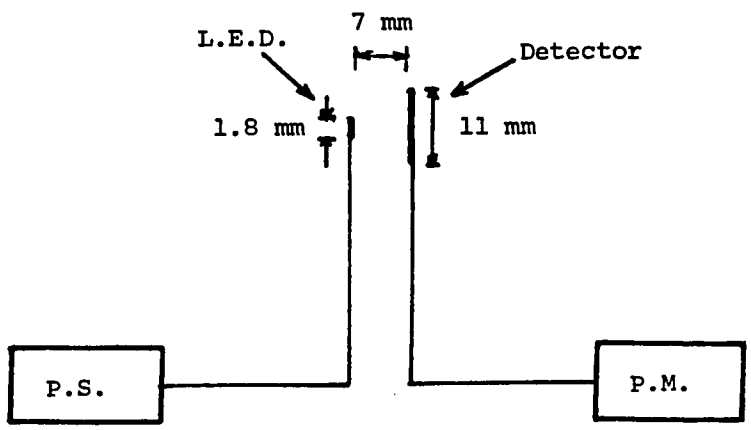

Fig. 3.14. Set-up for power measurements. -- The package containing a bonded die is put in close proximity to the detector and then both are covered with a black cloth. The sensitive surface is large enough to allow small misalignments between die and detector, and to pick up most of the light. P.S. = power source, P. M. = power meter.

allow small misalignments between die and detector, and to pick up most of the light.

Figure 3.15 shows the measured power output as a function of the input current for the four devices under consideration. The digital power meter gave only one or two significant figures. For the 2 μW range the digital power meter has a resolution of 0.02 μW. The behavior of the devices is evidently linear:

$$W_{out} = \alpha.I \qquad (3.1)$$

where α is of the order of 4 μW/A. Device B shows half the power output of Device D. Both devices are from the same wafer, but D is the gap type, while B is the overlap type.

In Fig. 3.16 the same data of power output are plotted as a function of the power input to the device. Power input is defined as V.I, where V is the measured voltage drop across the device and I the current through the device or, in other words, the power input is $BV.I + I^2.R_s$ where R_s is the series resistance of the device, about 6 ohms, and not the limiting resistor, about 50 ohms, of the circuit, and BV is the breakdown voltage. The sublinear dependence is evident due to the $I^2.R_s$ term.

Figure 3.17 shows the efficiency as a function of the current through the device. Efficiency is defined as light power output divided by electric power input, that is:

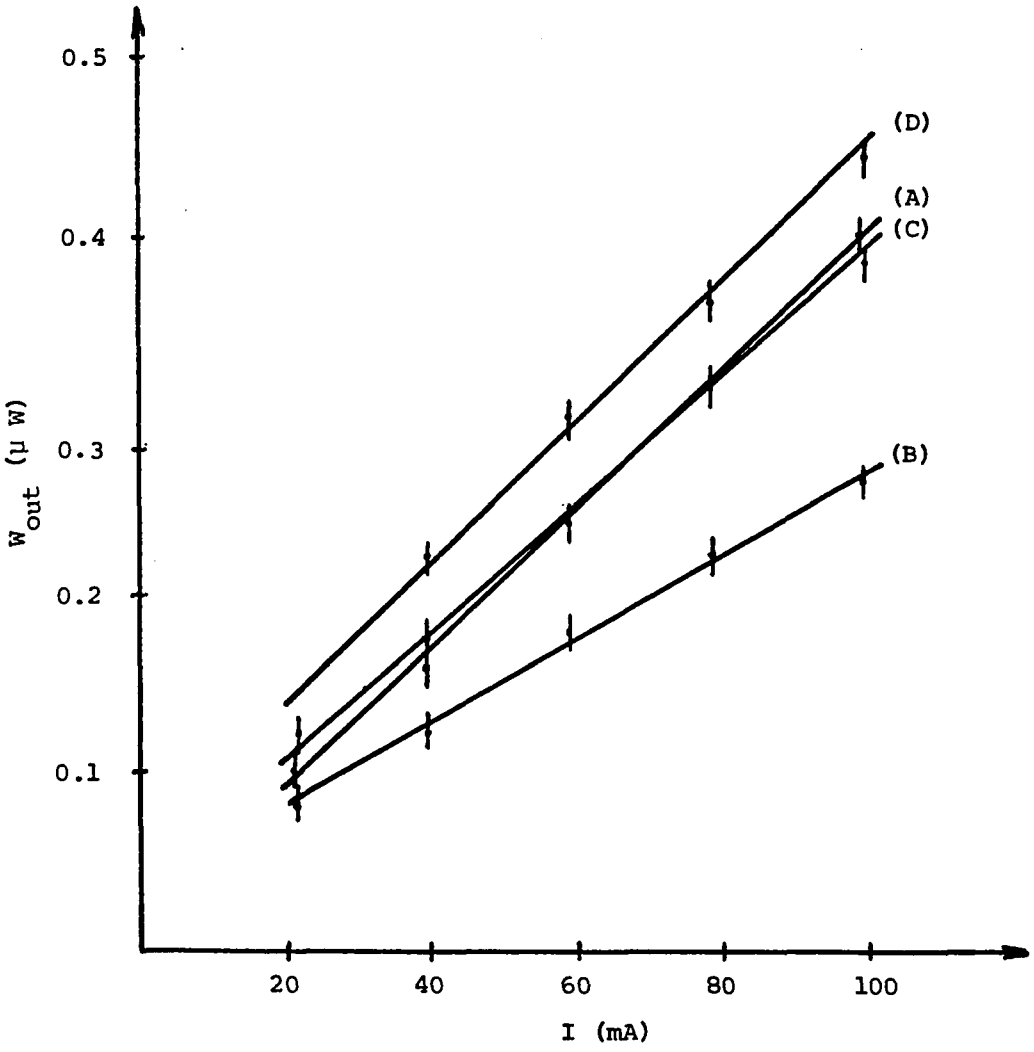

Fig. 3.15. Measured power output as a function of current input. -- Description of the devices: (A) Gap structure, from Wafer 1, with coverglass; (B) Overlap structure, from Wafer 3, no coverglass; (C) Gap structure, from Wafer 2, with coverglass; and (D) Gap structure, from Wafer 3, no coverglass. Note the linearity of W_{out} with I_{in}.

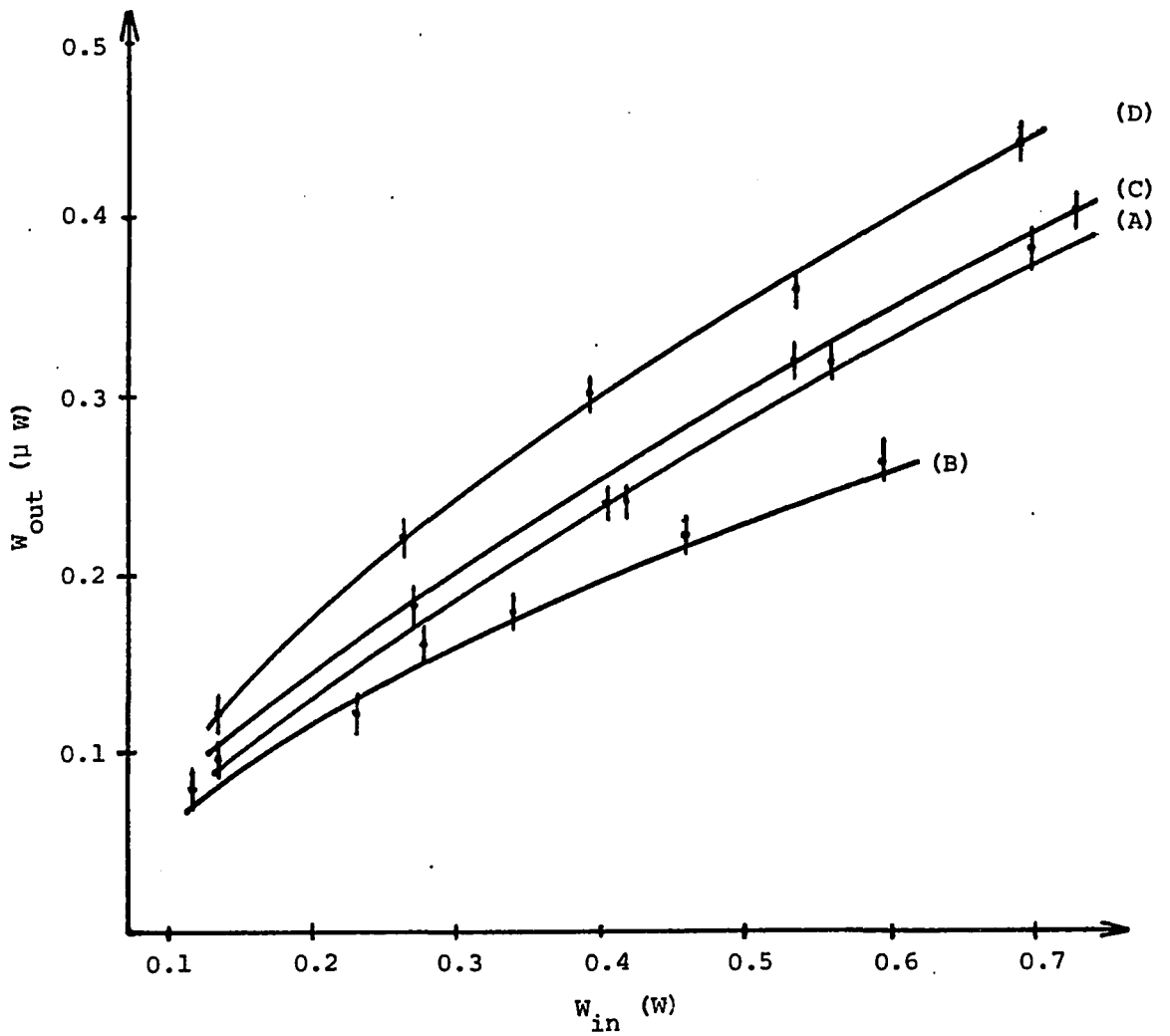

Fig. 3.16. Power (light) output as a function of power input. -- Power input is defined as V.I or BV.I + $I^2.R_s$ where V is the voltage drop across the diode, BV the breakdown voltage and R_s the series resistance of the device. (A), (B), (C) and (D) are the four devices O described in Fig. 3.15.

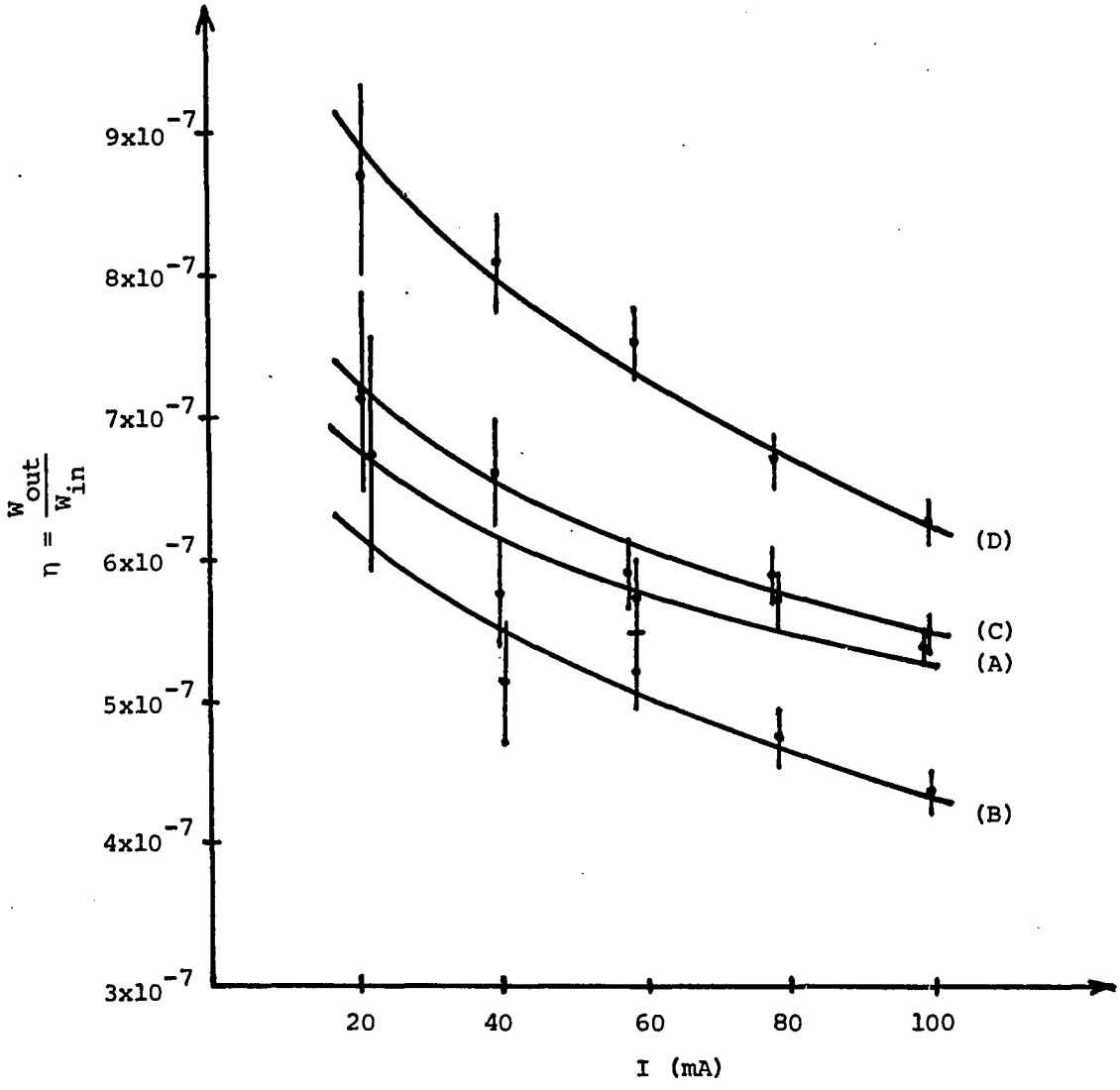

Fig. 3.17. Efficiency as a function of current input. -- Efficiency is defined as measured power (light) output divided by power input V.I, where V is the voltage drop across the device. (A), (B), (C) and (D) are the four devices O described in Fig. 3.15. Note the hyperbolic dependence of the efficiency on the current input.

$$\eta = \frac{W_{out}}{W_{in}} = \frac{\alpha.I}{BV.I + I^2.R_s} = \frac{\alpha}{BV + I.R_s} \qquad (3.2)$$

Thus, the hyperbolic behavior is reasonable. Numerically,

$$\eta = 6 \times 10^{-7}$$

at 100 mA. For low currents, a "junction efficiency":

$$\eta' = \frac{\alpha.I}{BV.I} = \frac{\alpha}{BV} \qquad (3.3)$$

may be defined; in this study values of η' are between 7×10^{-7} and 10^{-6}. Error bars are different for each power input:

$$\pm \Delta\eta = \pm \frac{\Delta W_{out}}{W_{in}} \qquad (3.4)$$

assuming the measure on W_{in} without errors. Thus, $\Delta\eta$ decreases for larger W_{in}.

Figure 3.18 shows the efficiency as a function of power input; both quantities were defined previously. Error bars are equal to the ones in Fig. 3.17.

3.5.3.2 Spectral Response. The emission spectrum for Device A, that is, gap structure, from Wafer 1 with coverglass, was determined using a Jarrell-Ash 0.5 meter Ebert-type scanning monochromator, Model No. 82020, Serial No. 859765. The grating has 1180 grooves/mm, with a resolution of at least 0.2 Å at first order which spans from

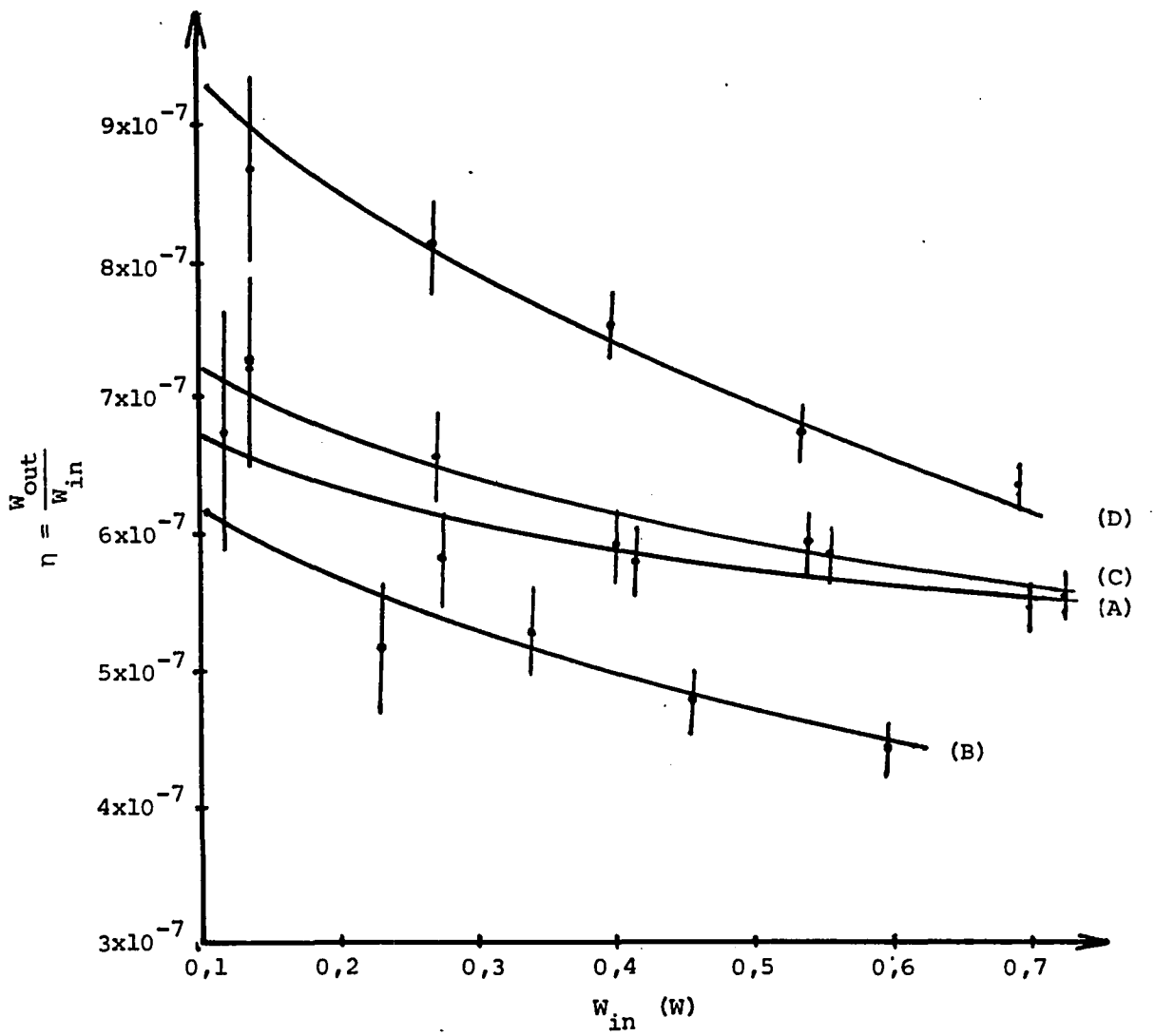

Fig. 3.18. Efficiency as a function of power input. -- Efficiency is defined as measured power output divided by power input V.I, where V is the voltage drop across the device. (A), (B), (C) and (D) are the four devices O described in Fig. 3.15.

1900 to 9100 Å, and is blazed at 5000 Å. A photomultiplier, Fairchild-Dumont 6291, spectral response S-11, is connected at the exit slit. Figure 3.19 shows a diagram of the monochromator and general setup. The LED is positioned at the entrance slit, and the photomultiplier is positioned at the exit slit. In order to scan a wavelength range, a motor rotates the grating, projecting a different region of the spectrum of the radiation to the exit slit for each angle of rotation. A scale outside the monochromator shows the wavelength detected, i.e., the wavelength component that is at the exit slit. The photomultiplier has a photosensitive surface known as the photocathode which emits electrons when radiation is incident on it. This element has a spectral response with wavelength which will be described later. The photocathode current is amplified in the photomultiplier and in an electronic amplifier. The amplified signal is recorded on paper using a plotter. The system drifts, and while the system is ON, the recorded signal increases with time even without the presence of any input signal. Thus, it was necessary to determine the drift for correcting the spectrum. For this reason the following six runs between 4000 and 7000 Å were scanned:

1. LED ON; scanning from 4000 Å up to 7000 Å,
2. LED ON: scanning from 7000 Å down to 4000 Å,

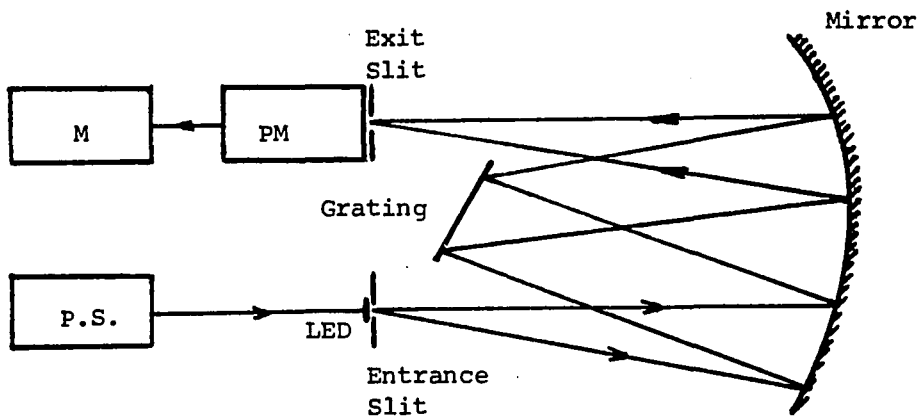

Fig. 3.19. Ebert type grating monochromator and general set-up for measurement (after Martin, 1967). -- The light from the light emitting device (LED) is reflected at the mirror and diffracted at the grating. The mirror focuses and collimates the light rays. The exit slit lets the light within a certain wavelength interval pass and reach the photomultiplier, where it is detected and the signal amplified.

3. LED OFF; scanning from 4000 Å up to 7000 Å,
4. LED OFF; scanning from 7000 Å down to 4000 Å.

These last two runs establish the drift of the system. In principle, they should allow a correction of the first two spectra. Two additional, and reliable, measurements were made:

5. LED ON; scanning from 4000 Å up to 7000 Å. LED turned OFF every 250 Å to adjust the "zero" of the system. Thus, a "true" value of light emission was available every 250 Å, without the influence of the drift.
6. LED ON; scanning from 7000 Å down to 4000 Å. LED turned OFF every 250 Å to adjust the "zero" of the system. Same consideration as in Run 5 applied here.

No signal could be detected below 4000 Å and above 7000 Å. The current through the LED was maintained at 160 mA dc.

The six resulting curves are shown in Fig. 3.20. The Traces 5 and 6 are considered reliable spectra, and differences are mainly assigned to the wrong correction of zero. Spectrum 1 was corrected for the drift using 3, and spectrum 2 using 4. As shown in Fig. 3.21, both corrected spectra 1' and 2' turned out to be too different from 5

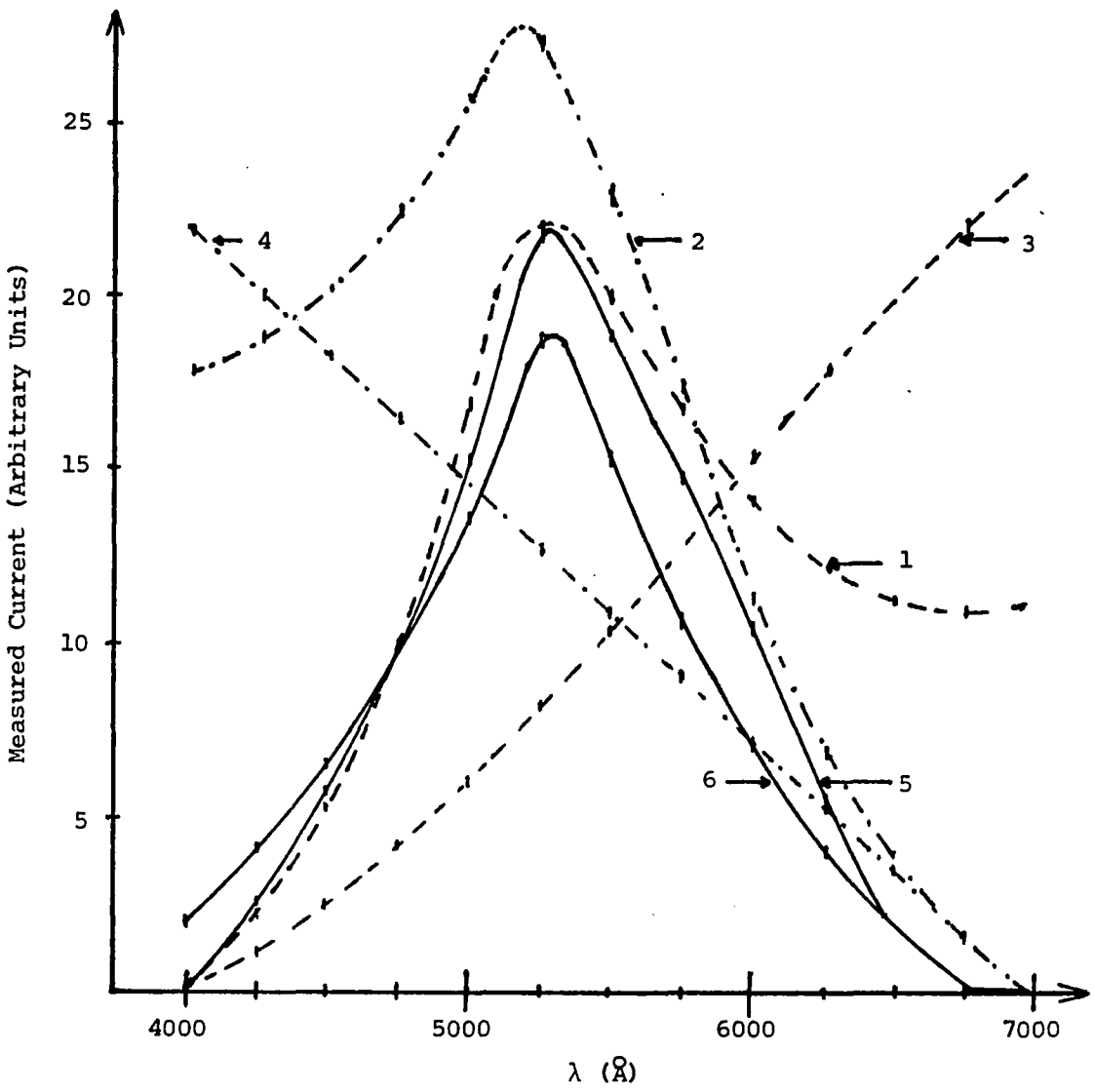

Fig. 3.20. Emitted spectra before corrections. -- Spectra determined for the type O device identified as (A), under a current of 160 mA dc. Description of measurements:
(1) LED ON; scanning from 4000 Å up to 7000 Å.
(2) LED ON; scanning from 7000 Å down to 4000 Å.
(3) LED OFF; scanning from 4000 Å up to 7000 Å.
(4) LED OFF; scanning from 7000 Å down to 4000 Å.
(5) LED ON; scanning from 4000 Å up to 7000 Å.
(6) LED ON; scanning from 7000 Å down to 4000 Å.
In measurements (5) and (6) the LED is turned OFF every 250 A to adjust the zero of the meter.

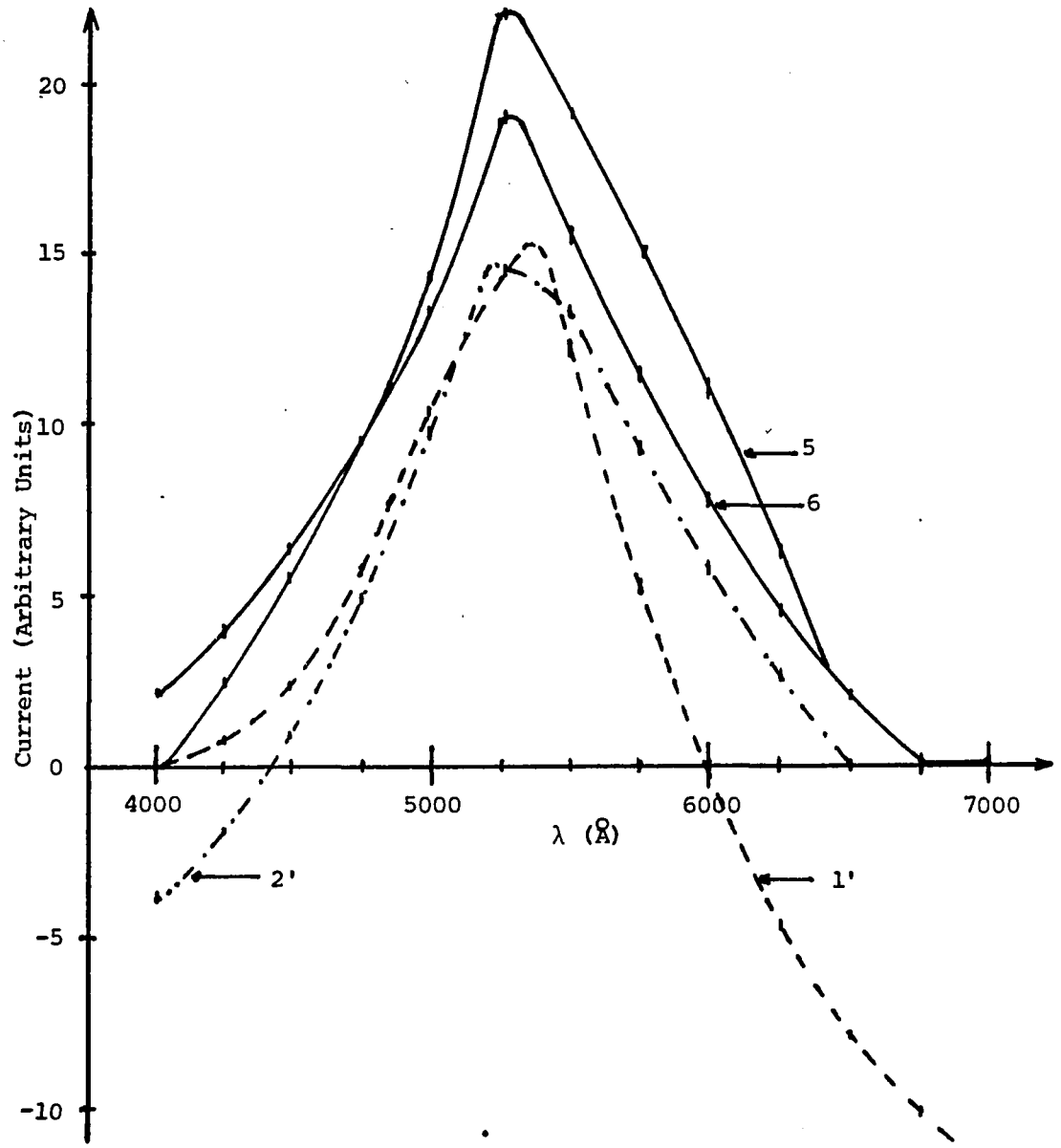

Fig. 3.21. Spectra corrected for drift. -- Using the preceding Fig. 3.20, curve (1') is obtained as (1) - (3), and curve (2') is obtained as (2) - (4). Curves (5) and (6) are the same as before. Corrected curves give unreliable values (negative) and so cannot be taken into account.

and 6, giving also negative values in parts of their characteristics. This was attributed to the random value of the drift. Hence, it was decided not to take into account those two "corrected" spectra 1' and 2'.

Figure 3.22 shows the average spectrum considering only measurements 5 and 6, before corrections for the photomultiplier and grating responses are made. The error bars indicate the differences between the two traces considered.

The photomultiplier has a spectral response, i.e., the photocathode current varies with the wavelength of the incident light. Figure 3.23 shows the relative spectral sensitivity characteristic of the photocathode used in these measurements, S-11 response type, for constant light intensity at the photocathode. The maximum sensitivity is 56 mA/W at 4400 Å. These data were given by Dr. Hans Roehrig, from the UA Optical Sciences Center.

Thus, the absolute sensitivity was immediately calculated for each wavelength, as the relative sensitivity times 56 mA/W. Then the quantum efficiency of the detector, that is, the number of electrons emitted for each incident photon, for each wavelength, was calculated using the following equation (Engstrom, 1980):

$$\eta_{Det}\ (\%) = 124.\ \frac{\sigma(mA/W)}{\lambda(nm)} \qquad (3.5)$$

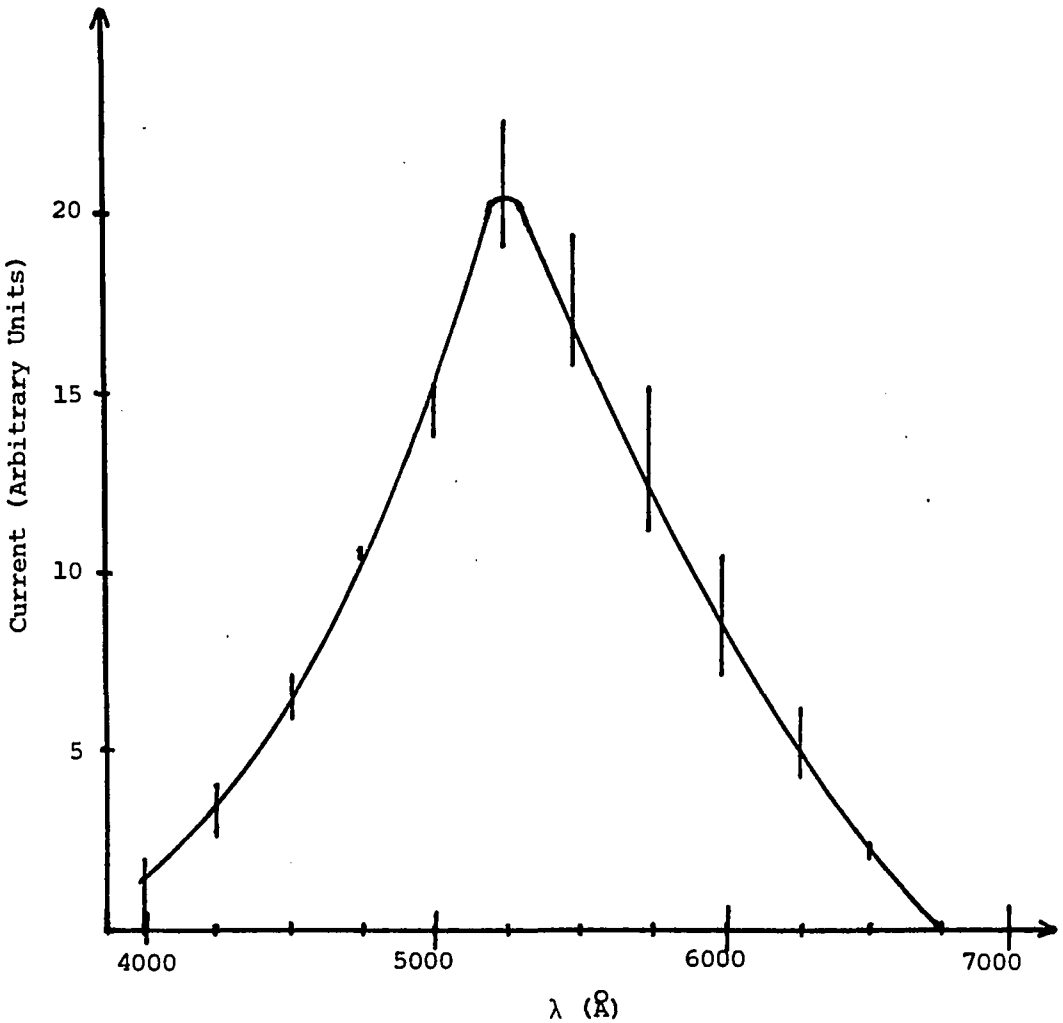

Fig. 3.22. Average spectrum before corrections for the photomultiplier and grating responses. -- Determined using measurements (5) and (6) from the preceding figures. Error bars extend between both measurements.

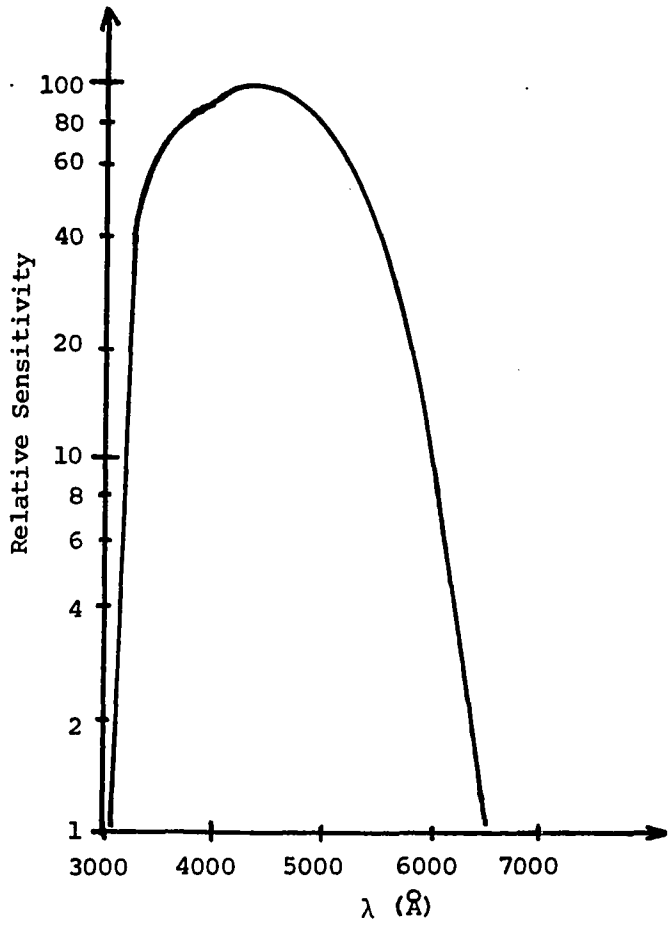

Fig. 3.23. Spectral-sensitivity characteristic of photosensitive device having S-11 response. -- Determined for equal values of Radiant Power at all wavelengths. This is the response of the photocathode of the photomultiplier and will be used for determining the number of photons reaching the photocathode, knowing the generated and measured current (Fig. 3.22). Plot after RCA Electron Tube Handbook (1972).

where σ is the absolute sensitivity at each wavelength λ. Then, for each λ,

$$(\text{Number of photons}) \times \frac{\eta_{Det}}{100} \alpha I_{PM} \tag{3.6}$$

where

$$I_{PM} \equiv I_{photomultiplier}$$

Thus,

$$(\text{Number of photons}) \alpha \frac{I_{PM}}{\eta_{Det}} \times 100 \tag{3.7}$$

I_{PM}, the current from the photomultiplier, is proportional to the recorded one. No calibration was done, so only relative values were obtained. Figure 3.24 shows the spectral distribution corrected for the photomultiplier response.

Another correction was necessary. Grating efficiency is defined as the fraction of the incident power at each wavelength diffracted into the order in question. The grating is said to be "blazed" for a wavelength λ_b at the peak of the first order efficiency curve. For wavelengths near λ_b most of the incident power falls into the first order and very little falls into the second and higher orders. Figure 3.25 shows the grating efficiencies for different orders. In this particular experiment the used grating was blazed for 5000 Å. Thus:

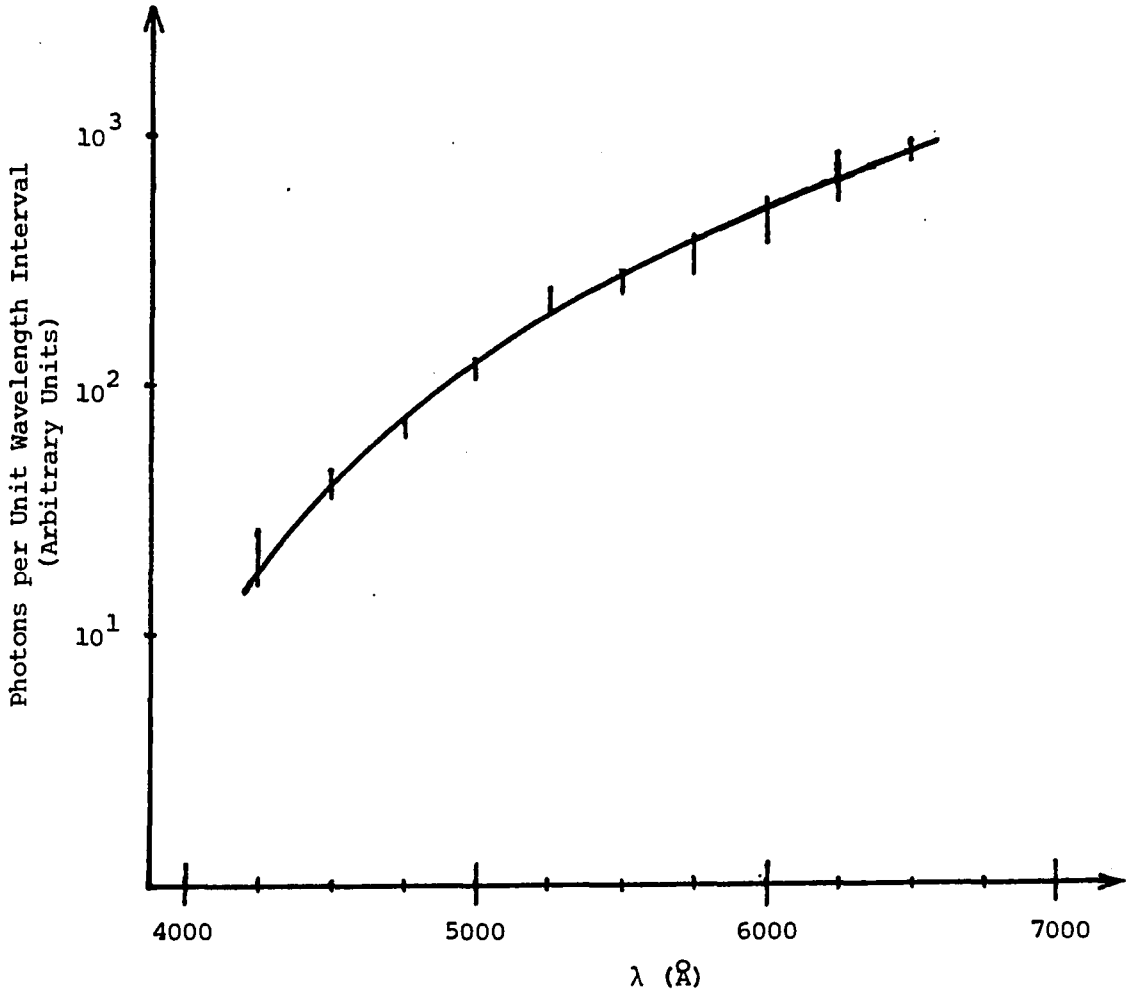

Fig. 3.24. Spectral distribution corrected for the photomultiplier response. -- This spectrum gives the relative number of photons per unit wavelength interval.

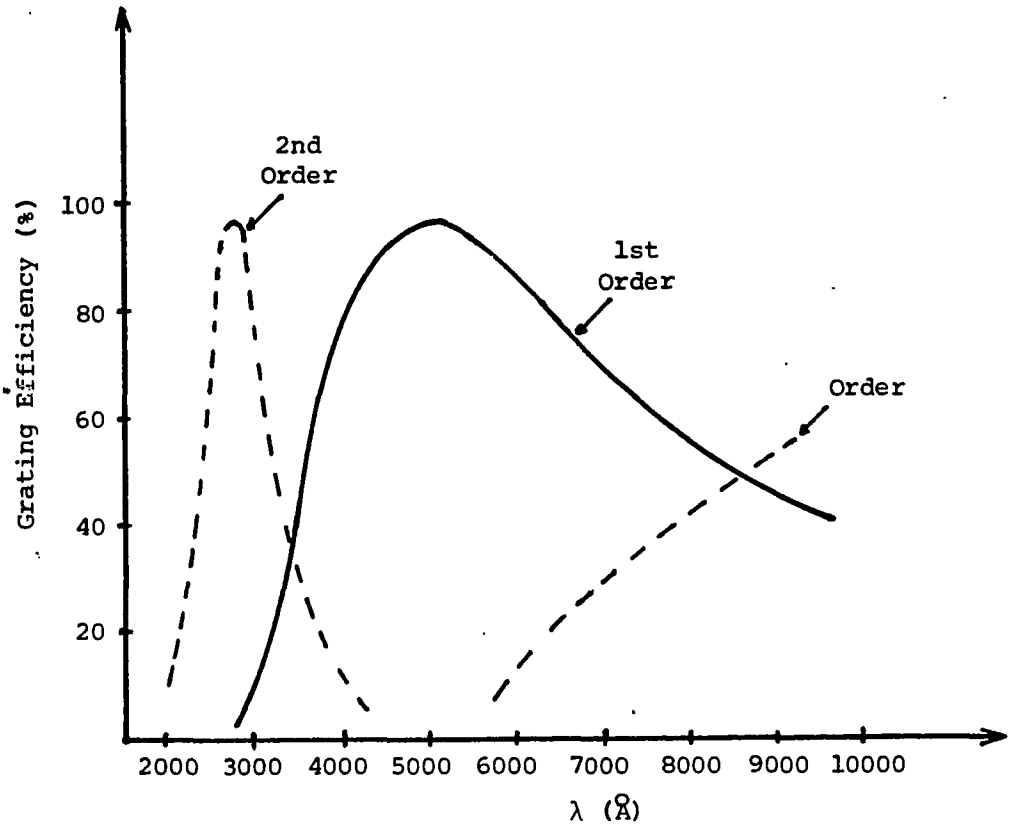

Fig. 3.25. Efficiencies of a grating (after Martin, 1967). -- Grating efficiency is defined as the fraction of the incident power at each wavelength diffracted into the order in question. The grating is said to be "blazed" for the wavelength λ_b (5000 A in this case) at the peak of the first order efficiency curve. For wavelengths near λ_b most of the incident power falls into the first order.

$$(\text{No. photons})_{\text{real}} = \frac{(\text{No. photons})_{\text{old value}}}{\eta_{\text{grating (\%)}}} \times 100 \qquad (3.8)$$

The corrected spectrum is shown in Fig. 3.26. This spectrum gives the number of photons emitted per wavelength interval, in relative units. A monotonic increase of the number of photons per unit wavelength interval with wavelength is noticed.

In order to find the emission spectrum per photon energy interval as a function of the photon energy, it is necessary to transform the wavelength interval $\Delta\lambda$ to a photon energy interval ΔE. For an interval $\Delta\lambda$ and an interval ΔE, the area under both spectral curves, i.e., the number N of photons, must be the same. Thus:

$$N_\lambda \times \Delta\lambda = N_E \times \Delta E = N_E \times h.\Delta\nu \qquad (3.9)$$

So,

$$N_E = \frac{N_\lambda}{h} \times \frac{\Delta\lambda}{\Delta\nu} \qquad (3.10)$$

But:

$$\lambda = \frac{c}{\nu} \qquad (3.11)$$

Therefore,

$$|\Delta\lambda| = \frac{c}{\nu^2} .\Delta\nu \qquad (3.12)$$

or

$$\left|\frac{\Delta\lambda}{\Delta\nu}\right| = \frac{c}{\nu^2} \qquad (3.13)$$

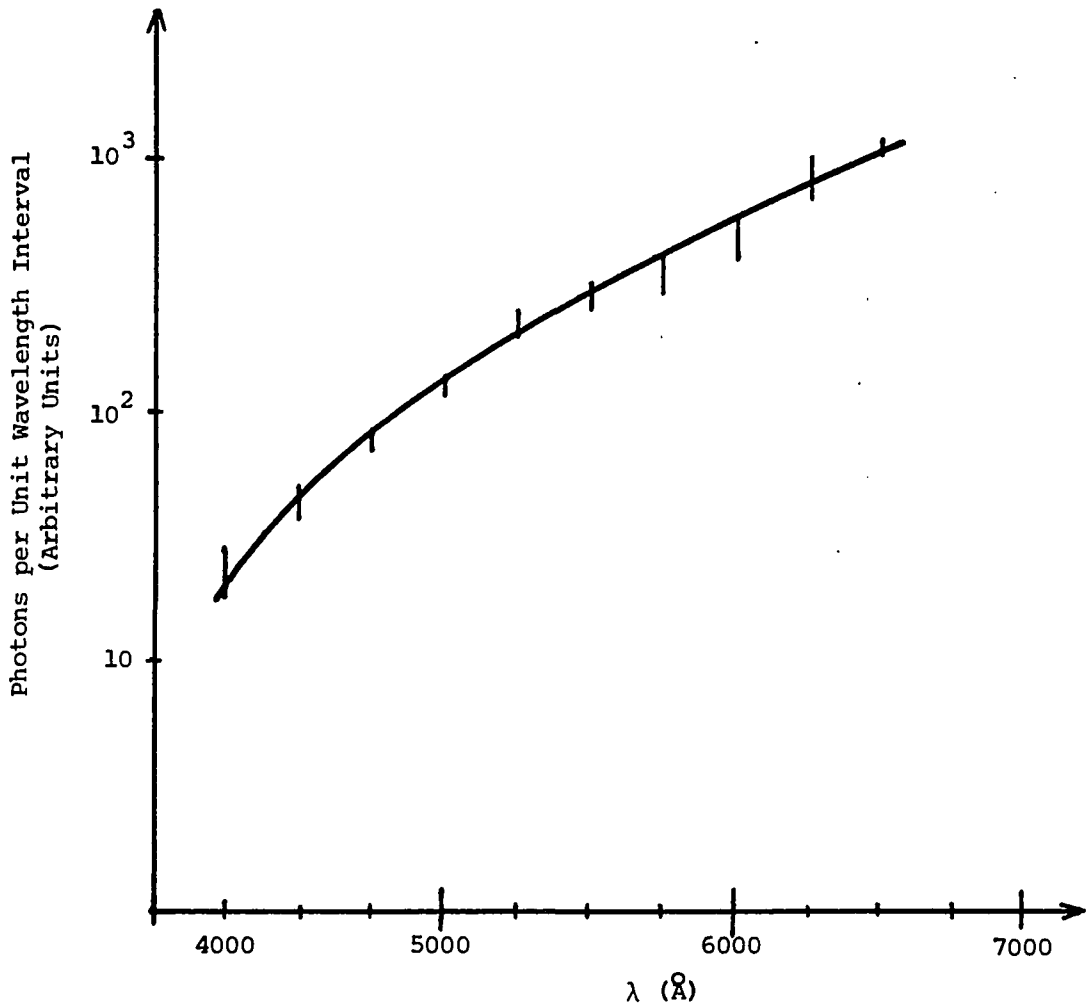

Fig. 3.26. Spectral distribution corrected for the photomultiplier and grating responses.

where ν is the frequency of the electromagnetic wave of wavelength λ and c is the velocity of light. Hence:

$$N_E = \frac{N_\lambda}{h} \cdot \frac{c}{\nu^2} = N_\lambda \cdot \frac{hc}{(h\nu)^2} = N_\lambda \cdot \frac{hc}{(\hbar\omega)^2} \qquad (3.14)$$

Thus,

$$N_E \alpha \frac{N_\lambda}{(\hbar\omega)^2} \qquad (3.15)$$

with $\hbar w$ the photon energy in the considered energy interval. Using Eq. 3.15, the spectral distribution per photon energy interval as a function of the photon energy was obtained. The result is shown in Fig. 3.27. Notice the monotonic decrease in the number of photons for increasing photon energies.

As was explained in Section 2.2.3, the spectrum of Fig. 3.27 represents the quantum efficiency of the light emitting device at the considered photon energy. That is,

$$N_E = \frac{J_{out}}{\hbar\omega} \qquad (3.16)$$

where J_{out} represents the power emitted per unit energy interval. Figure 3.28 shows the power J_{out} spectrum as a function of the photon energy. Notice the monotonic decrease for increasing photon energies in the considered photon energy range.

3.5.3.3 Quantum Efficiency. The absolute value of the quantum efficiency of the light emitting device, which

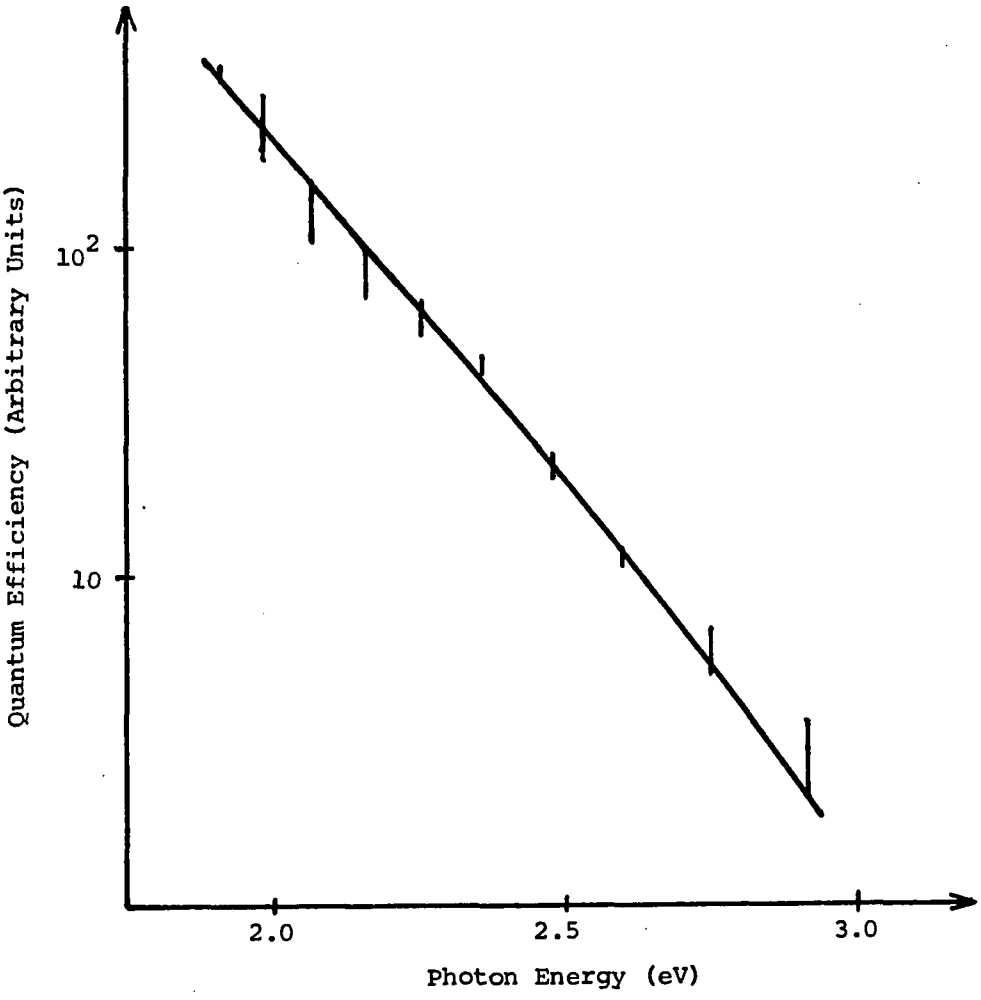

Fig. 3.27. Corrected spectral distribution as a function of the photon energy. -- The number of photons per unit energy interval is proportional to the number of photons per unit wavelength interval (Fig. 3.26) divided by the photon energy squared. This plot agrees completely with the already published spectra, also known in the literature as the "spectral distribution of the quantum efficiency." This quantum efficiency is proportional to the number of photons in each photon energy interval.

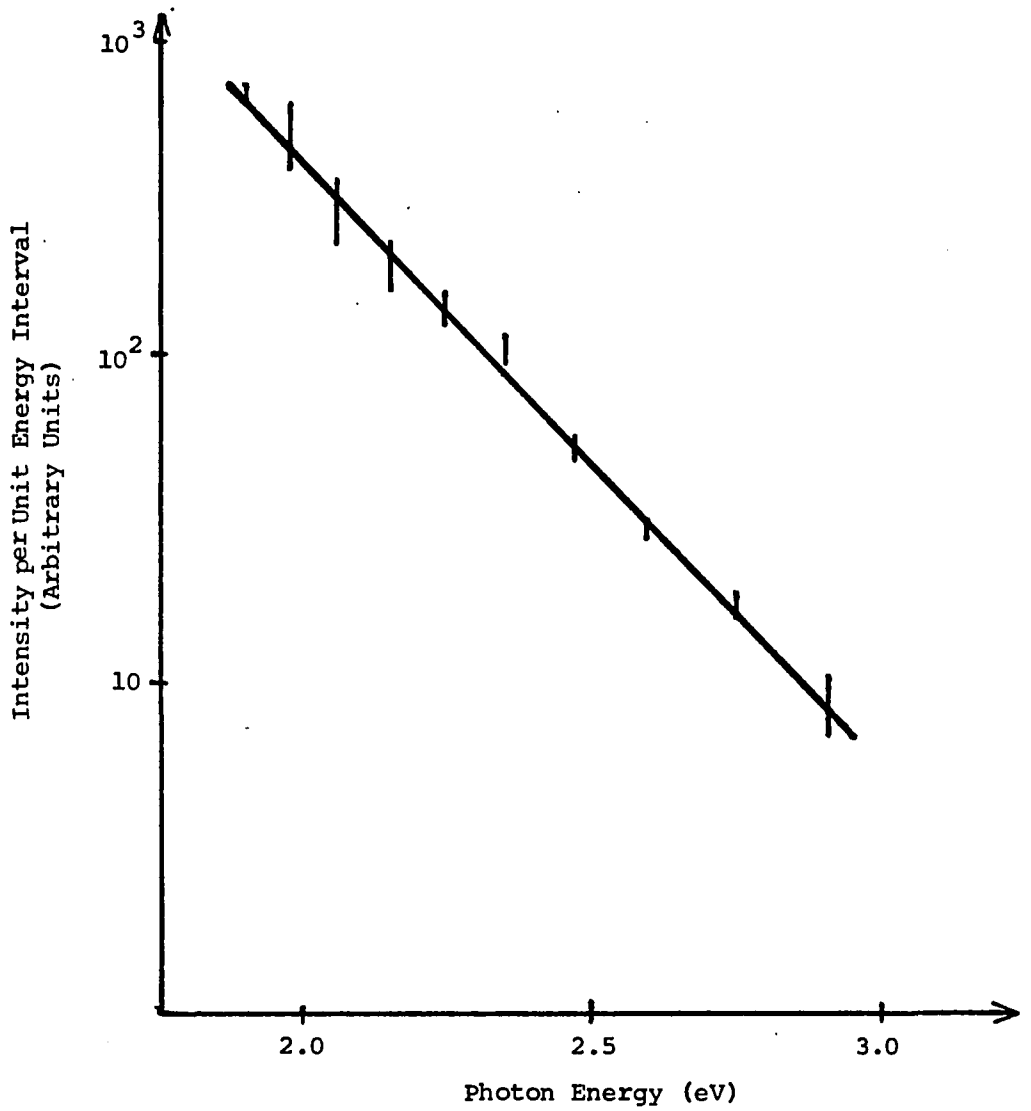

Fig. 3.28. Spectral distribution of intensities (radiated power). -- The power radiated per photon energy interval is obtained multiplying the number of photons per unit energy interval (Fig. 3.27) by the photon energy.

is the total number of photons emitted per electron that forms part of the current density that flows through the device, can be estimated. The determined spectrum, Fig. 3.27, increases for decreasing photon energies. Thus, it seems reasonable to expect an average photon energy lying in the infrared. An integration over the whole spectrum would be the best solution to find an average value of photon energy, but the scanned region was too small and, based on previous publications, noted in Section 2.2.3, large amounts of photons with energies smaller than 2 eV might be present. For the purpose of estimating an order of magnitude of the absolute quantum efficiency, an average photon energy of 1.5 eV was assumed. This result will give the number of photons in an energy range of the order of 1 eV to 3 eV, the detection range of the power meter, emitted per electron. This region of the spectrum is the most important for the present study concerning light emission. For a current density of 100 mA the total power output is 0.4 μW (Fig. 3.15). Thus:

$$\frac{\text{Power}}{I} = \frac{0.4\ \mu W}{100\ mA} = 4 \times 10^{-6}\ \frac{W}{A}$$

But

$$\frac{[W]}{[A]} = \frac{J/s}{C/s} = \frac{J}{C} = q^{-1} \cdot \frac{eV}{C} = q^{-1} \cdot \frac{eV/photon}{C/photon} =$$

$$\frac{q^{-1}}{\hbar\omega} \cdot \frac{photon}{C} = \frac{q^{-1}}{\hbar\omega} \cdot \frac{photon/e^-}{C/e^-}$$

$$= \frac{q^{-1}}{\hbar\omega . q^{-1}} \text{ photons/e}^-$$

where

$$q = 1.6 \times 10^{-19}$$

and

$$\hbar\omega = 1.5$$

Hence,

$$\frac{\text{Power}}{I} = \frac{4 \times 10^{-6}}{1.5} \text{ photons/e}^- = 2.6 \times 10^{-6} \text{ photons/e}^-.$$

So, the quantum efficiency was estimated on the order of 3 x 10^{-6} photons/electron.

3.5.4 Other Optical Results

Two additional qualitative results are presented. In order to determine the influence of the thermally grown oxide on the power output and spectral characteristics of the emission, the oxide was stripped from half of a wafer. No difference was noticed between the light outputs from both sides, while testing many types of O devices, with overlap and gap structures from many dice and on two wafers. No quantification was possible because of the lack of resources at the moment.

Devices were tested as photodetectors. Detection took place whenever the junction was exposed, i.e., not covered with aluminum. The avalanche photoeffect, i.e., the reverse biasing of the diode exactly to the beginning of avalanche in which the absorption of light gives generation

and multiplication of carriers and so a much higher current, was not noticed in the gap structures. No quantification of sensitivities was done, because that is beyond the scope of this study.

3.6 Discussion of Experimental Results

The breakdown voltage in Wafers 1 and 2 was 5.9 $\pm$ 0.1 V for all devices except for the devices with the gap structure, where it was higher, 6.5 $\pm$ 0.1 V. Wafer 3, which was given a higher pre-drive temperature, had a lower breakdown voltage, 5.6 $\pm$ 0.1 V, in the p-n type devices, although they are the same in the gap structures; when punch-through takes place, the diodes enter into the avalanche region at basically the same voltage. Values of BV obtained are of the expected and desired order of magnitude. Measured values of series resistances are on the order of 6 ohms for type O devices to 25 ohms for devices in row 9 (Fig. 3.1).

Light emission from diffused p-n junctions takes place under avalanche breakdown, in agreement with the theory. In addition, when the voltage is increased, the first light appears at the most curved regions, or corners, of the junction, when avalanche breakdown is reached. This is explained by the presence of a higher electric field at the corners, which is why breakdown occurs at the corners first.

The power output increases proportionally to the current density (Fig. 3.15), with a coefficient of the order of 4×10^{-6} W/A for type O devices with gap structure. As a consequence, the efficiency decreases for larger currents and power inputs due to the I^2R_s power dissipation in the series resistance. From 20 mA to 100 mA of current input, the efficiency decreased about 25% depending on the sample characteristics (Fig. 3.17). Measured values of power output and efficiency are of the order of 0.4 μW and 6×10^{-7}, respectively, for a power input of 0.7 W (100 mA). The quantum efficiency was estimated as 3×10^{-6} photons/e^- assuming an average photon energy of 1.5 eV and the detection of all the emitted light. That value of quantum efficiency is one-third of that reported in the literature (Kosyachenko et al., 1984). However, it is not known which photon energy the authors considered for their estimate. A lower light output and efficiency was found in Sample B, with the overlap structure; see Figs. 3.15 to 3.18.

A lower coupling efficiency was not considered to be the cause because the measurement process was very carefully done. Gap structures have a larger depletion region width than overlap structures. Furthermore, qualitatively the observed light emitted line from the gap structure was much broader than that from the overlap structure. Thus, light was also generated at the p regions, which have much lower

concentrations. This result is somewhat contrary to Figielsky-Torun's model, according to which light is more likely to come from the n^+ region, reinforcing the theory of scattering by acoustic phonons (Kosyachenko et al., 1984). The slightly higher power output of Sample D is attributed to the lack of a protective coverglass, which reflects and absorbs part of the radiated energy; reflection alone gives a decrease in power transmitted through the coverglass of the order of 10%.

Spectral measurements agree completely with the spectra obtained by other investigators (see Section 2.2.3). The quantum efficiency per unit photon energy interval decreases monotonically for increasing photon energies (Fig. 3.27). Also, from 2 eV to 3 eV the quantum efficiency decreases by more than two orders of magnitude, in agreement with previous investigations, as they were described in Section 2.2.3, Figs. 2.9 and 2.13a. The small change in slope when approaching 2.4 eV is attributed to correction deficiencies due to the lack of larger correction curves and to fabrication tolerances. Measurements below 1.91 eV, i.e., wavelengths higher than 6500 Å, are not considered reliable because of the low sensitivity of the detector. The same holds true for measurements beyond 3.1 eV, i.e., wavelengths smaller than 4000 Å. The power spectrum

(Fig. 3.28) did not show any peak but decreases monotonically with increasing photon energies. This result does not necessarily contradict former studies, which find that a peak lies close to the energy band gap E_g, 1.1 eV for silicon (Haecker, 1974; Kosyachenko et al., 1984) because no measurement was possible in that photon energy region.

CHAPTER 4

CONSIDERATIONS ON OPTICAL INTERCONNECTIONS

4.1 Introduction

In this chapter a method for forming an optical interconnection is proposed. Two key points are considered in detail: substrate preparation, and waveguide etching. An optical interconnection was fabricated and tested. Only partial results, related to waveguide etching, were obtained. It was beyond the scope of this study to continue experiments on the subject. However, it was decided to include this discussion as a reference for future investigations.

4.2 Layout

The system to be designed consisted of a light emitting device (LED), a photodetector, and a waveguide adequately coupled to them, as described in Sections 2.4.3 and 3.3. Different LEDs and detectors were laid out as shown in Fig. 4.1. The waveguides were laid out in one direction. As discussed in Section 3.5.4, LEDs work as photodetectors.

In this study three different structures, gap, overlap, and abutting, as defined in Section 3.3 were

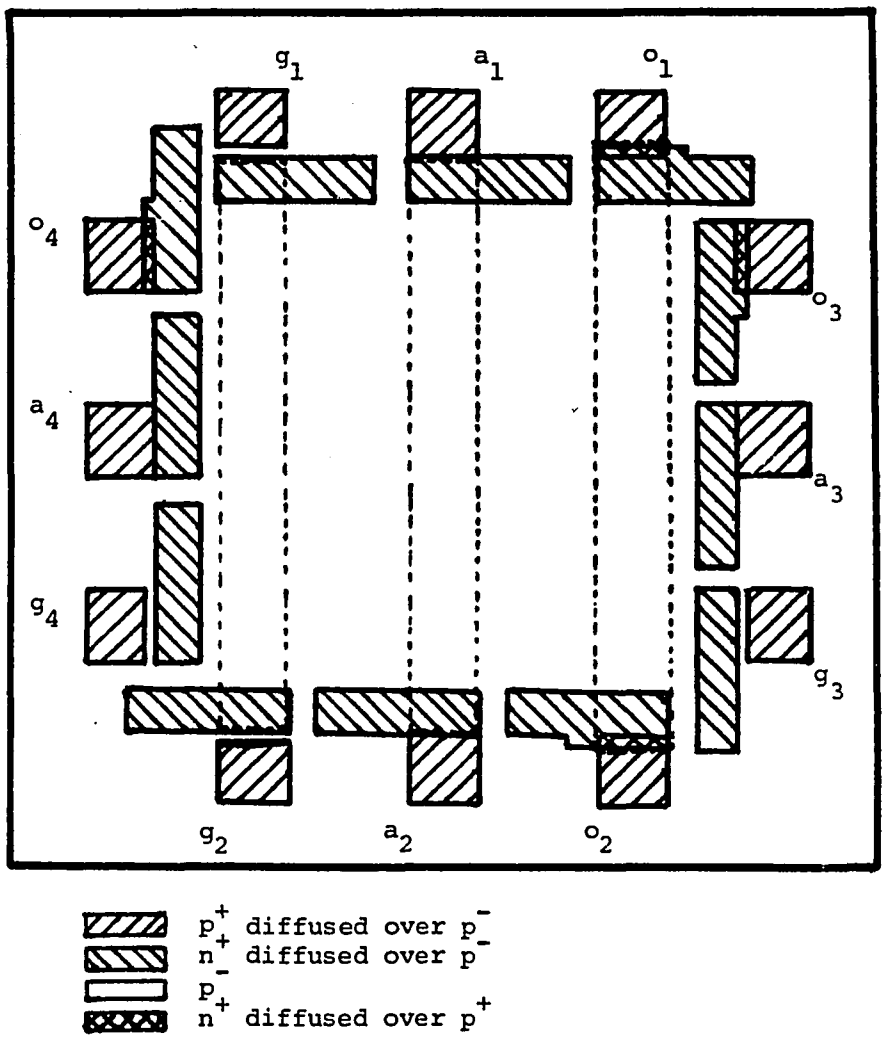

Fig. 4.1. General layout--optical interconnection. -- p^+ and n^+ regions are drawn with full lines. Waveguides are drawn with dashed lines. "o," "a," and "g" stand for overlap, abutting, and gap structures respectively. At the mask level the gap width equals the overlap width and equals 0.2 mils.

considered for the LEDs, with patterns based on Row 9 of Fig. 3.1, which was laid out to check the usefulness of its devices for the optical interconnection. Those devices (Fig. 3.1, Row 9) were tested and light emission took place under avalanche breakdown as in the basic structures, e.g., type O devices, Figs. 3.1 and 3.9. No quantitative evaluation was possible because of the small size of the devices, which made the detection of their light output impossible. Figure 4.2 shows one of the patterns to be used in the present study, with overlap structure. The others differ only slightly, as is shown in Figure 4.1, in order to give gap and abutting structures.

Large dimensions were adopted to have more light available. For this first study, it was decided to lay out equal devices facing each other and study each basic structure separately.

In the considered layout, waveguides are 50 mils long and 6 mils wide.

Figure 4.3 shows the cross-section of an overlap device with the tapered end of the waveguide at the designed position, i.e., with the taper over the junction, in order to couple the light.

4.3 Process Design

For this study both impurities, of p^+ and n^+ types, are diffused using basically the same process outlined in

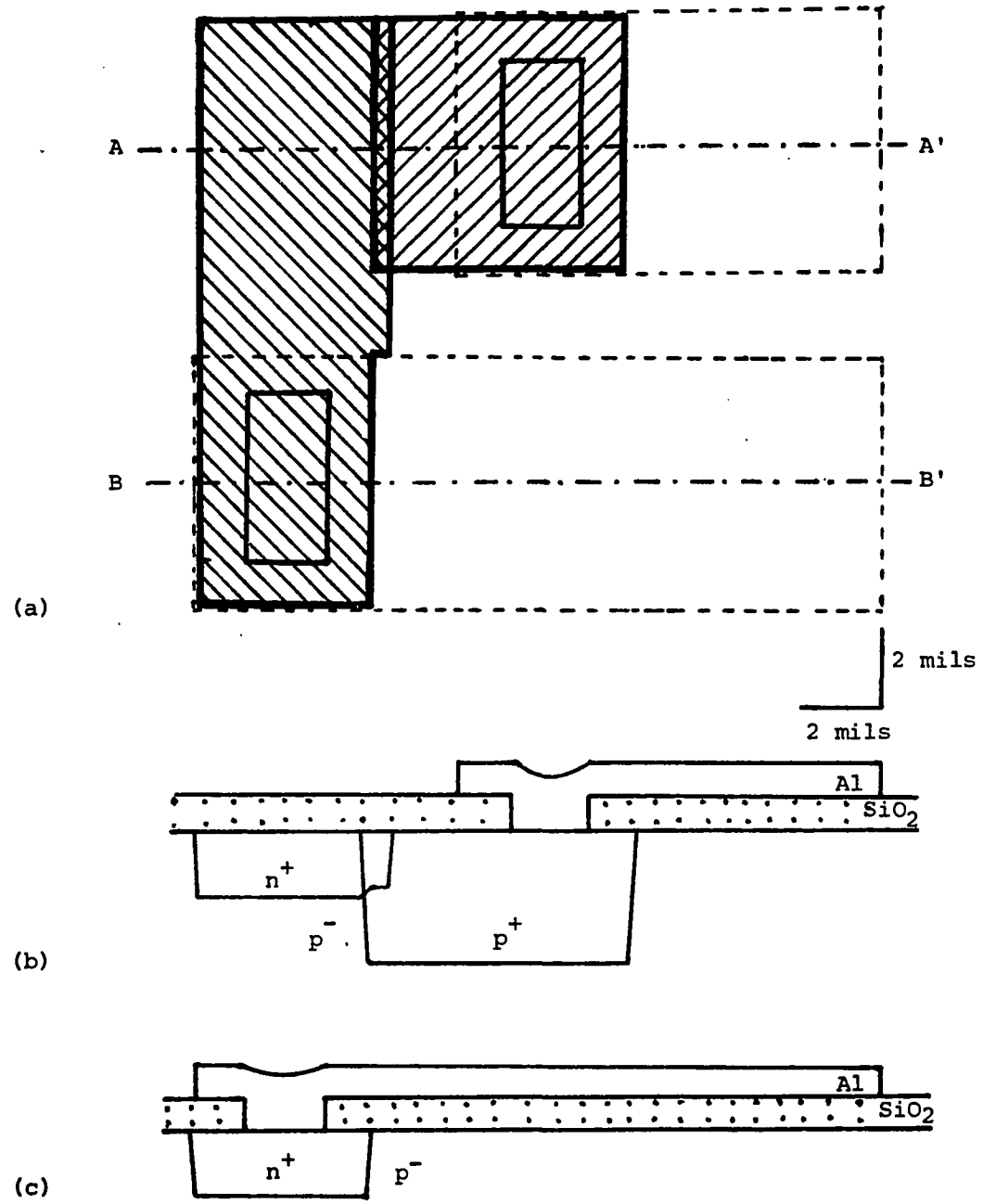

Fig. 4.2. LED for optical interconnections. -- (a) Top view; (b) Cross section A-A'; and (c) Cross section B-B'. Drawn for an overlap structure device.

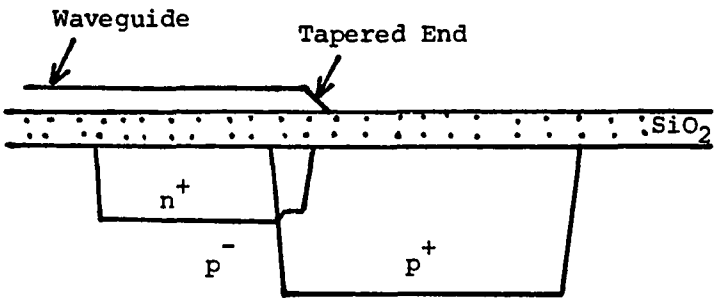

Fig. 4.3. Cross section of an overlap device, with the tapered end of the waveguide at the designed position.

Section 3.4. This process has proven to give light emitting devices with efficiencies comparable with published data. However, as is shown in Section 2.3.1, a low efficiency is expected when these diodes are used as light detectors for an average photon energy of the order of 1.5 eV or less. This was the value assumed in Section 3.5.3.3 for calculating the quantum efficiency of the LEDs, because of the relatively small n^+ diffusion depth, about 1.5 μm. According to Fig. 2.17, the detection efficiency η_D is of the order of 10%.

An estimate of the voltage to be detected by the LED working as a photovoltaic cell is in order. For an emitted power P, and detection and coupling efficiencies η_D and η_C, respectively, the absorbed power at the detector is given by $P/(\eta_D.\eta_C)$. Considering an average photon energy $\hbar\omega$, the number of electron hole pairs (EHP) generated in an active volume Vol of the detector per unit time is:

$$\text{No. of EHP} = \frac{P.\eta_D.\eta_C}{\hbar\omega} \qquad (4.1)$$

Thus, the component of current due to the photogeneration is:

$$q \cdot \frac{P.\eta_D.\eta_C}{\hbar\omega} \equiv q.g_{op}.\text{Vol} \qquad (4.2)$$

where g_{op} is the optical generation rate, and is expressed in EHP/cm^3sec.

Hence, the total current is given by:

$$I = I_o(e^{V/V_T} - 1) - q \cdot \frac{P \cdot \eta_D \cdot \eta_C}{\hbar\omega} \qquad (4.3)$$

where

$$I_o = q.A.(\frac{D_p}{L_p} \cdot p_n + \frac{D_n}{L_n}.n_p) \qquad (4.3)$$

as defined in Section 2.2.2.1, Eq. (2.8), and $V_T = kT/q$. Assuming an emitted power $P = 10^{-7}$ W, a detection efficiency $\eta_D = 0.1$, a coupling efficiency $\eta_C \simeq 1$, which may be achieved using tapers at 45^o to the base, no attenuation in the waveguide, and an average photon energy $\hbar\omega = 1.5$ eV, the voltage generated in open circuit, i.e., for $I = 0$, is:

$$V_{oc} = V_T.\ln(\frac{10^{-8}}{1.5\ I_o} + 1) \qquad (4.5)$$

where I_o is given in amps. This reverse saturation current depends on the assumed lifetimes, concentrations and device structure. If $D_p = 12.5$ cm^2/sec, $D_n = 35$ cm^2/sec, and assuming $\tau_p = \tau_n = 10^{-8}$ sec, it results $L_p = 3.5 \times 10^{-4}$ cm, and $L_n = 5.9 \times 10^{-4}$ cm. Impurity concentrations vary with the distance to the junction. Assuming $N_d = 10^{19}$ cm^{-3} and $N_a = 10^{18}$ cm^{-3}, results in $p_n = 22.5$ cm^{-3} and $n_p = 225$ cm^{-3}. The area A depends on the structure. For a gap structure, assuming a depth of 1.5 μm and a junction length of 6 mils, the area A is of the order of 2.3×10^{-6} cm^2. Thus, substituting in Eq. (4.4), the current I_o is of the order of

5.2×10^{-18} Amp. Thus, using Eq. (4.5), the expected induced voltage is of the order of 0.54 volts. Due to the logarithmic characteristic of Eq. (4.5), an error in the estimation of efficiencies and reverse current of three orders of magnitude would not be significant. Hence, a generated open circuit voltage of the order of 0.3 to 0.5V may be expected.

In order to design the waveguide, many requirements must be satisfied. The index of refraction of a waveguide must be higher than that of the surrounding media, in order to propagate the radiation (Section 2.4.1). If the difference is very large, coupling is easier but more modes are present, limiting the operating bandwidth because of the different velocity of transmission associated with each mode. In Section 2.4.2 it was remarked that the confined modes have part of their electromagnetic energy contained in the two surrounding media. This energy decreases exponentially with distance from the boundary of the waveguide into the other media. A simple conservative rule for reducing the absorption of this electromagnetic energy to acceptable levels requires that the adjacent media do not absorb light in regions of the order of a wavelength deep of the light transmitted from the boundary between the waveguide and the media. In other words, in this region the absorption coefficient must be very small, which is achieved by using

materials with the energy band gap E_g larger than the photon energy of the light to be transmitted.

If the waveguide is deposited over the thermally grown oxide, steps and height changes will scatter the light from the waveguide to the surrounding media. From the cross section of a typical overlap structure, as it is shown in Fig. 4.4, it is visualized that individual steps over the thermally grown oxide may be as high as 700 nm, while the underlying silicon has steps smaller than 150 nm. Thus, for a waveguide a few hundred nanometers thick, which is a typical value deposited over the oxide, most of the light in the waveguide would be scattered to the two surrounding media. The waveguide cannot be deposited over bare silicon because silicon has a higher index of refraction than the usual waveguide materials, ZnS and Si_3N_4, making the waveguiding impossible; the basic condition between indices of refraction is not satisfied (Eq. 2.25). A solution was found. It consisted of stripping the thermally grown oxide, thus eliminating the large steps, and then depositing a layer of CVD SiO_2 of the necessary thickness. This new layer cannot be thermally grown oxide, not only because of the changes in the resulting process parameters, but mainly because of the already diffused phosphorus reflow, which might give a whole n-type layer along the wafer. (The present process uses diffusion furnaces.) Hence, the

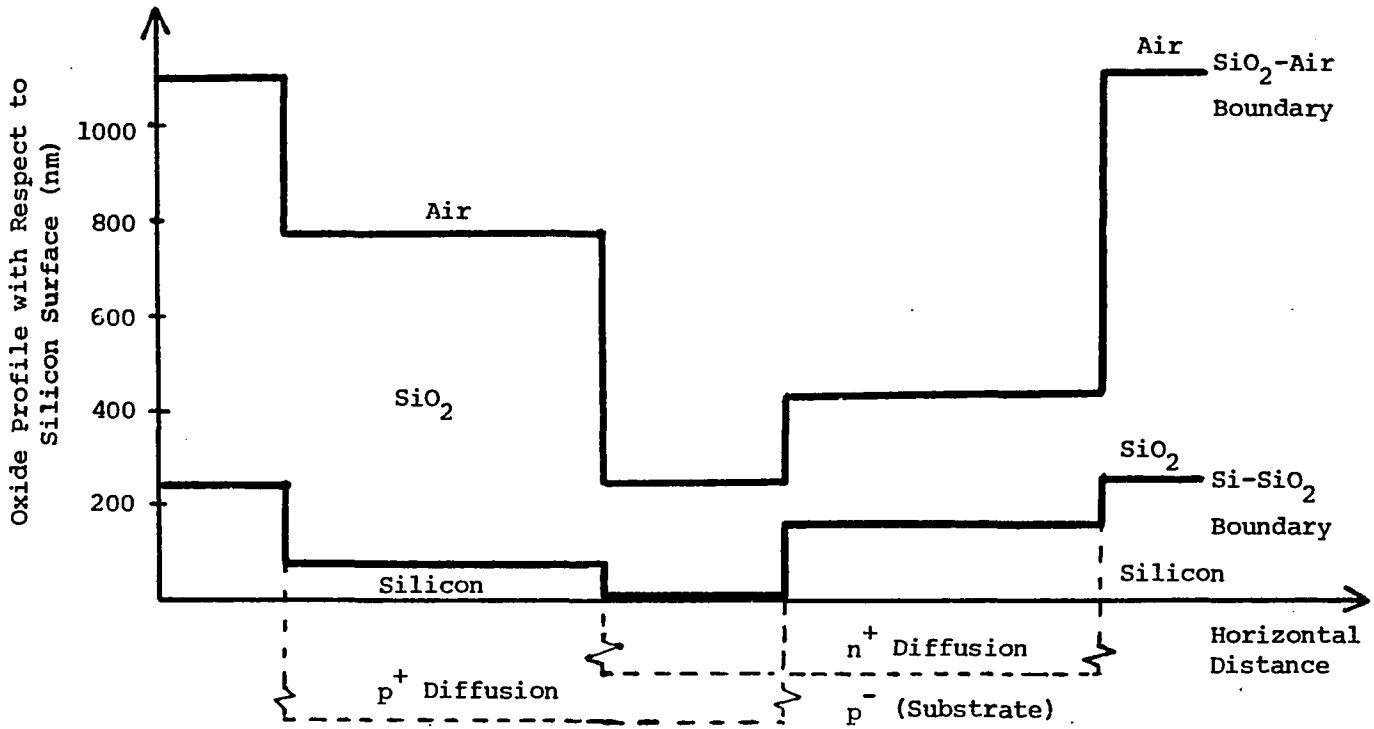

Fig. 4.4. Approximate oxide thicknesses for an overlap structure. -- After a diffusion process in which a p^+-n^+ junction is formed, steps are present on the oxide surface and underlying silicon surface. Thus, a waveguide few hundred nanometers thick might scatter all the light to the other media if the waveguide had to follow those large step changes. In order to simplify the diagram, lateral diffusions were not considered. The drawing is based on data and calculations, and not drawn to scale horizontally.

waveguide must be deposited over the CVD oxide, having at most the step changes of the underlying silicon.

Several process flows were followed, as shown in the process flow chart, Fig. 4.5, not only to find out relations between different impurity concentrations and system efficiencies, but also to check for the need of stripping the thermally grown oxide and depositing a CVD oxide layer as well.

Two basic waveguide materials are ZnS and Si_3N_4 (Section 2.4.4). The first one was selected not only because of its higher index of refraction, making the coupling and the guiding more efficient, but also because of the lack of resources for depositing a layer of Si_3N_4. In order to avoid the possibility of contamination the aluminum metallization was done before the ZnS deposition. A layer of ZnS of nominal thickness 478 nm was deposited at the UA Optical Sciences Center. The substrate characteristics of these wafers is the following.

Wafers 5 and 6:	CVD SiO_2 + P_2O_5 over bare silicon
Wafer 11:	CVD SiO_2 over thermally grown oxide
Wafer 18:	Originally thermally grown oxide, i.e, neither strip of SiO_2 nor CVD growth nor additional thermally grown oxide was done

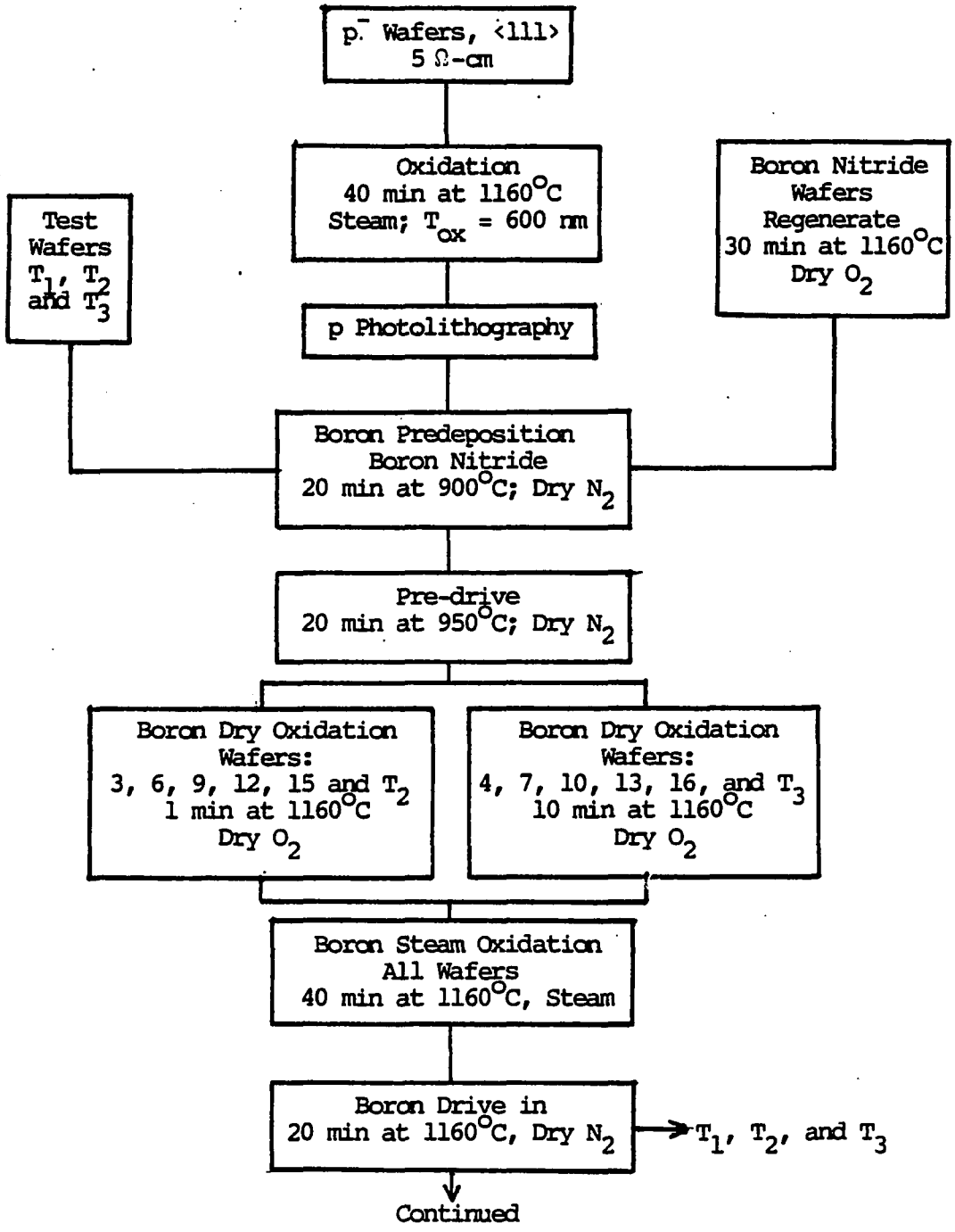

Fig. 4.5. Process flowchart--optical interconnection.

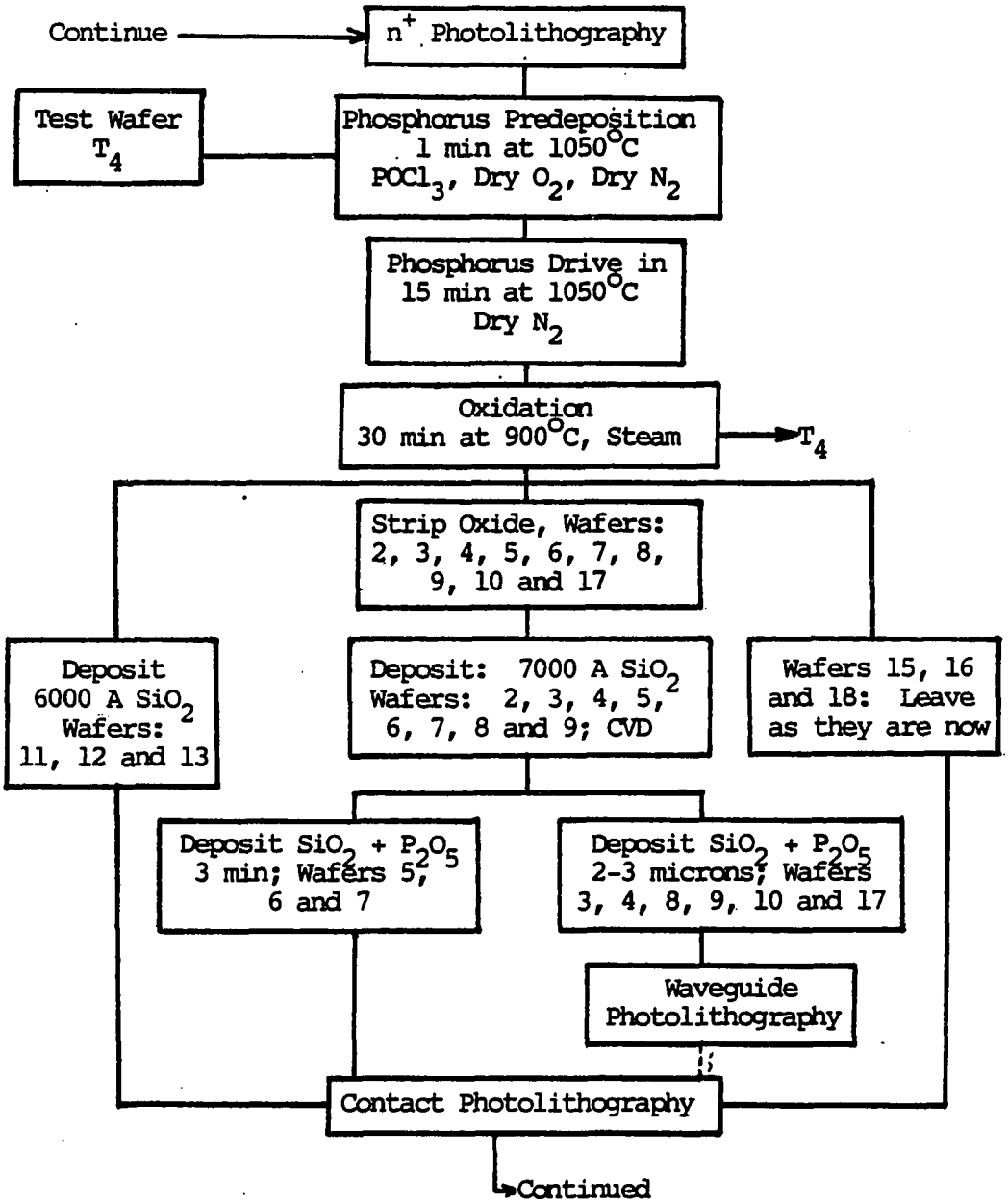

Figure 4.5.--Continued

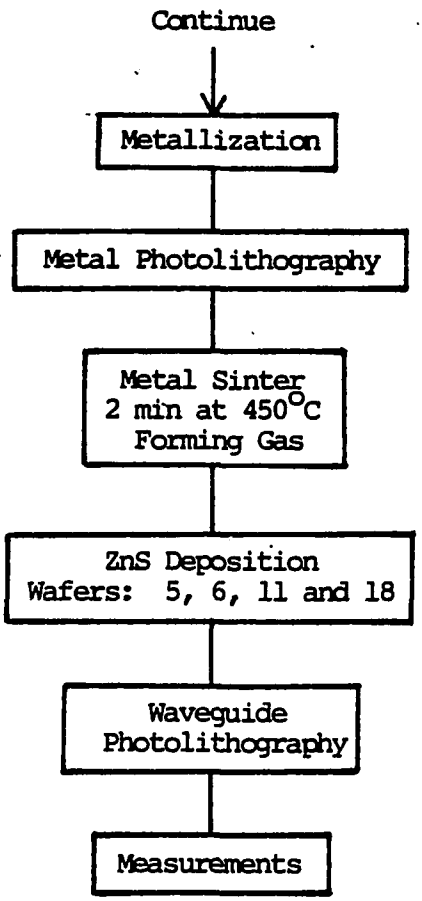

Figure 4.5.--Continued

No other depositions could be done, so the other wafers were not used and their processes interrupted.

The coupling is done by means of having the ends of the waveguides tapered. Ideally a taper with 45^{o} to the base allows a high coupling efficiency. However, in order to have the taper properly aligned over the junction, photolithographic and alignment tolerances smaller than a micron are required. On the other hand, if it is chosen to fabricate the ends of the waveguide with small angles to the base, the tapered ends will extend over a larger distance, relaxing the alignment requirements. The disadvantage of this is that the coupling efficiency will be much lower, mostly at the light source end, as shown in Section 2.4.3. For this project, Kasper aligners were used; thus, a very small yield of working interconnections was expected because of processing limitations. One characteristic helps: in principle it is necessary to have only the tapered end at the light emitting device aligned correctly because the photodetector will also work if light is absorbed a diffusion length from the junction. As source and detector are identical, coupling may occur in one direction, but not in the other.

4.4 Experimental Results

This section describes the etching of the ZnS layer, until obtaining a tapered end waveguide. An additional comment is made regarding the interconnection tests.

Different acids (Section 2.4.4), dilutions and temperatures were tested until a good ZnS etch was obtained. Mixtures of acid and water were tested which ranged from 3 drops of acid, HCl or HNO_3, in 20 ml of DI water, up to 1:20 acid:water.

On those wafers with CVD SiO_2 and thermally grown oxide numbered 11 and 18, respectively, the ZnS broke up into pieces and lifted with any mixture. At higher temperatures (60^oC) the ZnS broke up faster.

Better results were obtained on those wafers with CVD SiO_2 + P_2O_5 (wafers 5 and 6). At room temperature no etching took place even when the wafers were left in the etchant for hours. At higher temperatures (80^oC) all of the ZnS lifted from the wafer in any mixture. Good etching was obtained when a mixture of 3 drops HCl in 20 ml DI water at 60^oC was used. It took 30 minutes to etch most of the ZnS. However, when attempting to taper the ends by undercutting by means of overetching, the ZnS broke into pieces, and what undercutting existed was irregular. In addition, these solutions attack the aluminum, mainly at the border of the contact window, breaking the electrical contact to the pads.

The EKC Nophenol 922 HB photoresist remover attacks the ZnS at 100°C but strips satisfactorily at 60°C for 3 minutes.

Even with all those problems when the wafers were inspected using a Nomarski contrast interferometer, tapered end waveguides with an angle to the base on the order of 45° were found on some dice. No appreciable tapers were noticed at the lateral edges; it might be the photoresist could lift easier from the waveguide ends, where it was narrower, allowing some undercut.

The light emission and detection properties of the LEDs were checked, and some electrical measurements concerning the optical interconnection were made. However, no reliable evidence of an optical interconnection could be obtained. Not enough dice were available for the tests, and due to the lack of resources at the time, no other wafers could be processed.

CHAPTER 5

CONCLUSIONS AND RECOMMENDATIONS

5.1 Summary

In the preceding chapters a study of a silicon light emitting device was presented. In addition, an optical interconnection scheme was proposed. Devices using this scheme were fabricated and some exploratory results were presented. The following is a summary of the results.

Light emission takes place in the depletion region of a diode under avalanche breakdown. When the voltage is increased and breakdown is reached, the first light appears in the corners of the diffused patterns, where the electric field is maximum. The intensity of the emitted light is proportional to the current density through the device, as shown in Fig. 3.15, in agreement with the literature, Section 2.2.3, and higher, double, in devices which have an intrinsic region p^- between the p^+ and n^+ regions, known in this study as gap structures. At 100 mA, or 0.7 W of power input, the power output measured at wavelengths between 4000 Å and 11000 Å, i.e., at photon energies between 3.1 eV and 1.1 eV, for gap structures, is of the order of 0.4 μW, which implies an efficiency of about 6×10^{-7}, and a quantum

efficiency of about 3 x 10^{-6} photons/electron. The spectral distribution of the emitted light in terms of quantum efficiency per unit photon energy interval, as shown in Fig. 3.27, is of the wide band nature, extending from less than 2 eV to more than 3 eV, the measured energy interval, and decreasing monotonically more than two orders of magnitude for increasing photon energies in that interval, in agreement with the literature, as shown in Figs. 2.9 and 2.13a. The spectral distribution in terms of power emitted per unit photon energy interval, as shown in Fig. 3.28, has the same shape in the studied photon energy range, 2 eV to 3 eV. The presence of a higher power output from the p-i-n structures than from the p-n structures suggests that light is also generated in the low concentration region, the p^-. This suggests that the impurity concentration is not an important factor in light generation; this result is contrary to the model proposed by Figielsky and Torun (Haecker, 1974) and by Tam et al. (1984), although it agrees with the model proposed by Kosyachenko et al. (1984), as described in Section 2.2.3. Thus, it is likely that light emission occurs by indirect intraband transitions of high energy carriers accompanied by the transfer of momentum to acoustic phonons.

A pattern was selected for the optical interconnection, as shown in Fig. 4.2, based on the necessary compatibility between aluminum and waveguide.

A process was found for etching ZnS, the waveguide material, based on diluted HCl at an elevated temperature of $60^{o}C$.

To date, no conclusions can be drawn as to whether optical interconnections have been achieved.

5.2 Recommendations for Future Study

Different areas need consideration in order to obtain an efficient and reliable optical interconnection.

Different diffusions should be tested to find better emission and detection efficiencies and to definitely accept or reject the proposed dominance of the impurity concentrations in the light emission process. No major change is expected in the emission spectra because of the lack of a structure.

Better aligners and photolithographic techniques must be used in order to have most of the dice operative. Registration tolerances cannot be larger than a micron.

Zinc sulfide is a brittle material, difficult to process chemically. Other materials such as Si_3N_4 or Ta_2O_5 must be tested. In particular, it is possible to etch and form a tapered end on silicon nitride deposited over SiO_2 using HF/glycerol mixtures (Deckert, 1980).

An interesting solution, called "skeleton," allows a better coupling. This proposed model is shown in Fig. 5.1. A layer of CVD SiO_2 may be etched chemically (Parisi, Haszko and Rozgonyi, 1977) or with plasma etching techniques in order to obtain a tapered end with a changing slope close to 90^{o} at the base and reduced to zero smoothly following a parabola-type pattern. High index material can be deposited over it and etched, resulting in a much better coupling. As it is shown in Fig. 5.1, light that enters through the SiO_2 can also be coupled. However, the pattern must have a curvature; if it is flat, the light will be reflected without forming a guided model, as was discussed in Section 2.4.1 and Fig. 2.20b.

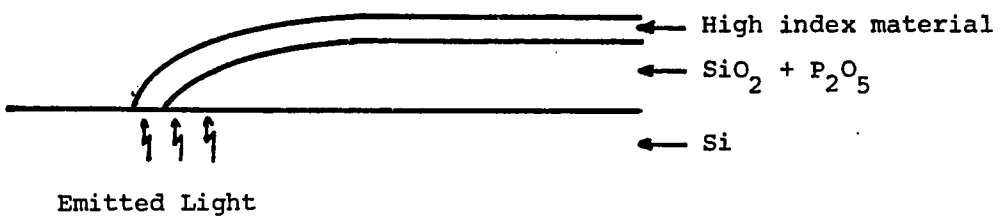

Fig. 5.1. "Skeleton" solution. -- This pattern allows a better coupling than the tapered end waveguide. Note that the thinner, high index material, not necessarily face the junction; other positions would also work.

LIST OF REFERENCES

Baraff, G. A. "Maximum Anisotropy Approximation for Calculating Electron Distributions; Application to High Field Transport in Semiconductors," Phys. Rev., Vol. 133, A 26, 1964.

Chynoweth, A. G., and K. G. McKay. "Photon Emission from Avalanche Breakdown in Silicon," Phys. Rev., Vol. 102, 1956.

Das, N. C., W. S. Khokle, and S. D. Mohanty. "Visible Light Emission from Silicon MOSFETs," Solid State Electronics, Vol. 28, No. 10, 1985.

Deckert, C. A. "Pattern Etching of CVD Si_3N_4/SiO_2 Composites in HF/Glycerol Mixtures," J. Electrochem. Soc., Vol. 127, No. 11, 1980.

Ehret, W. F. Smith's College Chemistry, 6th ed., D. Appleton Century Company, Inc., New York, 1947.

Fan, H. Y., W. Spitzer, and R. J. Collins. "Infrared Absorption in n-Type Germanium," Phys. Rev., Vol. 101, 1956.

Fink, D. G., and D. Christiansen. Electronics Engineer's Handbook, 2nd ed., McGraw-Hill Book Company, 1982.

Fordemwalt, J. N., editor. Laboratory Manual for Integrated Circuit Technology, University of Arizona Publications, 1985.

Goodman, J. W., F. J. Leonberger, S. Y. Kung, and R. A. Athale. "Optical Interconnections for VLSI Systems," Proceedings of the IEEE, Vol. 72, No. 7, 1984.

Grove, A. S. Physics and Technology of Semiconductor Devices, John Wiley & Sons, 1967.

Guts, V. V., L. A. Kosyachenko, and I. V. Solonchuk. Title not available. Ukr. Fiz. Zh., Vol. 28, pp. 1528, 1983.

Haecker, W. "Infrared Radiation from Breakdown Plasmas in Si, GaSb, and Ge: Evidence for Direct Free Hole Radiation," Phys. Stat. Sol. (a), Vol. 25, 1974.

Hamilton, D. J., and W. G. Howard. Basic Integrated Circuits Engineering, McGraw-Hill, 1975.

Hunsperger, R. G. Integrated Optics: Theory and Technology, 2nd ed., Springer-Verlag, 1984.

Kittel, C. Introduction to Solid State Physics, 5th ed., John Wiley & Sons, 1976.

Kosyachenko, L. A., E. F. Kukhto, and V. M. Sklyarchuk, Title not available, Tekh. Sredstv Svyazi Ser. Obshchetekh., No. 5, pg. 54, 1982.

Kosyachenko, L. A., E. F. Kukhto, and V. M. Sklyarchuk. "Mechanism of Electroluminiscence Emitted by a Silicon P-N Junction under a Reverse Bias," Sov. Phys. Semicond., Vol. 18, No. 3, 1984.

Kramers, H. A. "On the Theory of X-ray Absorption and of the Continuous X-ray Spectrum," Phil. Mag., Vol. 46, 1923.

Kressel, H. Semiconductor Devices for Optical Communication, Springer-Verlag, 1980.

Maissel, L., and R. Glang. Handbook of Thin Film Technology, McGraw-Hill, 1970.

Martin, D. H. Spectroscopic Techniques for Far Infrared, Submillimetre and Millimetre Waves, John Wiley & Sons, 1967.

Newman, R. "Visible Light from a Silicon P-N Junction," Phys. Rev., Vol. 100, 1955.

Ogura, S., P. J. Tsang, W. W. Walker, D. L. Critchlow, and J. F. Shepard. "Design and Characteristics of the Lightly Doped Drain-Source (LDD) Insulated Gat Field-Effect Transistor," IEEE Trans. Electron Devices, Vol. ED-27, 1980.

Parisi, G. I., S. E. Haszko, and G. A. Rozgonyi. "Tapered Windows in SiO_2: The Effect of NH_4F:HF Dilution and Etching Temperature," J. Electochem. Soc., Vol. 124, No. 6, 1977.

RCA. Electron Tube Handbook, Radio Corporation of America, Electron Tube Division, 1972.

Shockley, W. "Problems Related to P-N Junctions in Silicon," Solid-State Electron., Vol. 2, 1961.

Streetman, B. G. Solid State Electronic Devices, 2nd ed., Prentice-Hall, Inc., 1980.

Sze, S. M. Physics of Semiconductor Devices, 2nd ed., John Wiley & Sons, 1981.

Tam, S., F. C. Hsu, P. K. Ko, C. Hu, and R. S. Muller. "Spatially Resolved Observation of Visible-Light Emission from Si MOSFETS," IEEE Electron Device Letters, Vol. EDL-4, No. 10, 1983.

Tam, S., and C. Hu. "Hot-Electron-Induced Photon and Photocarrier Generation in Silicon MOSFETs," IEEE Transactions on Electron Devices, Vol. ED 31, No. 9, 1984.

Tien, P. K., and R. J. Martin. "Experiments on Light Waves in a Thin Tapered Film and a New Light-wave Coupler," Appl. Phys. Let., Vol. 18, No. 9, 1971.